Observed Effects of Gravitational Microlensing of Stars by a Spatial−Temporal Tunnel

M. B. Bogdanov[1] and A. M. Cherepashchuk[2]

[1]*Chernyshevsky University, Saratov, Russia*
[2]*Sternberg Astronomical Institute, Universitetskiǐ pr. 13, Moscow, 119899 Russia*
Received March 13, 2002; in final form, May 23, 2002

Abstract—We consider microlensing of stars by a spacetime tunnel (wormhole), which is manifest as a gravitational lens with negative mass and a circular caustic in the source plane. If a source with a small angular size does not cross the circular caustic, it is impossible to discriminate between gravitational lenses with positive and negative mass. Even for comparatively large stellar angular diameters, differences from a Schwarzschild lensing curve are on the order of the observational errors. When the angular size of a star is comparable to the radius of the Einstein cone, for a sufficiently large impact parameter, the shape of the observed light curves can be similar to that due to microlensing of a compact object surrounded by an extended gaseous envelope. Such an object can be easily distinguished from a negative-mass gravitational lens via analysis of chromatic and polarization effects of the lensing. © *2002 MAIK "Nauka/Interperiodica"*.

1. INTRODUCTION

The discovery of gravitational microlensing of stars by massive, compact objects belonging to the Galactic halo [1], predicted in [2, 3], attracted the attention of numerous observers. Currently, several hundred events involving microlensing of stars in the Magellanic Clouds and Galactic bulge have been detected by the international groups MACHO, OGLE, PLANET and others. These data are of considerable interest for a variety of astrophysical problems [4]. However, the nature of the objects that act as the gravitational lenses remains unknown. Essentially the only parameter of the lens that can be derived from the observations is its mass. According to statistical observational data acquired by the MACHO group [5], the masses of lenses in the Galactic halo are $0.15-0.90M_\odot$. More accurate mass estimates are possible for microlensing events for which the effect of the annual parallax is observed. This effect is more distinctly visible for massive lenses. For example, the mass of the lens associated with the EROS BLG-2000-5 event was estimated to be $M = 0.612 \pm 0.057M_\odot$ [6]. For five of six such events observed by the MACHO group in the Galactic bulge, the lens masses exceeded one solar mass; for two of these events—MACHO-96-BLG-5 $\left(M = 6 + \dfrac{+10}{-3}M_\odot \right)$ and MACHO-98-BLG-6 $\left(M = 6 + \dfrac{+7}{-3}M_\odot \right)$—it apparently exceeded the limiting mass for a neutron star [7]. The upper limits for the luminosities of each of these two lenses do not exceed that of the Sun, so that they are black-hole candidates.

The uncertainties of the parameters of the gravitational lenses admits the possibility that the lenses correspond to objects with very different masses. It has been proposed that a substantial fraction, or even all, of the lenses are dwarf stars in our Galaxy [8−12]. Along with the black-hole hypothesis, it was also suggested that they are compact clusters of weakly interacted massive particles (WIMPs) [13−16]. More exotic forms of matter have also been proposed, such as so-called spacetime tunnels (wormholes) [17, 18], which are predicted by the general theory of relativity. The type of lens can be identified from microlensing observations, based on subtle photometric, chromatic, and polarization effects due to both the lens and the lensed source. Here, we consider such effects for gravitational microlensing by a spacetime tunnel.

2. SPATIAL−TEMPORAL TUNNELS AS GRAVITATIONAL MICROLENSES

As was shown in [19−21], the equations of general relativity allow solutions in the form of two regions in spacetime connected by a so-called spacetime tunnel. Such a tunnel can exist only if it is filled with a certain type of exotic matter with a negative energy density and, therefore, a negative mass. It was first suggested in [22] that such an object could be manifest as a gravitational lens capable of forming multiple images of a distant source of radiation. Under certain

conditions, the angular distance between the images can become smaller than the resolving power of telescopes, and the observer will detect only the combined flux from all the images of the source. In this way, the spacetime tunnel will be manifest as a gravitational microlens with negative mass.

Such a microlens modeled as a negative point mass was considered in [17, 18] using the commonly applied approximations of geometric optics and small deviation angles. Like an ordinary gravitational lens, it is basically specified by the angular radius of the Einstein cone p_0, which can be expressed as

$$p_0^2 = \frac{4G|M|}{c^2} \frac{D_{sl}}{(D_{sl} + D_{ol})D_{ol}}, \tag{1}$$

where G is the gravitational constant, M is the mass of the lens, c is the velocity of light, D_{sl} is the distance from the source to the lens, and D_{ol} is the distance from the lens to the observer. The lens equation indicates that its properties differ dramatically from those of an ordinary positive-mass Schwarzschild lens [23, 24] due to the presence of a circular caustic with angular radius $2p_0$ in the source plane. When a point source is located an angular distance $p < 2p_0$ from the lens, it is no longer observed, and the detected flux decreases to zero. When $p > 2p_0$, two images of the source arise, located on one side of the lens between the directions towards the lens and the source. One of the images is always inside the Einstein cone, while the second is outside it. As the source approaches the caustic from the outer side, the images merge and disappear when $p = 2p_0$. The amplification factor for the flux from a source with an infinitely small angular size in the region $p > 2p_0$ is

$$A(u) = \frac{u^2 - 2}{u\sqrt{u^2 - 4}}, \tag{2}$$

where $u = p/p_0$; at a caustic crossing, u formally tends to infinity. Relation (2) differs from the corresponding formula for a Schwarzschild lens [23, 24] only in the signs of the numerical terms in the numerator and denominator.

In the case of lensing of a source with a finite angular size, the flux will increase as it approaches the caustic then sharply decrease and completely disappear. In the course of the egress of the source from the inner region of the circular caustic, the pattern will change to the opposite. For a source with a circularly symmetrical brightness distribution, the light curve, generally called the lensing curve, will always be symmetrical relative to the time of its closest approach to the lens. If the source does not cross the caustic during its relative motion, the lensing curve displays one maximum and its shape is close to those of observed stellar microlensing curves.

3. MICROLENSING CURVES FOR A POINT SOURCE

Taking into account the small angular sizes of the Einstein cones of stellar-mass lenses, the case when the lensed star does not cross the circular caustic is more probable. The question arises: how large is the difference between the lensing curves of an ordinary Schwarzschild lens and a point-like negative-mass lens in this case? Note that this important observational problem was not considered in [17, 18]. In searches for microlensing events, the observed light curves are generally modeled using a point-source curve. It is, therefore, of interest to consider first and foremost this type of source.

Let a source whose angular size is negligibly small compared to p_0 be located an angular distance of $p > 2p_0$ from the center of a point-like, negative-mass lens. We denote $u_s = p_s/p_0$ to be the argument of the factor for the amplification of a point source by a Schwarzschild lens. Equating the amplification factors for these lenses, we obtain

$$\frac{u_s^2 + 2}{u_s\sqrt{u_s^2 + 4}} = \frac{u^2 - 2}{u\sqrt{u^2 - 4}}. \tag{3}$$

After simple manipulation of (3), we obtain a biquadratic equation for u_s:

$$u_s^4 + 4u_s^2 - (u^4 - 4u^2) = 0. \tag{4}$$

When $u > 2$, Eq. (4) has the single real, non-negative root

$$u_s = \sqrt{u^2 - 4}. \tag{5}$$

Thus, with u_s specified by (5), the amplification factors of the lenses coincide.

In the case of linear and uniform motion of the source relative to the lens, the angular distance p varies with time t, and the argument of the amplification factor can be written

$$u = p_0^{-1}\sqrt{p_m^2 + V^2(t - t_0)^2}, \tag{6}$$

where p_m is the minimum angular distance from the lens reached at the time t_0 (the impact parameter) and V is the angular velocity. A relation similar to (6) can also be written for the Schwarzschild lens, labelling the corresponding variable with the subscript s. Taking into account (5), we conclude that, for the same angular velocity $V = V_s$, the curve of a point source lensing by a negative-mass lens does not differ from that for a Schwarzschild lens with the same p_0, provided the impact parameter is $p_{m,s} = \sqrt{p_m^2 - 4p_0^2}$.

Thus, if a point source moves outside the circular caustic, photometric observations cannot distinguish lensing curves due to a spacetime tunnel and a positive-mass gravitational lens. However, it is apparent that the amplification factors of the lenses can be equal only for one value of the impact parameter, so that the lensing curves for extended sources will differ.

$I(t)$
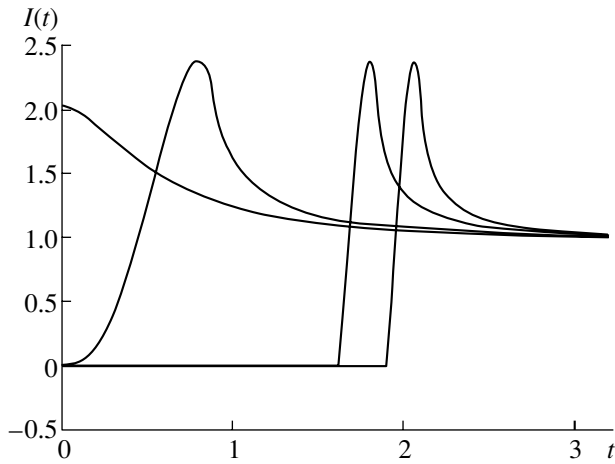
Fig. 1. V light curves for the microlensing of a star with $R = 0.1$ by a spacetime tunnel; time is measured in units of the Einstein cone radius crossing time. The positive branches of the curves for the impact parameters $p_m = 2.1, 1.9, 1.0,$ and 0 are indicated.

4. LENSING CURVES FOR A SOURCE WITH FINITE ANGULAR SIZE

Lensing curves and images of extended sources formed by a negative-mass lens were calculated in [18] using the method of ray tracing and the solution of the lens equation on a 5000×5000 count grid. If we consider only photometric effects, the problem is simplified by the fact that the amplification factor for the flux from a source area element will be specified by (2). The problem is thus similar to the calculation of lensing curves for the case when a source is lensed by a linear caustic [25]. In this case, photometric effects depend only on the one-dimensional projection of the source brightness distribution onto the axis perpendicular to the caustic. We denote this projection, usually called the strip brightness distribution, $B(\xi)$, where ξ is the angular distance from some fixed point of the source, such as the center of a symmetrical source, measured perpendicular to the caustic. The lensing curve $I(x)$ is calculated as a function of the angular distance x between the center of the source and the caustic by integrating the strip brightness distribution taking into account the amplification factor. The central problem here is the singularity of the amplification factor at the caustic. For the $B(\xi)$ profiles of real astronomical objects, a sufficient condition for the convergence of the numerical procedure for the estimation of the integral $I(x)$ is to select the so-called canonical partitioning of the integration interval (uniform grids of the variables ξ_i and x_i, related by the expression $\xi_i = (x_i + x_{i+1})/2$) [26, 27]. Another possibility is that an integer number of counts ξ_i lie within a grid step x_i.

In our case, the lens possesses a circular caustic, and the lensing curve $I(p)$ as a function of the angular distance from the lens p will depend on the one-dimensional brightness distribution $B_p(r)$, which is the source brightness integrated over an infinitely narrow circular strip with radius r concentric to the caustic. Within this strip, the lens amplification factor (2) remains constant. If the angular size of the source is much smaller than p_0, the curvature of the caustic can be neglected, and the distribution $B_p(r)$ coincides with the strip brightness distribution. As in the previous case, the influence of the singularity of the integral in the flux calculation can be removed by corresponding selection of the grids for the variables p_i and r_i.

Further, we will assume the lensed source to be a star and the brightness distribution over the stellar disk to display circular symmetry. In this case, the detected flux will depend only on the angular distance between the center of the stellar disk and the lens. For most stars, the limb darkening is described by the linear law

$$b_\lambda(\mu) = b_\lambda(1)(1 - u_\lambda + u_\lambda \mu), \qquad (7)$$

where μ is the cosine of the angle between the line of sight and the normal to the stellar surface and u_λ is the limb-darkening coefficient, which depends on the wavelength λ. The value μ corresponding to the angular distance from the center of the star ρ is related to it by the expression $\mu = \sqrt{R^2 - \rho^2}/\rho$, where R is the angular radius of the star. Further, we will assume that the brightness at the center of the star can be written $b_\lambda(1) = 1/\pi R^2(1 - u_\lambda/3)$, which normalizes its flux to unity.

Let us introduce a polar coordinate system (r, φ) with its origin coincident with the lens. If the center of the stellar disk is located an angular distance p from the lens, the integrated brightness of the circular strip of the disk specified by the radius r is
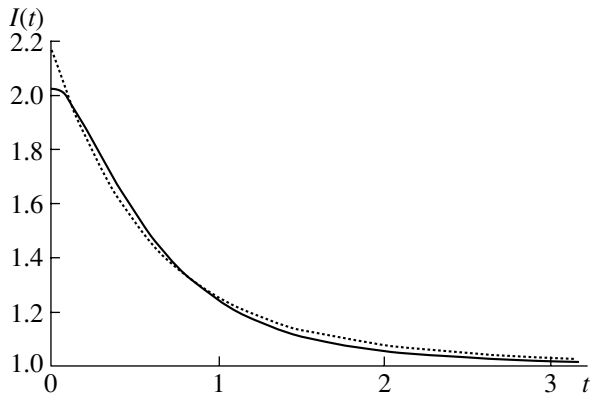
$$B_p(r) = 2 \int_0^{\varphi_m} b_\lambda(\rho) r d\varphi, \qquad (8)$$

where $\rho^2 = r^2 + p^2 - 2rp \cos \varphi$ and an upper limit for the integral can be derived from the condition $R^2 = r^2 + p^2 - 2rp \cos \varphi_m$. Taking into account the caustic amplification factor (2), the detected radiation flux is

$$I(p) = \int_{p-R}^{p+R} A(r/p_0)B_p(r)dr, \qquad (9)$$

where $A(r/p_0) = 0$ for $r < 2p_0$.

We expect from statistical reasoning that the lensed star will probably be a late-type dwarf. Since

Fig. 2. Comparison of the curve for microlensing of a star with $R = 0.1$ by a spacetime tunnel for the impact parameter $p_m = 2.1$ (solid) and the most similar curve for the microlensing of a point source by a Schwarzschild lens (dashed). The units along the horizontal axis are the same as in Fig. 1.
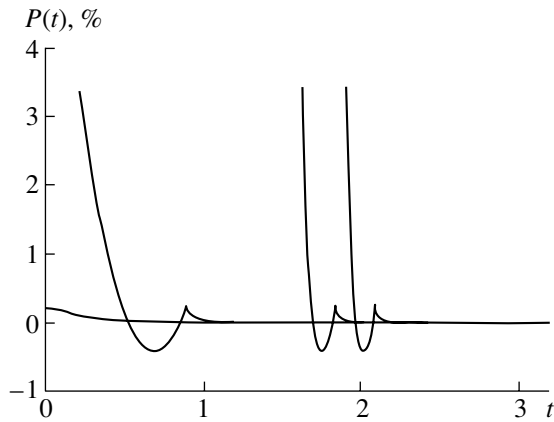

Fig. 3. Variation of the color index $V-I$ for the microlensing of a star by the spacetime tunnel shown in Fig. 1. The units along the horizontal axis are the same as in Fig. 1.

most red stars display intrinsic variability, they are not usually included in searches for microlensing events. Therefore, to estimate the effect of the finite angular size of the source, we chose a K0V star, and assumed that its limb-darkening coefficient is $u_V = 0.702$ in the V band [28]. The lensing curves were calculated using (7) and (8) and canonical-partition grids with a step sufficiently small that the relative error would not exceed 10^{-4}. Since the flux depends only on the angular distance p, the lensing curve can be calculated for a single value of the impact parameter $p_m = 0$; we can find the counts for other values via interpolation. We used a cubic spline interpolation, which provided the necessary accuracy. We chose the value $R = 0.10$ for the comparison with the calculations [17] (further, we will measure all angles in units of p_0).

The lensing curves were calculated for the impact parameters $p_m = 0$, 1.0, 1.9, and 2.1. Assuming $V = 1$ in (6), we will measure time in units of the time required to cross the angular radius of the Einstein cone. Figure 1 presents these results. Since all the curves are symmetrical about the time of closest approach to the lens, the figure shows only their positive branches. Our calculations are consistent with the results of [17], confirming the validity of the technique used.

We can see from Fig. 1 that, when the star does not cross the circular caustic, the lensing curve displays a single maximum and its shape is similar to that for a Schwarzschild lens. Extending the analysis of the previous section, we can ask how much these curves differ and whether it is possible to compensate for the differences by appropriate selection of the parameters. To estimate the differences between the curves, we took 100 equidistant counts of the curve
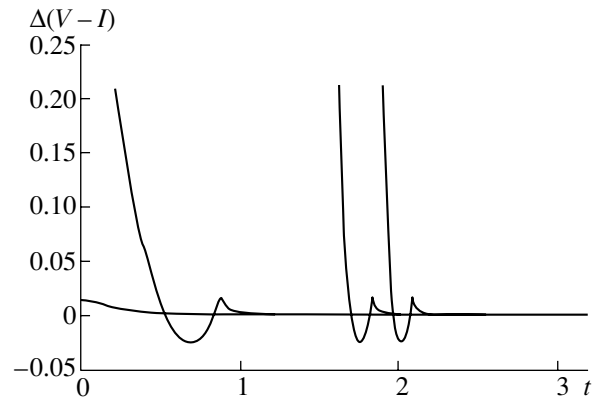
with $p_m = 2.1$ and attempted to fit the light curve for a Schwarzschild lens to them, varying the parameters R, p_m, and V such that the sum of the squares of the deviations reached a minimum. The method used to calculated the curves for the lensing of a star by a Schwarzschild lens is described in [29]. The discrepancy decreased with decreasing R, and the best result corresponded to a point source with $p_m = 0.358$ and $V = 0.734$. Figure 2 presents both lensing curves. The largest discrepancy between them occurs at the maximum brightness. The differences away from the maximum are small and, given the comparatively low accuracy of photometry in crowded stellar fields, it would be rather difficult to discriminate between these two lensing curves.

When a star crosses the circular caustic, characteristic symmetrical lensing curves with a central depression are formed. They differ markedly from observed stellar microlensing curves and could potentially provide unambiguous evidence for the presence of a negative-mass gravitational lens. However, in the recent study [30] of microlensing of stars by a compact object surrounded by an extended gaseous envelope, due to the extinction of the stellar radiation by refraction and Rayleigh scattering in the envelope, the lensing curve can acquire a shape close to that characteristic of a negative-mass lens. One possibility for discriminating between these two types of lens is provided by analyses of chromatic effects associated with the lensing.

5. CHROMATIC EFFECTS OF MICROLENSING

The basic property of gravitational lenses of both positive and negative masses is that their parameters are independent of wavelength. However, the amplification factors are different for radiation from

Fig. 4. The variation of the degree of polarization for curves of microlensing of a star by the spacetime tunnel shown in Fig. 1. The units along the horizontal axis are the same as in Fig. 1.

different regions of the stellar disk. Due to the wavelength dependence of the brightness distribution, this results in chromatic effects during the microlensing. The possibility of observing these effects for ordinary gravitational lenses has been considered, for example, in [31–33]. Such an analysis for a negative-mass lens was carried out in [17] by calculating the U and I lensing curves for a K giant with $T_{\text{eff}} = 4750$ K and $R = 0.10$, assuming that the limb-darkening coefficients were $u_U = 1.050$ and $u_I = 0.503$. The limb-darkening coefficients u_λ were determined by comparing the law (7) and brightness distributions calculated for model stellar atmospheres. In this case, u_λ can be estimated in different ways, based on either conservation of the total flux or the best consistency between (7) and the calculated data [28]. The first method formally yields $u_\lambda > 1$. However, it is physically meaningless to use this value to calculate the brightness distribution (7), as was done in [17], since this yields negative brightnesses at the edge of the stellar disk.

We calculated the variations of $V-I$ for microlensing of a K0V star by a negative-mass object, since exactly these photometric bands are most frequently used in searches for gravitational-microlensing events. The limb-darkening coefficients $u_V = 0.702$ and $u_I = 0.433$ were taken from [28]. As for the calculation of the photometric effects, we adopted $R = 0.10$, $V = 1$, and $p_m = 0$, 1.0, 1.9, 2.1. Figure 3 presents the resulting positive branches of the color-variation curves. As expected, the maximum variation $\Delta(V-I)$, which corresponds to reddening, occurs when the stellar disk is almost entirely inside the circular caustic. However, the radiation flux is very small (Fig. 1) and cannot be detected. We restricted the calculations to the region in which the V flux exceeds 0.001 of its initial value. In the course of the passage of the

stellar disk across the caustic, $\Delta(V-I)$ changes sign twice: after reddening, the star becomes bluer, then redder again. However, in the region where the flux is appreciably different from zero, the chromatic effects are small and can be detected only with rather high photometric accuracy. If the star does not cross the circular caustic, the color varies in the same way as for a Schwarzschild lens [31] and reddening is always observed.

Thus, in the same way as for ordinary gravitational lenses, chromatic effects during the microlensing of a star by a spacetime tunnel are second-order compared to photometric effects. However, their detection could make it easy to discriminate between this exotic object and a compact body with an extended gaseous envelope. In the latter case, the chromatic effects will be very different in both their values and character, due to the strong wavelength dependence of the refraction and, especially, of Rayleigh scattering ($\propto \lambda^{-4}$).

6. POLARIZATION EFFECTS OF MICROLENSING

Analogous to chromatic effects, gravitational microlensing of stars gives rise to variable polarization of the observed radiation, due to the character of the polarization distribution over the stellar disk. The stellar radiation becomes polarized as a result of scattering in the stellar atmosphere. Chandrasekhar [34] and Sobolev [35] demonstrated that the radiation emerging from a plane-parallel Rayleigh atmosphere is partially polarized, with the direction of the electric vector being perpendicular to the plane containing the line of sight and the normal to the stellar surface. In ordinary observations of stars, the detected total radiation from the entire stellar disk is unpolarized due to the disk's symmetry. The origination of partial polarization of the total flux is associated with a violation of the disk symmetry due to rapid rotation of the star, tidal deformation, the presence of hot spots and/or an asymmetrical envelope, or a combination of these factors. It is apparent that the action of a gravitational lens also violates the disk symmetry. The type and degree of polarization observed during microlensing of a star by a positive-mass lens were considered in [36, 37].

To analyze the linear polarization that originates during the propagation of radiation in the atmosphere of a star, it is convenient to introduce the intensities b_l in the direction normal to the stellar surface in the plane of the line of sight and b_r in the direction perpendicular to this. For simplicity, we will assume that the lensed star has a plane-parallel Rayleigh atmosphere. In this case, the exact brightness distributions b_l and b_r over the stellar disk are presented

by Chandrasekhar [34]. For our estimates, it is more convenient to use the approximate formulas derived in [38]:

$$b_r + b_l = \frac{1 + 16.035\mu + 25.503\mu^2}{1 + 12.561\mu + 0.331\mu^2}, \quad (10)$$

$$\frac{b_r - b_l}{1 - \mu} = \frac{0.1171 + 3.3207\mu + 6.1522\mu^2}{1 + 31.4160\mu + 74.0112\mu^2}, \quad (11)$$

where, as in (7), μ is the cosine of the angle between the line of sight and the normal to the stellar surface. Relations (10) and (11) can be used to estimate the intensities of the polarized components, so that the relative error of the degree of polarization $P = (b_r - b_l)/(b_r + b_l)$ compared to the exact solution for any μ does not exceed 0.001.

Let us bring the origin of the polar coordinate system (ρ, θ) to the center of the stellar disk, so that the main axis from which we measure the angle θ will be directed towards the gravitational lens, located an angular distance p from the coordinate origin. Due to the circular symmetry of the initial brightness distributions b_l and b_r, it is apparent that the flux and degree of polarization of the detected radiation will depend only on p. Let $b_L(\rho, \theta)$ and $b_R(\rho, \theta)$ be the intensities at the point of the visible stellar disk with the coordinates (ρ, θ) for observations through polarizers oriented parallel and perpendicular to the direction towards the lens. Then, according to the transformation law for the Stokes parameters (and, accordingly, for the intensities b_l and b_r), we have

$$b_L(\rho, \theta) = b_r(\rho)\sin^2\theta + b_l(\rho)\cos^2\theta, \quad (12)$$

$$b_R(\rho, \theta) = b_l(\rho)\sin^2\theta + b_r(\rho)\cos^2\theta. \quad (13)$$

The coordinate system (ρ, θ) is related to the system (r, φ) introduced in Section 4: $r\sin\varphi = \rho\sin\theta$. Taking this into account and substituting the brightness distributions (12) and (13) into (8) and (9), we can calculate the flux from the star with the polarizer oriented in the parallel ($I_L(p)$) and perpendicular ($I_R(p)$) directions relative to the lens. The degree of polarization $P(p)$ when the center of the star is an angular distance p from the lens will be

$$P(p) = \frac{I_R(p) - I_L(p)}{I_R(p) + I_L(p)}. \quad (14)$$

Figure 4 presents the positive branches of the polarization curves for the microlensing of a star with a Rayleigh atmosphere calculated for the same lensing parameters as in the previous sections. As previously, we will consider only those sections of the curves for which the flux is no lower than 0.001 of the initial value. Since, like the chromatic effects, the polarization effects of microlensing are due to differences in the radiation from the central and limb regions of the stellar disk, it is not surprising that the shape of the polarization curves essentially coincides with that of the color-index variation curves (Fig. 3). During the passage of the caustic across the stellar disk, the degree of polarization changes sign twice. According to (14), this means that the plane of the electric vector is first perpendicular ($P > 0$), then parallel ($P < 0$), and finally perpendicular ($P > 0$) to the direction towards the lens.

When the star does not cross the circular caustic, the degree of polarization is always positive, and the plane of the electric vector is always perpendicular to the direction from the center of the star towards the gravitational lens. Thus, with sufficient observational accuracy, it may be possible to detect the rotation of the plane of polarization as the star moves relative to the lens. At the time when the maximum degree of polarization is attained, which coincides with the maximum brightness of the lensed star, the plane of polarization will be specified by the position angle of the relative motion of the star and lens. The direction of the motion remains unspecified, due to the symmetry. A similar pattern is observed for a Schwarzschild lens [37].

For a star with a pure Rayleigh atmosphere, the degree of polarization is small, and its maximum, reached at the very edge of the stellar disk, is 11.7%. Since the albedo of a singular scattering under the conditions in stellar atmospheres is always smaller than unity, we expect that the polarizations of real stars will be lower, so that the calculated values correspond to upper limits. In addition, the Nagirner effect may also be observed [39], which is manifest by a rotation of the plane of polarization with motion from the edge of the stellar disk. The influence of the true absorption on the polarization of the radiation emerging from the atmosphere of the star assuming a plane-parallel geometry was considered in detail in [40]. In the Wien region of the spectrum, P can appreciably exceed the value for a Rayleigh atmosphere. The degree of polarization for long wavelengths is smaller, but remains appreciable. For late-type dwarfs, which statistically are most likely to be lensed, an additional contribution to the increase of P may be introduced by Rayleigh scattering on molecules. Overall, for real stars, the order of magnitude of the calculated polarizations is expected to remain valid.

Thus, both chromatic and polarization effects during the microlensing of a star by a spacetime tunnel are small. However, the accuracy of current polarimetric observations considerably exceeds photometric accuracy; for sufficiently bright objects, P can be determined with an error not exceeding 0.01%. Unfortunately, this accuracy cannot be provided in monitoring observations during searches for microlensing

events. However, observers have already accumulated considerable experience in triggering large telescopes to observe detected events involving microlensing by gravitational-lens caustics, so that prospects for observing these polarization effects are fairly encouraging.

7. CONCLUSION

The unambiguous identification of such an exotic object as a spacetime tunnel from observations of gravitational microlensing of stars is a rather complicated problem. If a source with a small angular size does not cross the circular caustic, it is impossible to discriminate between gravitational lenses with positive and negative mass. Even for stars with relatively large angular diameters, deviations from the lensing curve for a Schwarzschild lens are of the order of the observational errors.

Distinctive photometric features of microlensing by a negative-mass body are a sharp decrease of the flux considerably below the initial level during the caustic crossing and a symmetric lensing curve. However, unavoidable gaps in the observations may prevent the detection of the second caustic crossing, and the shape of the light curve in the vicinity of the maximum is approximately the same as for microlensing by a caustic of an ordinary binary gravitational lens. When the angular size of the star is comparable to the radius of the Einstein cone for sufficiently large impact parameters, the observed light curves should resemble those for microlensing of a compact object surrounded by an extended gaseous envelope. This case can be easily distinguished from a negative-mass lens through an analysis of the chromatic and polarization effects arising during the lensing.

REFERENCES

1. C. Alcock, C. W. Akerlof, R. A. Allsman, *et al.*, Nature **365**, 621 (1993).
2. A. V. Byalko, Astron. Zh. **46**, 998 (1969) [Sov. Astron. **13**, 784 (1969)].
3. B. Paczynski, Astrophys. J. **304**, 1 (1986).
4. A. F. Zakharov and M. V. Sazhin, Usp. Fiz. Nauk **168**, 1041 (1998) [Phys. Usp. **41**, 945 (1998)].
5. C. Alcock, R. A. Allsman, D. R. Alves, *et al.*, Astrophys. J. **542**, 281 (2000).
6. J. H. An, M. D. Albrow, J.-P. Beaulieu, *et al.*, astro-ph/0110068 (2001).
7. D. P. Bennett, A. C. Becker, J. L. Quinn, *et al.*, astro-ph/0109467 (2001).
8. B. V. Komberg, D. A. Kompaneets, and V. N. Lukash, Astron. Zh. **72**, 457 (1995) [Astron. Rep. **39**, 402 (1995)].
9. E. J. Kerins, Astron. Astrophys. **322**, 709 (1997).
10. M. B. Bogdanov and A. M. Cherepashchuk, Astron. Zh. **75**, 261 (1998) [Astron. Rep. **42**, 229 (1998)].
11. B. S. Gaudi, M. D. Albrow, J. H. An, *et al.*, astro-ph/0104100 (2001).
12. C. Alcock, R. A. Allsman, D. R. Alves, *et al.*, Nature **414**, 617 (2001).
13. A. V. Gurevich, K. P. Zybin, and V. A. Sirota, Usp. Fiz. Nauk **167**, 913 (1997) [Phys. Usp. **40**, 869 (1997)].
14. M. V. Sazhin, A. G. Yagola, and A. V. Yakubov, Phys. Lett. A **219**, 199 (1996).
15. A. F. Zakharov, Astron. Zh. **76**, 379 (1999) [Astron. Rep. **43**, 325 (1999)].
16. M. B. Bogdanov, Astron. Zh. **78**, 1059 (2001) [Astron. Rep. **45**, 929 (2001)].
17. E. Eiroa, G. E. Romero, and D. F. Torres, gr-qc/0104076 (2001).
18. M. Safonova, D. F. Torres, and G. E. Romero, gr-qc/0105070 (2001).
19. M. S. Morris and K. S. Thorne, Am. J. Phys. **56**, 395 (1988).
20. D. Hochberg and M. Visser, Phys. Rev. D **56**, 4745 (1997).
21. D. Hochberg, A. Popov, and S. V. Sushkov, Phys. Rev. Lett. **78**, 2050 (1997).
22. S.-W. Kim and Y. M. Cho, in *Proceedings of the Seventh Marcel Grossman Meeting, Stanford University, 1994* (World Scientific, River Edge, 1996), p. 1147.
23. P. Schneider, J. Ehlers, and E. E. Falco, *Gravitational Lenses* (Springer-Verlag, Berlin, 1992).
24. A. F. Zakharov, *Gravitational Lenses and Microlenses* [in Russian] (Yanus-K, Moscow, 1997).
25. M. B. Bogdanov and A. M. Cherepashchuk, Astron. Zh. **77**, 842 (2000) [Astron. Rep. **44**, 745 (2000)].
26. S. M. Belotserkovskiĭ and I. K. Lifanov, *Numerical Methods in Singular Integral Equations and Their Application to Aerodynamics, the Theory of Elasticity, and Electrodynamics* [in Russian] (Nauka, Moscow, 1985).
27. M. B. Bogdanov, astro-ph/0102031 (2001).
28. A. A. Rubashevskiĭ, Astron. Zh. **67**, 860 (1990) [Sov. Astron. **34**, 433 (1990)].
29. M. B. Bogdanov and A. M. Cherepashchuk, Astron. Zh. **72**, 873 (1995) [Astron. Rep. **39**, 779 (1995)].
30. V. Bozza, P. Jetzer, L. Mancini, and G. Scarpetta, astro-ph/0111079 (2001).
31. M. B. Bogdanov and A. M. Cherepashchuk, Pis'ma Astron. Zh. **21**, 570 (1995) [Astron. Lett. **21**, 505 (1995)].

32. A. Loeb and D. Sasselov, Astrophys. J. Lett. **449**, L33 (1995).

33. C. Han, S.-H. Park, and J. H. Jeong, Mon. Not. R. Astron. Soc. **316**, 97 (2000).

34. S. Chandrasekhar, *Radiative Transfer* (Clarendon, Oxford, 1950; Inostrannaya Literatura, Moscow, 1953).

35. V. V. Sobolev, *Radiative Transfer in the Atmospheres of Stars and Planets* [in Russian] (Gostekhizdat, Moscow, 1956).

36. J. E. L. Simmons, J. P. Willis, and A. M. Newsam, Astron. Astrophys. **293**, L46 (1995).

37. M. B. Bogdanov, A. M. Cherepashchuk, and M. V. Sazhin, Astrophys. Space Sci. **235**, 219 (1996).

38. N. G. Bochkarev and E. A. Karitskaya, Pis'ma Astron. Zh. **9**, 14 (1983) [Sov. Astron. Lett. **9**, 6 (1983)].

39. D. I. Nagirner, Tr. Astron. Obs. Leningr. Gos. Univ. **19**, 79 (1962).

40. N. Bochkarev, E. A. Karitskaya, and N. A. Sakhibullin, Astrophys. Space Sci. **108**, 15 (1985).

Tranlsated by K. Maslennikov

Infrared Photometry of the Unique Object FG Sge in 1985−2001

O. G. Taranova and V. I. Shenavrin

Sternberg Astronomical Institute, Moscow State University, Universitetskiĭ pr. 13, Moscow, 119992 Russia
Received April 20, 2002; in final form, May 23, 2002

Abstract—Our analysis of many years of infrared photometry of the unique object FG Sge indicates that the dust envelope formed around the supergiant in August 1992 is spherically symmetrical and contains compact, dense dust clouds. The emission from the spherically symmetrical dust envelope is consistent with the observed radiation from the star at 3.5−5 μm, and the presence of the dust clouds can explain the radiation observed at 1.25−2.2 μm. The mean integrated flux from the dust envelope in 1992−2001 was $\sim (1.0 \pm 0.2) \times 10^{-8}$ erg s^{-1}cm^{-2}. The variations of its optical depth in 1992−2001 were within 0.5−1.0. The maximum density of the dust envelope was recorded in the second half of 1993 and corresponded to mean optical depths as high as unity. Several times in the interval from 1992 to 2001, the dusty material of the envelope partially dissipated and was then replenished. For example, the optical depth of the dust cloud at $\lambda = 1.25$ μm during the last brigthness minimum in the J band was $\tau_{1.25} \approx 4.3$, which is much higher than the optical depth of the dust envelope of FG Sge. During maxima of the J brightness, the mean spectral energy distribution at 0.36−5 μm can be represented as a combination of radiation from a G0 supergiant that is attenuated by a dust envelope with a mean optical depth of 0.65 ± 0.15 and emission from the spherically symmetrical dust envelope itself, with the temperature of the graphite grains being 750 ± 150 K. At minima of the J brightness, only radiation from the dust envelope is observed at 1.65−5 μm, with the radiation from the supergiant barely detectable at 1.25 μm. As a result, the integrated flux during J minima is almost half that during J maxima. The mean mass of the spherically symmetrical dust envelope of FG Sge in 1992−2001 was $(3 \pm 1) \times 10^{-7} M_\odot$. This envelope's mass varied by nearly a factor of two during 1992−2001, in the range $(2-4) \times 10^{-7} M_\odot$. In Autumn 1992, the mass-loss rate from the supergiant exceeded $2 \times 10^{-7} M_\odot$/yr. The average rate at which matter was injected into the envelope during 1993−2001 was $10^{-8} M_\odot$/yr. The mean rate of dissipation of the dust envelope was about $1 \times 10^{-8} M_\odot$/yr. During 1992−2001, the supergiant lost about $8.7 \times 10^{-7} M_\odot$. The parameters of the dust envelope were relatively constant from 1999 until the middle of 2001. © *2002 MAIK "Nauka/Interperiodica"*.

1. INTRODUCTION

In 1985, the unique object FG Sge (the nucleus of the planetary nebula He 1-5) was included in our program of studies of circumstellar dust envelopes[1]. The object's instability, the presence of pulsations similar to those observed for RV Tauri stars, and its systematic reddening over decades until the autumn of 1992, provided evidence for a dust envelope surrounding FG Sge. Our monitoring of the object in 1985−1989 enabled us to detect for the first time a relatively hot, optically thin dust envelope [2], as was confirmed in [3, 4]. Until the autumn of 1992, the $JHKL$ brightesses of FG Sge demonstrated small-scale pulsations with amplitudes up to $0^m\!.3$ and a quasi-period of 100−120 days. In 1985−1989, the 0.36−2.2 μm spectral energy distribution (SED) corresponded to an F8−G1 supergiant, and the star's photometric parameters were similar to those of RV Tauri stars. At that time, the mean V brightness was $9^m\!.18 \pm 0^m\!.05$, the J brightness was

$7^m\!.10 \pm 0^m\!.03$, the K brightness was $6^m\!.56 \pm 0^m\!.02$, and the L brightness was $6^m\!.31 \pm 0^m\!.02$.

The star's optical to near-IR (JH) brightness began to drop rapidly in August 1992. In the optical, the star faded by $\sim 5^m$ (in V) within several weeks, and the J brightness dropped by approximately $2^m\!.5$. Simultaneously, the brightness at $\lambda > 2.2$ μm began to increase. For example, the L brightness increased by more than $\sim 2^m$ during the second half of September 1992 [4]. The character of the brightness and color changes of FG Sge over a wide spectral range in September 1992 made it possible to unambiguously attribute the observed effects to the formation of a dust envelope around the star. Numerous papers have analyzed observations of FG Sge acquired after September 1992; lists can be found, for example, in the papers of Gonzalez *et al.* [5] and Arkhipova *et al.* [6]. Our own observations of FG Sge in 1993−1997 are analyzed by Tatarnikov *et al.* [7] and Tatarnikov and Yudin [8].

The current paper presents $JHKLM$ photometric

data for FG Sge obtained from 1985 to 2001 and an analysis of IR photometric data obtained mainly after 1997.

2. OBSERVATIONS

Our $JHKLM$ photometry of FG Sge (along with other objects in our observing program) is carried out on the 125 cm telescope of the Sternberg Astronomical Institute's Crimean Station using an InSb photometer. The uncertainties of the photometric measurements of FG Sge do not exceed $0^m.01-0^m.05$ in any of the bands. Descriptions of the observing techniques, instrumental parameters, and data accumulated in 1985–1997 can be found in [1, 2, 7, 8].

Table 1 presents the results of the $JHKLM$ photometry of FG Sge obtained in 1998–2001. This table gives the photometric uncertainties together with the magnitudes. Figures 1 and 2 display light curves and color curves for the entire time interval covered by our observations, 1985–2001. The horizontal lines show the mean levels of the $JHKLM$ brightnesses of FG Sge prior to Autumn 1992. The numbers from *1* to *12* mark characteristic episodes in the J variations; the data indicated by the number *2* were obtained by Woodward *et al.* [4] in September–October 1992. Our 1993–1997 data (before the vertical dashed lines in Figs. 1 and 2) were analyzed in [7, 8].

3. NEAR-IR BRIGHTNESS AND COLOR VARIATIONS OF FG Sge IN 1985–2001

During our 1985–1989 infrared observations of FG Sge, the variations in the star's photometric behavior, though unique, were not catastrophic. The observed changes in the IR brightness of FG Sge for the previous ~ 15 years (1970–1985) suggest the star was evolving towards the red-giant (supergiant) stage. On average, the decrease of the star's effective temperature was accompanied by its expansion (T_{eff} changed from 7500 to 5600 K and the radius increased by almost a factor of 1.7 in 15 years), whereas changes in the star's luminosity did not exceed 10 % in 15 years. Observations obtained in 1985 indicated that the luminosity, radius, and M_{bol} (for $r = 4.1$ kpc) were close to those typical of a normal G1I supergiant. In the character of its variability in 1985–1986 (Sp(min) ~ G2I, Sp(max) ~ F5I, $P \sim$ 115 days), FG Sge resembled semiregular variables intermediate between δ Cep and SRd [1, 9]. The mean spectral type of FG Sge in 1985–1989 derived from the JHK photometry was G0I, with variations from maximum to minimum not exceeding 0.2 of a spectral type. At the same time, the UBV data implied a much later spectral type, about K0. This discrepancy was explained by the presence of anomalous line absorption in the B and U bands, due, in turn, to peculiarities of the chemical composition of FG Sge during this time interval [2].

Before analyzing our observations further, we will refine the main parameters of FG Sge in 1989, the last year of our IR observations prior to the autumn of 1992. The averaged observations of FG Sge for 1989 [2] are presented in the second column of Table 2. The subsequent columns give the same values corrected for interstellar extinction with $E(B-V) =$ 0.4, their standard errors, and the number of nights used for the average. Using the data of Table 2, we plotted the $0.36-5$ μm SED, which demonstrates that the radiation of FG Sge in 1989 could be represented with the spectrum of a normal G(0 ± 1) supergiant. The mean integrated flux from FG Sge in 1989 computed from the observed SED taking into account the contribution of the radiation at $0.36-5$ μm to the integrated flux for a source temperature of 5800 K (G0I), was F_{int}(FG Sge) $= (2.1 \pm 0.1) \times 10^{-8}$ erg s^{-1}cm^{-2}. Taking into account the radiation at $\lambda > 5$ μm adds less than 1 % to the integrated flux of a source with a temperature exceeding 5500 K. The luminosities of normal F5 to G5 supergiants are almost independent of the spectral type, and equal to $6300L_{\odot}$ [10]. Thus, for L(G0I) $= 6300L_{\odot} = 2.43 \times 10^{37}$ erg/s, the distance to FG Sge is $r = [L(\mathrm{G}(0 \pm 1)$ I$)/4\pi F_{\mathrm{int}}$(FG Sge)$]^{0.5} = 3.1 \pm 0.1$ kpc, and the radius of the supergiant is $R^* = (5.4 \pm 0.5) \times 10^{12}$ cm.

The lower part of Table 2 collects the principal parameters of FG Sge derived from the 1989 observations. Given their errors, the estimates of the parameters of FG Sge derived from the mean SED for 1985–1989 can be considered close to these values. The mean parameters of the relatively hot, optically thin circumstellar dust envelope revealed by our IR photometry in 1985–1989 are presented by Arkhipova and Taranova [2]. The only way to estimate the parameters of the dust envelope in 1989 is from its emission in the M band (5 μm), since the 3.5 μm emission of the dust envelope could be estimated only with a large uncertainty. The flux from the dust envelope can be defined as the difference between the observed M flux and its value for a normal G0 supergiant; the mean value of this quantity is $F_{\mathrm{d}}(M) \sim 3.7 \times 10^{-11}$ erg s^{-1}cm^{-2} μm^{-1}. Assuming that the temperature of the physically thin dust envelope was ~ 1000 K in 1989 [2], we can estimate its optical depth at 5 μm:

$$\tau_M \approx (r/R_{\mathrm{d}})^2 [F_{\mathrm{d}}(M)/B(M, T_{\mathrm{d}})] \approx 2.5 \times 10^{-3}, \tag{1}$$

where R_{d} is the radius of the dust envelope ($R_{\mathrm{d}} \approx (R^*/2)(T^*/T_{\mathrm{d}})^{2.9} \approx 4.4 \times 10^{14}$ cm for graphite grains)

Table 1. $JHKLM$ photometry of FG Sge in 1998−2001

Julian date	J	$\sigma(J)$	H	$\sigma(H)$	K	$\sigma(K)$	L	$\sigma(L)$	M	$\sigma(M)$
2450977.520	9.65	0.04	8.12	0.02	6.26	0.01	4.17	0.03	4.60	0.09
2450978.523					6.24	0.01	3.82	0.04		
2450981.476					6.28	0.01	4.22	0.01		
2451006.518	9.72	0.05	8.16	0.07	6.02	0.01	3.92	0.03	3.55	0.11
2451009.431	9.93	0.03	8.16	0.03	6.20	0.01	4.09	0.01	3.75	0.04
2451010.444	9.97	0.06	8.31	0.05	6.20	0.01	4.39	0.05	3.92	0.09
2451034.417	9.89	0.09	8.27	0.04	6.09	0.02	4.05	0.01	3.56	0.05
2451036.395	10.01	0.05	8.05	0.03	6.07	0.02	3.98	0.02	3.59	0.04
2451038.365	10.02	0.05	8.01	0.01	6.14	0.01	4.15	0.04	3.52	0.04
2451040.383	10.15	0.07	8.14	0.03	6.03	0.02	4.06	0.04	3.18	0.11
2451062.346	10.01	0.05	8.16	0.02	6.26	0.02	4.05	0.01	3.42	0.05
2451068.311	9.83	0.05	8.24	0.02	6.27	0.03	4.11	0.03	3.38	0.04
2451069.319	9.81	0.05	8.10	0.04	6.32	0.02	4.17	0.02	3.59	0.04
2451071.299					6.24	0.02	4.20	0.02		
2451072.286	9.75	0.05			6.24	0.02				
2451093.282	9.24	0.02	7.76	0.01	6.08	0.01	4.04	0	3.40	0.04
2451124.174			7.98	0.07	6.22	0.04	4.10	0.02		
2451152.188	9.19	0.05	7.56	0.02	5.92	0.01	4.06	0.02	3.59	0.04
2451174.174	8.39	0.02	7.28	0.02	5.95	0.01	4.11	0.01	3.59	0.04
2451300.572	7.11	0.01	6.35	0	5.52	0	3.95	0.01	3.55	0.02
2451328.518	7.23	0	6.36	0.02	5.53	0	3.85	0.01	3.40	0.01
2451352.515	7.06	0.05	6.28	0.01	5.25	0.02	3.69	0.03	3.46	0.02
2451359.505	7.14	0.01	6.24	0.01	5.24	0.01	3.67	0.01	3.36	0.02
2451360.534	7.14	0.01	6.19	0.01	5.27	0.01	3.67	0.02	3.38	0.02
2451366.510	7.18	0.02	6.18	0.02	5.25	0.02	3.65	0.01	3.33	0.02
2451383.436	7.24	0.01	6.26	0.01	5.27	0	3.63	0.01	3.34	0.02
2451393.415	7.32	0.01	6.32	0.01	5.32	0.02	3.62	0.01	3.39	0.02
2451420.340	7.20	0.01	6.30	0.01	5.22	0.01	3.53	0.01	3.23	0.01
2451451.249	8.92	0.03	7.15	0.01	5.56	0.02	3.60	0.02	3.25	0.02
2451452.326	9.22	0.05	7.30	0.02	5.54	0.03	3.61	0.02	3.28	0.03
2451455.235	8.96	0.02	7.24	0.02	5.51	0.01	3.61	0.02	3.13	0.02
2451505.157	9.29	0.03	7.46	0.01	5.75	0.01	3.67	0.01	3.25	0.02
2451649.578	7.35	0.01	6.54	0.01	5.54	0	3.70	0.01	3.22	0.02
2451685.514	7.32	0.01	6.53	0.01	5.57	0.01	3.74	0.01	3.27	0.02
2451706.530	7.26	0.01	6.48	0.01	5.46	0.01	3.70	0.01	3.09	0.02
2451711.518	7.23	0.01	6.45	0.01	5.46	0.01	3.68	0.02	3.16	0.02
2451737.472	6.93	0.01	6.20	0.01	5.35	0.01	3.63	0.02	3.14	0.02
2451767.370	6.90	0.02	6.19	0.02	5.35	0.02	3.64	0.02	3.17	0.04
2451773.355	6.91	0.01	6.22	0.02	5.32	0.01	3.68	0.02	3.22	0.06
2451779.342	6.94	0	6.22	0.01	5.29	0.01	3.62	0.01	3.14	0.04
2451801.278	7.13	0.01	6.30	0.01	5.32	0.01	3.60	0.01	3.16	0.02
2451831.219	7.25	0.02	6.44	0.02	5.34	0.02	3.78	0.02	3.26	0.02
2451834.224	7.24	0.01	6.40	0.01	5.42	0.01	3.70	0.01	3.19	0.02
2451856.202	6.98	0.01	6.27	0	5.36	0	3.66	0.01	3.24	0.01
2451865.202	6.88	0.01	6.18	0.01	5.3	0.01	3.6	0.01	3.21	0.01
2451868.186	6.88	0.01	6.17	0.01	5.33	0.01	3.65	0.01	3.1	0.02
2451888.163	6.94	0.01	6.26	0.01	5.42	0.01	3.64	0	3.17	0.02
2452093.465	−	−	7.84	0.02	5.88	0.02	3.63	0.02	3.08	0.02
2452117.459	10.42	0.08	8.04	0.02	6.08	0.02	3.67	0.01	3.19	0.04
2452130.327	−	−	−	−	6.19	0.03	3.81	0.02	−	−
2452132.399	10.16	0.12	8.15	0.02	6.15	0.01	3.74	0.01	3.28	0.04
2452133.412	10.38	0.11	8.16	0.02	6.16	0.01	3.74	0.02	3.23	0.02
2452154.346	10.2	0.09	8.29	0.02	6.18	0.01	3.74	0.01	3.15	0.03
2452163.326	10.18	0.08	8.29	0.02	6.2	0.01	3.75	0.01	3.36	0.03
2452186.317	10.69	0.16	8.34	0.02	6.23	0.01	3.83	0	3.31	0.03
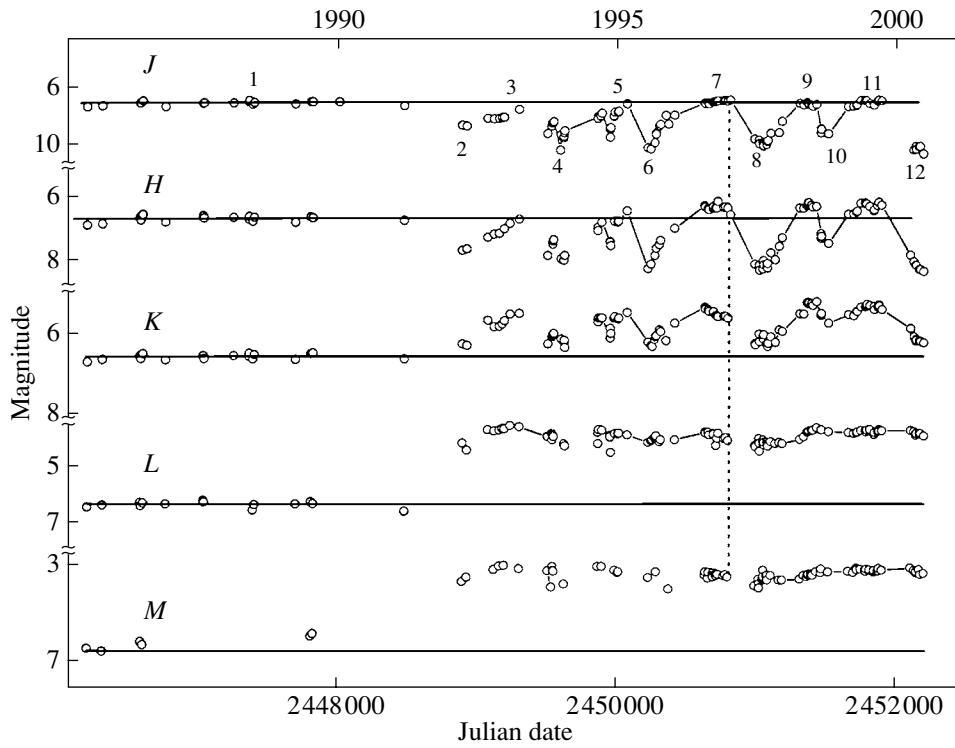
Fig. 1. Variations of the $JHKLM$ brightness of FG Sge in 1985–2001. The horizontal lines are the star's mean brightness levels prior to August 1992. Other notation is explained in the text.
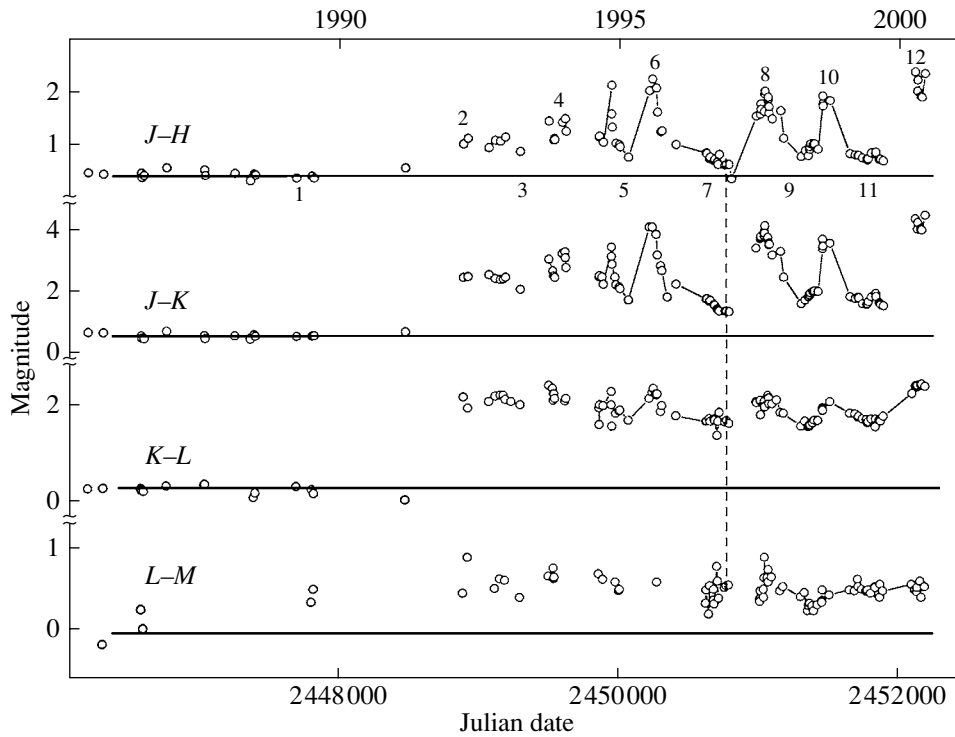
Fig. 2. Variations of the IR color indices of FG Sge in 1985–2001. The notation is the same as in Fig. 1.

Table 2. Mean IR magnitudes and main parameters of FG Sge in 1989

Parameter	m_{obs}	m_0	se	n
U	11.97	10.06	0.07	3
B	10.84	9.22	0.06	3
V	9.06	7.84	0.06	3
J	7.06	6.76	0.04	3
H	6.70	6.52	0.05	3
K	6.53	6.42	0.05	3
L	6.27	6.22	0.02	3
M	5.85	5.82	0.04	2
Sp	G(0 ± 1) I			
$L, L_\odot$	6300			
F_{int}, erg/s	$(2.1 \pm 0.1) \times 10^{-8}$			
r, kpc	3.1 ± 0.1			
R^*, cm	$(5.4 \pm 0.5) \times 10^{12}$			

and $B(M, T_d)$ is the M emission of a black body with the temperature T_d.

The optical depth of the dust envelope at 5 μm estimated from the mean value of the excess radiation for 1985−1989 was $\sim 1.4 \times 10^{-3}$. Thus, the optical depth of the FG Sge dust envelope at 5 μm in 1989 was twice its mean value for 1985−1989. A trend toward increasing dust-envelope emission in 1989 can also be noted in Fig. 2, based on the increase of the $L-M$ color index in 1989. If the average (over the spectrum of the supergiant) optical depth of the dust envelope corresponds to the value at ~ 0.55 μm, then this mean value was τ(mean, 1989) $\sim (5\,\mu m/0.55\,\mu m)^2 \tau(M, 1989) \approx 0.2$, and the integrated flux from the dust envelope in 1989 was $\sim 4 \times 10^{-9}$ erg s^{-1} cm^{-2}.

Let us now turn to the analysis of our IR observations of FG Sge after August 1992. Unfortunately, no detailed IR light curves of FG Sge were obtained in 1990−1991 or in July−September 1992, so we must compare the star's state after August 1992 with its state in 1989. It appears from Figs. 1 and 2 that the first minimum of the J brightness, recorded in the observations of Woodward *et al.* [4], coincides with the abrupt decrease of the optical brightness of FG Sge in Autumn 1992 [9].

The mean J brightness during the maxima of 1993−2001 (Fig. 1) was close to its value for 1985−1989. At the same time, the maximum $HKLM$ brightnesses were higher than the mean values for 1985−1989, with the difference increasing with the wavelength. In addition, the excess of the brightness above this previous mean level was accompanied by "smearing" of the brightness minima in the L and M bands. For example, the amplitude of the J brightness variations in 1995−2001 was about $3^m\!.5$, but the variations of the L and M brightnesses were within 1^m. As a result, the star appears strongly reddened after Autumn 1992 compared to its state in 1985−1989 (Fig. 2). The minimum reddening since Autumn 1992 has been observed during J-brightness maxima (Fig. 2). The maximum dimming of the star at phases of minima was observed in the J band. Further, at wavelengths $\lambda > 2.2$ μm (K band), the star's maximum and minimum brightnesses both begin to exceed the mean brightness level prior to Autumn 1992. We can see in Fig. 1 that the amplitudes of variations in the J, H, and K bands from August 1999 until the end of our observations (October 2001) were not lower than in 1994−1999. However, the variations of the L and M brightnesses became significantly weaker and, beginning in August 1999, the mean brightness level increased somewhat compared to 1993−1999. The situation with the supergiant after August 1992 is not definitely known, though photometric and spectroscopic optical observations (cf., for instance, [6]) indicate that, since Autumn 1992, FG Sge (the central star of the planetary nebula) has been in a state similar to R CrB stars, whose observed variability is mainly due to the quasi-periodic formation of their circumstellar dust envelopes.

4. ANALYSIS

3.5−5 μm. It is evident that the emission from the dust envelope that formed around FG Sge in August 1992 becomes pronounced at wavelengths $\lambda > 2$ μm, namely, in the range 3.5−5 μm. Moreover, we can conclude from the data in Table 1 and Figs. 1 and 2 that, after August 1992, the L and M radiation from FG Sge is mainly due to the dust envelope. This follows from a comparison of the observed color indices, $K-L$ (>1) and $L-M$ (>0), with their values for normal stars (including carbon stars), which do not exceed $0.2\ldots 0.4$ and $-0.5\ldots -0.2$. In addition, the star's brightness at 3.5 μm (L) had increased by nearly $2^m\!.5$ by Autumn 1992; it had grown by another $0^m\!.8$ by September 1993, and then exhibited variations with an amplitude of about $0^m\!.5$ about its mean level, $3^m\!.8$, until the end of 2001.

The brightness variations at 1.25 μm (J band) were quite different. The brightness changes in 1992−2001 exceeded $2^m\!.5$, and the maximum J brightness was higher than the level of 1985−1989. If we attribute all the J radiation to the F0−K5 supergiant, then the star's L brightness will be $5^m\!.8$−$6^m\!.3$,
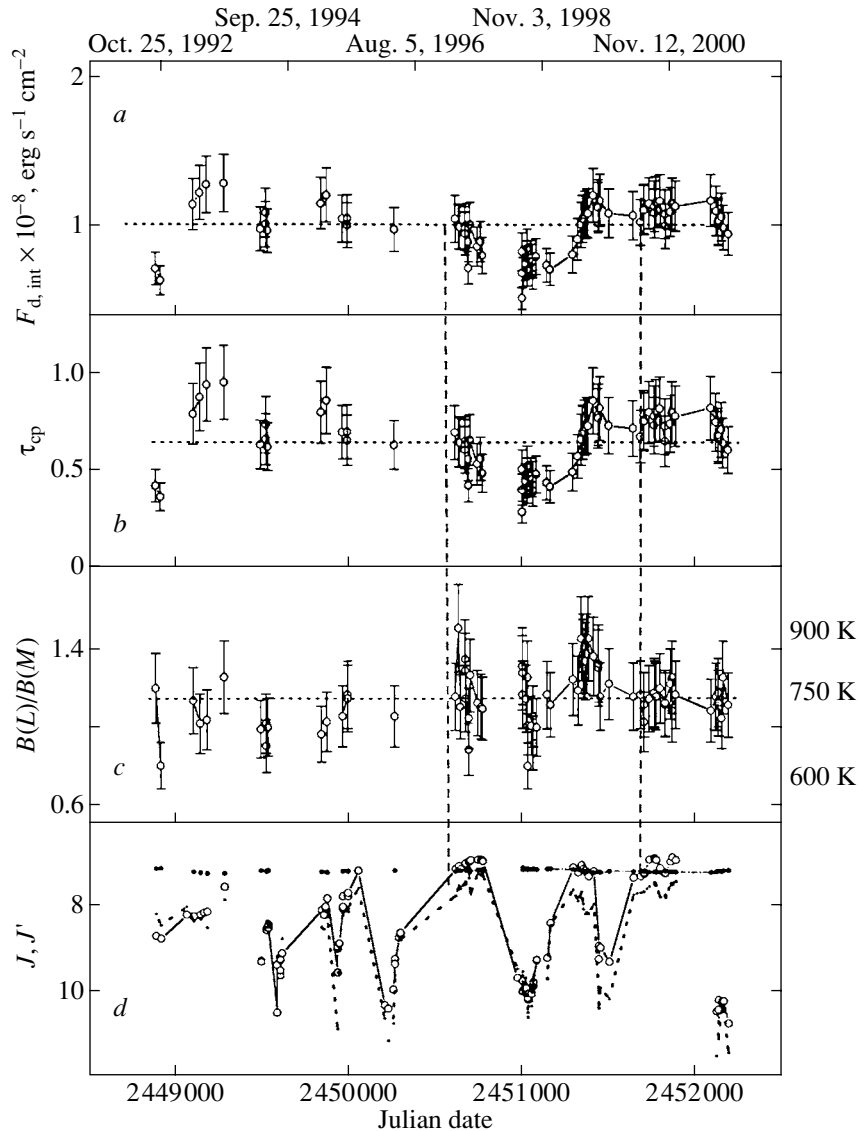
Fig. 3. Variations of some parameters of the dust envelope of FG Sge in 1992−2001: (a) the integrated flux, (b) the mean optical depth, (c) the temperature of the graphite grains, and (d) a comparison between the observed and model variations of the J brightness (see text for details).

even at the maximum J brightness. The observed L brightness of FG Sge in 1992−2001 varied in the range $3^m5−4^m1$, so that the contribution of the dust-envelope emission in the L band exceeded 80% of the observed L flux. The same is true at 5 μm (the M band), where the contribution from the dust envelope exceeded 90%.

The most plausible explanation for the appearance of the cirumstellar dust envelope in Autumn 1992 is the condensation of dust grains at some distance from the star, either as a result of a long-term accumulation to a critical level (e.g., via the stellar wind from the supergiant) or due to an abrupt ejection of matter from the supergiant. The emission from the dust grains in the envelope is due to heating by

short-wavelength radiation from the supergiant. If the energies absorbed and re-radiated by the dust grains are in balance, we can write for a physically thin dust envelope

$$F_{int}^* \approx F_{int}^* e^{-\tau_{mean}} + F_{d, int}$$

and

$$\tau_{mean} \approx -\ln[(F_{int}^* - F_{d, int})/F_{int}^*], \qquad (2)$$

where F_{int}^* and $F_{d, int}$ are the integrated fluxes from the star and the dust envelope and τ_{mean} is the mean optical depth of the envelope.

For the value of F_{int}^*, we will assume the mean integrated flux of FG Sge in 1989.

Integrated flux from the dust envelope in 1992−2001. This flux can be estimated as follows:

—subtract the mean 1989 values from the fluxes observed at 3.5 and 5 μm;

—attribute the resultant fluxes at 3.5−5 μm to the dust envelope and estimate its integrated flux in 1992−2001 from the relation

$$F_{d, int} = (1/A) \sum \{[F_d(L) + F_d(M)][\Delta\lambda/2]\}, \quad (3)$$

where $F_d(L)$ and $F_d(M)$ are the fluxes from the dust envelope at 3.5 and 5 μm, $\Delta\lambda = 5−3.5$ μm, and A is the fraction of the radiation at 3.5−5 μm as part of the integrated radiation.

The fraction of the integrated blackbody radiation flux at 3.5−5 μm is $0.23 \pm 0.03\%$ over a wide range of temperatures characteristic of dust envelopes (500−1500 K). Therefore, the accuracy of our estimate of $F_{d, int}$ depends on the estimate of the fraction of the star's radiation in the L band, for which the accuracy is no worse than 15%.

Figure 3a shows the variations of $F_{d, int}$ in 1992−2001 together with the corresponding uncertainties. The minimum flux shown corresponds to the mean integrated flux from the dust envelope in 1989 ($\sim 4 \times 10^{-9}$ erg s^{-1} cm^{-2}, see above), and the maximum flux to the mean of the integrated flux from the star in 1989 ($\sim 2.1 \times 10^{-8}$ erg s^{-1} cm^{-2}). The horizontal dashed line is the mean level of the integrated flux from the dust envelope in 1992−2001. This figure shows that this integrated flux varied by a factor of 1.5−2 in 1992−2001.

Figure 3b displays variations of τ_{mean} in the range 0.5−1.0 in 1992−2001. If we assume, as earlier, that τ_{mean} corresponds to ~ 0.55 μm and that the dust grains in the envelope resemble graphite grains in terms of their optical properties [i.e., the wavelength dependence of the extinction factor can be represented as $Q_\lambda \propto \lambda^{-2}$ ($\tau_\lambda \propto Q_\lambda$)], then the optical depth of the envelope at 3.5−5 μm will definitely be less than unity. In this case, the flux from the dust envelope in this range can be written

$$F_d(\lambda) \propto B(T_d, \lambda)\tau_\lambda,$$

and

$$B(T_d, L)/B(T_d, M) = [F_d(L)/F_d(M)](3.5/5)^2. \quad (4)$$

We can estimate the blackbody temperature of the dust grains in the envelope from the ratio of the envelope fluxes at 3.5 and 5 μm. Figure 3c presents the variations of $B(T_d, L)/B(T_d, M)$ observed in 1992−2001. To the right are plotted the blackbody temperatures for several values of $B(T_d, L)/B(T_d, M)$. As in Fig. 3a, the dashed horizontal lines show the corresponding mean values.

Thus, we can draw the following conclusions from Figs. 3a−3c in a model with a physically thin dust envelope consisting of graphite grains, provided that its emission is in radiative equilibrium with the radiation of the supergiant, whose luminosity remained constant in 1989−2001.

The variations of the integrated flux from the dust envelope (its luminosity, Fig. 3a) reveal a "periodic" component with a time scale of about 2100 days and flux variations by a factor about 1.5. The dust-envelope luminosity nearly doubled in Autumn 1992 (compared to 1989) and then nearly doubled again by Autumn 1993. By Autumn 1994, it decreased by almost 40% and again increased by 20−30% by Summer 1995. In Spring 1995, it dropped to its mean value, and then may have remained almost constant until Autumn 1997. Further, the dust-envelope luminosity dropped by approximately 40% over 350−360 days, increased again by more than 50% 250−300 days later, and remained almost unchanged until 2001, when it decreased by $\sim$20%. The character of the dust-envelope luminosity variations in 1998−2001 is remarkably similar to the changes observed earlier, from Autumn 1992 until 1995.

The spherically symmetrical dust envelope observed in August 1992 reached its maximum density ($\tau_{mean} \sim 1$) in the second half of 1993. The envelope was dispersing at that time, and its density reached the level of August 1992 by Autumn 1998. Later, an injection of dust material into the envelope was observed. As a result, its density doubled within several hundred days and remained almost unchanged until the end of 2000. It is possible that the dust envelope began to disperse again in 2001. The variations of the mean optical depth of the dust envelope (Fig. 3b) in 1992−2001 repeat the variations of the integrated flux (2) in a natural way.

The mean temperature of the dust envelope is about 750 K, and the temperature varies from 600 to 900 K. It is possible that the dust envelope's temperature increased somewhat in Summer 1997 compared to its mean value. It returned to its mean value in Autumn 1998 then increased somewhat again in Autumn 1999 and gradually returned to its mean value by the end of 2001.

The most characteristic episode in the variations of these parameters was observed from Summer 1997 until Autumn 1999. This time interval is indicated by the vertical dashed lines in Fig. 3.

1.25−2.2 μm. Remember that our estimates of τ_{mean} were derived from data on the dust-envelope emission at 3.5−5 μm. Therefore, if the envelope is spherically symmetrical, the observed variations of τ_{mean} should also be reflected in the brightness variations of FG Sge at wavelengths shorter than 3.5 μm.

Table 3. Mean IR magnitudes of FG Sge (corrected for interstellar extinction) prior to August 1992 and for six episodes (Figs. 1, 2) after August 1992

Filter	Brightness prior to August 1992		Brightness maxima						Brightness mimima					
			Episode											
			7		9		11		8		10		12	
			JD24…											
	47200		50740		51340		51770		51050		51460		52140	
	m	se	m	se	m	se	m	se	m	se	m	se	m	se
J	6.78	0.03	6.65	0.01	6.83	0.02	6.62	0.01	9.75	0.02	8.80	0.09	10.03	0.08
H	6.48	0.02	6.15	0.04	6.08	0.03	6.02	0.01	7.91	0.03	7.10	0.06	8.02	0.05
K	6.44	0.02	5.47	0.01	5.23	0.06	5.21	0.01	6.01	0.05	5.48	0.05	6.06	0.02
L	6.25	0.03	3.88	0.06	3.69	0.05	3.59	0.01	4.00	0.03	3.57	0.02	3.70	0.02
M	6.0	0.11	3.35	0.02	3.38	0.03	3.13	0.02	3.39	0.07	3.19	0.03	3.22	0.03
N	5.4		2.45		2.8		2.4		2.5		2.5		2.3	
Q	5.4		2.45		2.8		2.4		2.5		2.5		2.3	
F_{int}, $10^{-8}\,\text{erg}\,\text{s}^{-1}\,\text{cm}^{-2}$	1.8		1.8		1.8		2.0		8.3		1.2		9.7	

For graphite grains, $(Q_\lambda \propto \lambda^{-2})$, and, if the values of τ_{mean} correspond to a wavelength of $\sim 0.55\ \mu$m, we can write

$$\tau(J) \approx (0.55/1.25)^2 \tau_{\text{mean}}$$

or

$$\Delta J \approx 1.086\tau(J). \quad (5)$$

Such variations of the J brightness should be observed during changes of the optical depth of the spherically symmetrical dust envelope derived from its emission at $3.5{-}5\ \mu$m. The open circles in Fig. 3d show the variations of the J brightness observed in $1992{-}2001$ and the filled circles the J variations derived from (5) with the mean J brightness for 1989 added. It is evident that the changes of the optical depth implied by the analysis of the observed emission from the dust envelope can explain only small variations of the J brightness near its maxima, and the observed variations (dips) of the J brightness cannot be explained by the model for the spherically symmetrical dust envelope.

Six episodes of decreasing JHK brightness (Fig. 1, the episodes with even numbers) were accompanied by reddening at these wavelengths. This can be explained in two ways.

(1) The star itself becomes redder. This can be ruled out: for example, the maximum values of $J{-}H$ for normal stars do not exceed 1^m, whereas the values observed during JHK minima are more than 2^m.

(2) The optical depth of the dust envelope increases. If the bulk of the dust envelope were participating in such an increase, it would have led to a synchronous brightness increase at $3.5{-}5\ \mu$m. However, a slight decrease rather than an increase is observed (Fig. 1, the episodes with even numbers). In other words, first, there must be an increase of the optical depth of the dust envelope along the line of sight and, second, the associated dust cloud makes up a small part of the dust envelope as a whole. Let us assume that the optical depth of the dust cloud is roughly an order of magnitude higher than the mean optical depth of the spherically symmetrical dust envelope and that the cloud's emission is not detected; i.e., its contribution to the total radiation of the dust envelope at $3.5{-}5\ \mu$m is within the observational errors, which do not exceed 5%. In other words, the ratio of the fluxes from the cloud and envelope should be no more than several hundredths, in which case the ratio of the sizes of the cloud and the envelope for the same grain temperatures will be $R_{cl}/R_{DE} < 0.05$, and we obtain for $R_{DE} \sim 4 \times 10^{14}$ cm the ratio $R_{cl} < 2 \times 10^{13}$ cm $\approx 280R_\odot$. It is most likely that the dust cloud condenses and dissipates within the spherically symmetrical dust envelope; however, the formation of such compact, dense clouds within dust envelopes requires a separate study.

The attenuation of the supergiant's J brightness by the graphite-grain dust cloud that appears in the line of sight will approximately follow the law

$$J' = J_0 + A'(J) \approx J_0 + 2.35 \times ((J{-}H) - 0.4), \quad (6)$$

$F(\%)$, erg s^{-1} cm^{-2} μm^{-1}
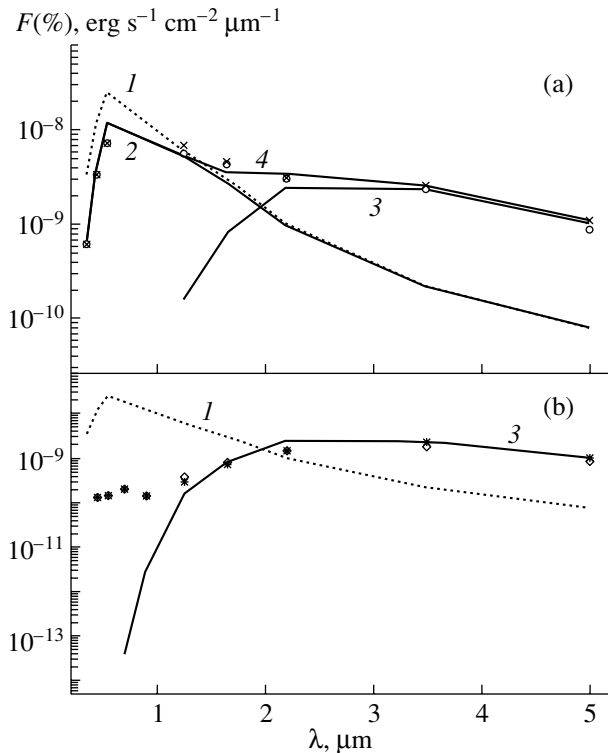
Fig. 4. The mean SED of FG Sge in 1989 at (a) maxima and (b) minima of the J brightness after August 1992 (see the text for the meaning of the various symbols). Curves $1-4$ are the SEDs for a G0 supergiant, G0 supergiant attenuated by a dust envelope, dust envelope, and model source.

where $J-H$ are the color indices observed in 1992–2001; $J_0 \approx 7^m05$ and $(J-H)_0 \approx 0^m4$ are the mean values for 1989. In Fig. 3d, the J' values are plotted as small asterisks; we can see that the observed J variations are in good agreement with the variations computed from (6). In other words, the emission from a spherically symmetrical dust envelope with sufficiently dense, compact dust clouds with characteristic sizes of several hundred solar radii can describe the brightness and color variations of FG Sge at 1.25–5 μm observed in 1992–2001 fairly well.

For example, according to (6), the optical depth of the dust envelope at $\lambda = 1.25$ μm during the latest J brightness minimum (episode 12 in Fig. 1) was $\tau_{1.25} \approx 0.92 A'(J) \approx 0.92[2.35 \times ((J-H)_{ep.\,12} - 0.4)] \approx 4.3$, or $\tau_{mean} \approx \tau_{0.55} \approx (1.25 \times 0.55)^2 \tau_{1.25} \approx 22$. Thus, the optical depth of the dust cloud is much higher than the optical depth of the dust envelope of FG Sge.

In reality, the optical depth of the dust cloud must be somewhat different from this, as will be demonstrated by our further analysis.

The SED and integrated fluxes of FG Sge in 1985–2001. The circles and crosses in Fig. 4a dis-

play the observed SEDs of FG Sge for two maxima of the J brightness (episodes 9 and 11 in Fig. 1). The diamonds and asterisks in Fig. 4b show the SEDs of FG Sge observed in two minima of the J brightness (episodes 8 and 12 in Fig. 1). The dotted curves 1 in Figs. 4a, 4b show the mean SED of the supergiant in 1989.

The mean SED at 0.36–5 μm at the J-brightness maxima (Fig. 4a) can be reproduced with a sum of the radiation of the G0 supergiant (curve 1) attenuated by a dust envelope with the mean optical depth ~ 0.65 (curve 2) and the emission of the spherically symmetrical dust envelope itself (curve 3), with the temperature of its graphite grains being ~ 750 K. Curve 4 is the SED of the combined radiation; deviations from the observed SED are within 10–15% of the flux, and the integrated fluxes coincide to within 5%. Analysis of the SED of FG Sge during other maxima of the J brightness using the adopted simple model (star + dust envelope) leads to similar results, with some differences (Fig. 3) in the derived temperatures of the graphite grains (750 ± 150 K) and in the mean optical depth of the dust envelope (0.65 ± 0.15).

The parameters of the dust envelope during J-brightness minima are virtually the same as during J-brightness maxima (Fig. 3). In Fig. 4b, curve 3 represents the SED of the dust envelope computed for the maximum J brightness (Fig. 4a); we can see that, in addition to the fluxes observed at 3.5 and 5 μm, the 1.65 and 2.2-μm fluxes observed during the minima J brightness also follow this curve. In other words, only emission from the spherically symmetrical dust envelope is observed at 1.65–5 μm during J-brightness minima. The radiation of the supergiant is barely detectable at 1.25 μm and possibly in the optical; we did not correct the $BVRI$ fluxes used for the optical minimum for the contribution of the nebula, and, in reality, there is almost no radiation from the supergiant itself in these filters. The integrated 0.45–5 μm radiation flux of FG Sge at J minima is almost half that at J maxima. This decrease of the integrated flux from maximum to minimum J brightness can easily be explained: only the emission from the spherically symmetrical dust envelope is observed at minimum J brightness, while the supergiant is screened by the dense dust cloud, whose optical depth was probably underestimated above.

This conclusion is supported by the integrated fluxes of FG Sge for the six most characteristic episodes of its 1989–2001 photometric behavior, presented in Table 3. This table contains the mean IR magnitudes of FG Sge prior to August 1882 and during six episodes (Figs. 1, 2) after August 1992 (corrected for interstellar extinction with $E(B-V) = 0.4$). To facilitate estimation of the integrated fluxes, the same table presents (in italics) the N (10 μm)
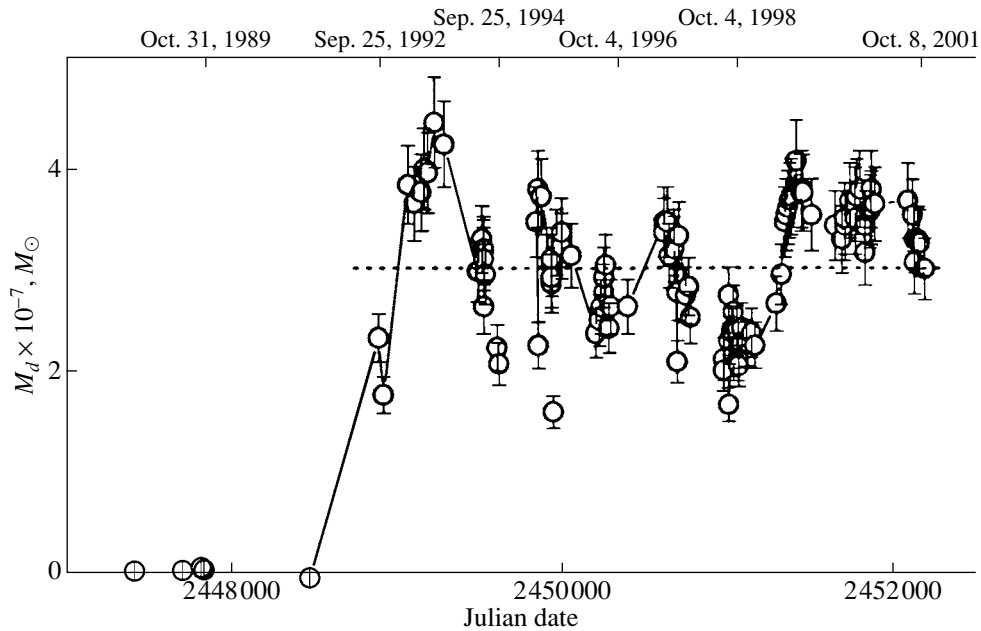
Fig. 5. Variations of the mass of the spherically symmetrical dust envelope of FG Sge in 1992−2001.

and Q (20 μm) magnitudes derived for the color temperatures corresponding to the $L-M$ color index. These N and Q magnitudes are somewhat over-estimated, since the contribution of the star itself (which is hotter than the dust envelope) is not taken into account in the L and M fluxes. However, more accurate estimationn of the N and Q magnitudes will not change the integrated fluxes by more than 2−5%. The last line of the table contains the integrated fluxes computed for each interval.

The mass of the dust envelope. If the dust envelope consists of dust grains heated to ~ 750 K, its mass can be determined using the following relation of Williams and Longmore [11]:

$$4\lambda r^2 F_d(L) = 1400 M_d B(T_d, L).$$

We have for $r = 3.1$ kpc

$$M_d \approx [8.2 \times 10^{41} F_d(L)]/2.9 \times 10^6 \quad (7)$$
$$\approx 2.8 \times 10^{35} F_d(L) \approx 140 F_d(L) M_\odot,$$

where $F_d(L)$ is the L flux from the dust envelope in erg s^{-1} cm^{-2} μm^{-1}.

Figure 5 shows the variations of the mass of the spherically symmetrical dust envelope of FG Sge in 1989−2001 computed using (7) and the data in Table 1. Several conclusions follow from Fig. 5: (i) the mean mass of the spherically symmetrical dust envelope in 1992−2001 was $(3 \pm 1) \times 10^{-7} M_\odot$; (ii) variations of the envelope's mass were in the range $(2-4) \times 10^{-7} M_\odot$, i.e., the envelope's mass varied by a factor of two in this time interval; (iii) the
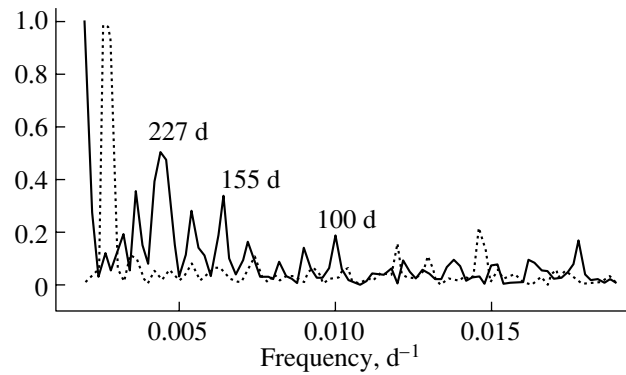

Fig. 6. Power spectrum and spectral window (dashed line) from J photometry of FG Sge in 1992−2001.

figure reveals several episodes of injection of dusty material into the envelope (JD 2448480−2449220, JD 2449620−2449860, JD 2450263−2440850, JD 2451037−2451422) and of the envelope's dissipation. The mean rate of injection of matter into the envelope was $9.6 \times 10^{-8} M_\odot$/yr. The mean rate of dissipation of the dust envelope was about $1 \times 10^{-7} M_\odot$/yr. If the gas-to-dust ratio in the envelope is ~ 100, the supergiant lost about $8.7 \times 10^{-5} M_\odot$ in 1992−2001.

Returning to Figs. 1 and 2, we conclude that most of the spherically symmetrical dust envelope formed over a time scale shorter than 500 days, and that the initial mass-loss rate by the supergiant exceeded $2 \times 10^{-7} M_\odot$/yr. Later, the rates of injection of matter into the dust envelope and of dissipation of the envelope remained approximately equal at a value that was
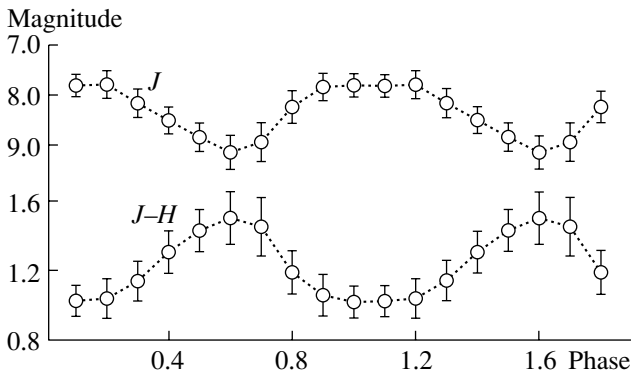
Magnitude

Fig. 7. Phase curves of J and $J-H$ for 1992−2001 folded with the 227-day period.

about half the initial value, so that the injection and dissipation began to slow by 1999, and the spherically symmetrical dust envelope was relatively stationary from 1999 to the middle of 2001. Thus, the initial ejection of matter by the supergiant in Autumn 1992 and the supergiant's variable stellar wind were able to support the dust envelope at least until October 2001 (the end of our observations).

Possible variations of the supergiant's parameters. As is noted above, the 1.25−1.65-μm radiation during J-brightness maxima is due primarily to the supergiant. Knowing the mean optical depth of the spherically symmetrical dust envelope, we can estimate the main parameters of the supergiant by assuming that its 1992−2001 luminosity remained at the 1985−1989 level (Table 3). During brightness maxima, the mean J magnitude of FG Sge is $\sim 6^m65$, and the mean $J-H$ color index is $\sim 0^m62$ (Table 3). Taking into account absorption in the dust envelope, these values are 6^m52 and 0^m56. This color index, $J-H \sim 0^m56$, agrees with values expected for K3 supergiants, so that, compared to 1985−1989, the supergiant became cooler by approximately 1500 K. However, its mean J brightness at the maxima of 1992−2001 did not decrease by $\sim 1^m$ (as expected from the change of the temperature) but instead increased by $\sim 0^m25$. In other words, the supergiant expanded as it cooled, with its radius increasing by almost a factor of 1.6 at constant luminosity. Note that, like the formation of the spherically symmetrical dust envelope, the supergiant's cooling and expanding occurred during the first several hundred days, and these processes were probably synchronous.

Pulsations of the IR brightness of FG Sge after August 1992. Both before and after August 1992, no strict periodicity was observed in the IR brightness variations of FG Sge. The mean value of the quasi-period in 1985−1989 was 110 days. It varied primarily between 90 and 120 days, and nearly

reached 150 days in 1989 [11]. After August 1992, a 400−800-day time scale for the JHK brightness variations is visible in the light and color curves (Figs. 1, 2). A detailed analysis of the 1992−2001 photometric data for FG Sge reveals the presence of a ~ 230-day "period" in the JHK brightnesses. This is approximately twice the pulsation time scale in 1985−1989. For this analysis, we applied software developed at the Sternberg Institute by V.M. Lyutyĭ for searches for periods in the brightness variations of unstable stars. Figure 6 shows the power spectrum and spectral window derived from our 1992−2001 J photometry of FG Sge. All periodic components and their reliabilities are easy to see. The power spectra and spectral windows are plotted for frequencies between 0.002 and 0.02 d^{-1}, with the frequency resolution being ~ 0.0002. The J light curve and $J-H$ color curve as a function of the phase of the 227-day period are presented in Fig. 7; the object reddens in the transition from maximum to minimum J brightness. The significant variations of the J brightness and $J-H$ color index indicate that the period found probably corresponds to the characteristic life time of dust clouds in the spherically symmetrical dust envelope of FG Sge in 1992−2001.

5. CONCLUSIONS

We can thus draw the following main conclusion from our analysis of 1985−2001 $JHKLM$ photometry of FG Sge: the IR variability of FG Sge after August 1992 can be explained by the emission from the spherically symmetrical dust envelope and the quasi-regular appearance of dust clouds in the line of sight, which can condense and disperse in the dust envelope.

The mean 0.36−5 μm SED at the J maxima can be reproduced with a sum of the radiation from a G0 supergiant attenuated by a spherically symmetrical dust envelope with mean optical depth 0.65 ± 0.15 and the emission of the dust envelope itself, with the temperature of its graphite grains being 750 ± 150 K. During the J minima, only emission from the dust envelope is observed at 1.65−5 μm. The dust cloud's optical depth at $\lambda = 1.25$ μm was ~ 4.3 during the 2001 J-brightness minimum, much higher than the optical depth of the dust envelope of FG Sge. The mean integrated flux from the dust envelope in 1992−2001 was $\sim (1.0 \pm 0.2) \times 10^{-8}$ erg s^{-1} cm^{-2}, and the integrated flux from the dust envelope varied by approximately a factor of 1.5−2 in 1992−2001. In the J minima, the integrated flux is nearly half that in the J maxima.

The variations of τ_{mean} for the spherically symmetrical dust envelope in 1992−2001 were in the range 0.5−1.0. The maximum density of the envelope was

recorded in the second half of 1993. Several episodes of partial dissipation and replenishing of the envelope with dusty material were observed in 1992−2001.

The mean mass of the dust envelope of FG Sge in 1992−2001 was $(3 \pm 1) \times 10^{-7} M_\odot$. Variations in the envelope mass were in the range $(2-4) \times 10^{-7} M_\odot$.

The bulk of the spherically symmetrical dust envelope was formed in Autumn 1992 on a time scale shorter than 500 days, and the rate of mass loss by the supergiant during the initial period exceeded $2 \times 10^{-7} M_\odot$/yr. Later, the rate of injection of matter into the spherically symmetrical dust envelope and rate of dissipation of the dust envelope remained nearly equal and were about half the rates during the initial period. By 1999, the injection and dissipation began to slow, and the spherically symmetrical dust envelope was relatively stationary from 1999 until the middle of 2001. Thus, the initial ejection of matter by the supergiant in Autumn 1992 and the supergiant's variable stellar wind supported the dust envelope at least until October 2001, when our observations ended.

The supergiant's spectral type based on the $J-H$ color index in 1992−2001 is K3 I. During this period, its radius increased by almost a factor of 1.6 compared to its radius in 1989. Like the formation of the spherically symmetrical dust envelope, the supergiant's cooling and expansion in Autumn 1992 occurred within several hundred days, and these processes were probably synchronous.

We have improved the 1989 parameters of FG Sge derived previously. The 0.36−5-μm radiation of FG Sge could be represented with the spectrum of a normal G(0 ± 1) supergiant. In 1989, the mean integrated flux from FG Sge was F_{int}(FG Sge) = $(2.1 \pm 0.1) \times 10^{-8}$ erg s^{-1} cm^{-2}; for a distance to FG Sge of $r = 3.1 \pm 0.1$ kpc, the corresponding radius was $R^* = (5.4 \pm 0.5) \times 10^{12}$ cm. The optical depth of the dust envelope at 5 μm was about 2.5×10^{-3}.

ACKNOWLEDGMENTS

REFERENCES

1. O. G. Taranova, Astrofizika **25**, 453 (1986).
2. V. P. Arkhipova and O. G. Taranova, Pis'ma Astron. Zh. **16**, 808 (1990) [Sov. Astron. Lett. **16**, 347 (1990)].
3. B. Montesinos, A. Cassatella, R. Gonzalez-Reistra, *et al.*, Astrophys. J. **363**, 245 (1990).
4. C. E. Woodward, G. F. Lawrence, R. D. Gehrz, *et al.*, Astrophys. J. Lett. **408**, L37 (1993).
5. G. Gonzalez, D. L. Lambert, G. Wallerstein, *et al.*, Astrophys. J., Suppl. Ser. **114**, 133 (1998).
6. V. P. Arkhipova, V. F. Esipov, G. V. Sokol, and S. Yu. Shugarov, Pis'ma Astron. Zh. **25**, 849 (1999) [Astron. Lett. **25**, 739 (1999)].
7. A. M. Tatarnikov, V. I. Shenavrin, and B. F. Yudin, Astron. Zh. **75**, 428 (1998) [Astron. Rep. **42**, 377 (1998)].
8. A. M. Tatarnikov and B. F. Yudin, Pis'ma Astron. Zh. **24**, 359 (1998) [Astron. Lett. **24**, 303 (1998)].
9. O. G. Tapanova, Pis'ma Astron. Zh. **13**, 891 (1987) [Sov. Astron. Lett. **13**, 374 (1987)].
10. C. W. Allen, *Astrophysical Quantities* (Athlone Press, London, 1973; Mir, Moscow, 1977).
11. P. M. Williams and A. J. Longmore, Mon. Not. R. Astron. Soc. **207**, 139 (1984).

Translated by N. Samus'

Structure of Gas Flows in Z And in Quiescence and during Outbursts

D. V. Bisikalo[1], A. A. Boyarchuk[1], E. Yu. Kilpio[1], and O. A. Kuznetsov[1, 2]

[1]*Institute of Astronomy, Russian Academy of Sciences, Pyatnitskaya ul. 48, Moscow, 109017 Russia*

[2]*Keldysh Institute of Applied Mathematics, Russian Academy of Sciences, Miusskaya pl. 4,
Moscow, 125047 Russia*

Received March 15, 2002

Abstract—A new mechanism is proposed to account for transitions between the quiescent and active states of symbiotic stars. A numerical study of the gas dynamics of the flows in the symbiotic star Z And shows that even small variations in the velocity of the wind from the cool giant can abruptly change the flow structure near the hot component. Such changes alter the accretion regime as the wind velocity increases: disk accretion makes a transition to accretion from the flow. Our calculations indicate that the accretion rate increases by a factor of several tens over a short time interval (~ 0.1 of the orbital period) during the rearrangement of the flow, when the accretion disk is destroyed. © *2002 MAIK "Nauka/Interperiodica".*

1. INTRODUCTION

Symbiotic stars are stars with peculiar spectra simultaneously containing molecular absorption bands typical of cool giants and high-excitation emission lines. The spectra of symbiotic stars are typical of those of cool giants in the red and IR but are characterized by a hotter continuum in the UV. Moreover, the spectra of such stars include a multitude of atomic emission lines corresponding to very different degrees of ionization. In addition to their peculiar spectra, symbiotic stars are characterized by considerable photometric and spectrometric variability.

We consider here the classic S-type symbiotic star Z And, which is among the best studied symbiotics. It has been systematically observed in the visual for more than 100 years. The light curve of this star is characterized by long stages of flare activity lasting up to several years, during which the brightness-variation amplitude in the visual can reach 3^m (from 11^m to 8^m), and quiescent periods lasting tens of years, when the star's brightness is nearly minimum.

Spectral observations of Z And were first made in 1928, when Plaskett [1] measured its optical spectrum. Since the photometric study of Z And by Boyarchuk in 1967 [2, 3], it has been commonly recognized that Z And is a binary system comprising a cool giant and a hot dwarf surrounded by a nebula. Since the beginning of IUE observations in 1978, Z And has been intensely and systematically observed in the UV. The IUE data archive includes 245 observations of Z And in 1978–1995. The available observations cover both the quiescent and active states of the system; the latter occured in 1984 and lasted about 900 days.

Studies of the spectral energy distribution of Z And over a wide range (from ultraviolet to infrared) during a quiescent period (1978–1982) [4] confirmed the binarity of Z And. According to these data, the characteristics of the components are as follows. The cool giant has a spectral class of M3.5III and loses matter at a rate of 2×10^{-7} $M_\odot$/yr; the compact hot component with a temperature of $\sim 10^5$ K accretes a small fraction (about 2%) of the wind from the donor. The gas of the intercomponent envelope has an electron density of $\sim 2 \times 10^{10}$ cm^{-3} and a temperature of $\sim (1.5–8) \times 10^4$ K. The components of Z And do not fill their Roche lobes, and matter exchange must occur via the stellar wind in this system.

Systematic observations of Z And have yielded the parameters of the system during flares. In 1995, Fernandez-Castro *et al.* [5] compiled observational results for Z And during the flares of 1984 and 1985 and noted the following typical features:

(1) a substantial decrease in the degree of ionization;

(2) a change in the slope of the UV continuum, which corresponds to a markedly lower temperature during the optical maximum;

(3) an increase in the optical depth of the medium, manifest, in particular, in a reduced flux ratio between the components of the CIV 1550 Å doublet;

(4) the appearance of P-Cygni emission-line profiles;

(5) an overall broadening of emission lines in the UV (e.g., the width of the CIII 1910 Å line increased by factors of 2.5 and 3 during the first and the second

flare, respectively), providing evidence for an increase in the speed of the emitting material.

These observational features can be explained if an optically thick envelope was formed and subsequently ejected by the accretor at a speed of 250−300 km/s during the flares in April 1984 and December 1985.

A number of mechanisms have been suggested to explain nova-like flare activity in symbiotic stars (see, e.g., [6] for a review). The most plausible scenario for Z And proposes the release of energy due to fluctuations in the accretion rate relative to the level corresponding to a steady-state combustion regime [5]. What is responsible for these variations in the accretion rate? Some studies [7, 8] have suggested that the flare activity is determined by variability of the wind from the giant; however, observations during the preflare period have revealed only small changes in the wind properties [7, 9]. This imposes strict constraints on all evolutionary scenarios that attribute the development of flare activity to changes in the properties of the giant. We consider here a new mechanism that gives rise to changes in the accretion rate in symbiotic systems and, consequently, can explain the observed transitions between quiescent and active states as an effect of the variations in the parameters of the wind issuing from the giant. The numerical simulations presented here indicate that even a small increase in the velocity of the giant wind that does not exceed the recorded variations in the wind can modify the accretion regime, forcing a transition from disk accretion to accretion from the flow. During the restructuring of the flow, the accretion rate increases substantially, possibly altering the combustion regime in the outer layers of the accretor. If the accretion rate exceeds the maximum rate at which hydrogen can burn in a shell around the degenerate core, the accreted material accumulates over the burning shell, and the accretor expands to sizes typical of giants [10−16]. Although the bolometric luminosity remains constant in this case, the visible brightness increases by $1-2^m$, while the effective temperature decreases. An optical flare develops on the thermal time scale [6, 12]. This mechanism is commonly associated with flares of classic symbiotic stars, such as Z And. To summarize, the considered increase in the accretion rate, which is accompanied by changes in the combustion regime, can result in the ejection of material from the accretor, i.e., in the appearance of the flow features needed to explain the observations.

2. THE MODEL

We studied the structure of matter flows in the equatorial plane of the symbiotic system Z And using
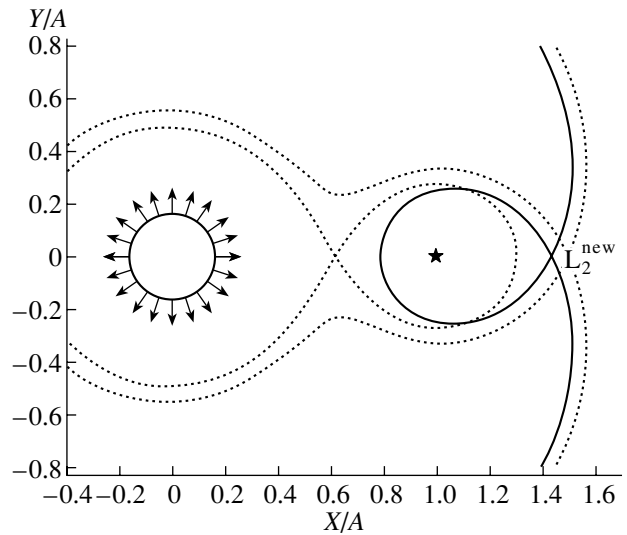
Fig. 1. Contours of the standard Roche potential passing through the stationary points L_1 and L_2 (dashed) and a contour of the modified potential passing through the stationary point L_2^{new} (solid). The bold circle marks the donor star, the star the accretor, and the arrows, the stellar wind of the donor.

a two-dimensional gas-dynamical model. The coordinate origin was at the center of the primary component (donor), with the x axis directed along the line connecting the component centers and the y axis aligned with the direction of the orbital motion of the

Parameters of the Z And system

Parameter	Value
Mass of the primary (cold) component M_1	$2M_\odot$
Radius of the primary (cold) component R_1	$77R_\odot$
Mass of the accretor M_2	$0.6M_\odot$
Radius of the accretor R_2	$0.07R_\odot$
Orbital period of the system P_{orb}	760 days
Distance between the components A	$483R_\odot$
Radius of the donor Roche lobe	$232R_\odot$
Orbital speed of the donor	7 km/s
Orbital speed of the accretor	25 km/s

accretor. The flow was described by a system of Euler equations for a rotating coordinate frame:

$$\frac{\partial \rho}{\partial t} + \frac{\partial \rho u}{\partial x} + \frac{\partial \rho v}{\partial y} = 0,$$

$$\frac{\partial \rho u}{\partial t} + \frac{\partial (\rho u^2 + P)}{\partial x} + \frac{\partial \rho uv}{\partial y} = -\rho \frac{\partial \Phi}{\partial x} + 2\Omega v \rho,$$

$$\frac{\partial \rho v}{\partial t} + \frac{\partial \rho uv}{\partial x} + \frac{\partial (\rho v^2 + P)}{\partial y} = -\rho \frac{\partial \Phi}{\partial y} - 2\Omega u \rho,$$

$$\frac{\partial \rho E}{\partial t} + \frac{\partial \rho uh}{\partial x} + \frac{\partial \rho vh}{\partial y} = -\rho u \frac{\partial \Phi}{\partial x} - \rho v \frac{\partial \Phi}{\partial y}.$$

Here, $\mathbf{u} = (u, v)$ is the velocity vector, P is the pressure, ρ is the density, $h = \varepsilon + P/\rho + |\mathbf{u}|^2/2$ is the specific total enthalpy, $E = \varepsilon + |\mathbf{u}|^2/2$ is the specific total energy, ε is the specific internal energy, Ω is the angular velocity of the system, and $\Phi(\mathbf{r})$ is the force potential.

In a standard formulation of the problem taking into account only the gravitational forces produced by the components of the system and the centrifugal force, the potential has the form

$$\Phi(\mathbf{r}) = -\frac{GM_1}{|\mathbf{r} - \mathbf{r}_1|} - \frac{GM_2}{|\mathbf{r} - \mathbf{r}_2|} - 1/2\Omega^2(\mathbf{r} - \mathbf{r}_c)^2.$$

Here, M_1 is the mass of the donor, M_2 is the mass of the accretor, $\mathbf{r}_1$ and $\mathbf{r}_2$ are the position vectors of the stellar centers, and $\mathbf{r}_c$ is the position vector of the center of mass of the binary. This is the so-called Roche potential; in our case, however, we must include the additional force that accelerates the wind from the donor, which will modify the form of the potential.

Previous studies (see, e.g., [17−19]) have demonstrated that the overall flow structure in a system whose components do not fill their Roche lobes is determined primarily by the adopted stellar-wind parameters. Unfortunately, there is no commonly accepted mechanism for the acceleration of gas in stellar atmospheres. For this reason, we do not consider real acceleration mechanisms and instead use the following parametric equation for the gas-accelerating force:

$$\mathbf{F}(\mathbf{r}) = \alpha \frac{GM_1}{|\mathbf{r}|^2} \frac{\mathbf{r}}{|\mathbf{r}|},$$

where α is a parameter.

This force, which is directed away from the primary, modifies the potential in the following way:

$$\Phi(\mathbf{r}) = -\frac{GM_1}{|\mathbf{r} - \mathbf{r}_1|} + \alpha \frac{GM_1}{|\mathbf{r} - \mathbf{r}_1|} - \frac{GM_2}{|\mathbf{r} - \mathbf{r}_2|}$$
$$- 1/2\Omega^2(\mathbf{r} - \mathbf{r}_c)^2.$$

The structure of the standard and modified (for $\alpha = 1$) potential is shown in Fig. 1. We can see that

the Roche lobe of the donor vanishes at $\alpha = 1$, while the Roche lobe of the accretor changes its shape only slightly.

Numerical simulations carried out for various α values [20] indicated that no steady-state solution exists for $\alpha < 0.8$. In this case, the gas that was injected into the space between the components at an early stage falls back to the donor surface. Here, as in [21, 22], we assume that $\alpha = 1$; i.e., the gravitational force of the donor is completely balanced by the gas-accelerating force. The accepted value of α provides for a wind characterized by a boundary velocity of 25 km/s, the value at infinity $V^\infty \simeq 32$ km/s, and the velocity variation according to the beta (Lamers) law with $\beta \approx 1$.

We closed the system using the equation of state for an ideal gas,

$$P = (\gamma - 1)\rho\varepsilon$$

with the adiabatic index γ taken to be 5/3. The solution for $\gamma = 5/3$ corresponds to the case of no energy losses, and yields correct results only for systems with negligible radiative losses, i.e., for optically thick media. The intensity ratio observed in the CIV 1550 Å doublet suggests that the intercomponent envelope of Z And is optically thin in the quiescent state [5]. However, we are not concerned with the entire extended envelope but rather with the vicinity of the accretor in the equatorial plane of the system, i.e., with the disk. Estimates show that a disk with a temperature of $T = 15\,000$ K will be optically thick for the accretion rate $\dot{M}_{\mathrm{accr}} = 4.5 \times 10^{-9} M_\odot$/yr observed for Z And, justifying the use of the adiabatic model in the flow region of interest. Indeed, the optical depth is defined as the product of the absorption coefficient κ, the density, and the layer thickness, $\tau = \kappa\rho l$. For disk accretion, the main parameter is the ratio of the thickness of the $\tau = 1$ layer to the disk thickness. For disk accretion,

$$\dot{M}_{\mathrm{accr}} = 2\pi RH\rho v_r.$$

Here, R is the disk radius, H is the disk half-thickness, and v_r is the radial velocity component

$$v_r = \frac{\alpha_{SS}c_s H}{R},$$

where c_s is the sound speed, α_{SS} is the Shakura−Sunyayev parameter, and

$$H = \frac{c_s}{V_{\mathrm{K}}}R,$$

with V_{K} being the Keplerian velocity. Therefore, we obtain

$$\frac{l^{\tau=1}}{H} = \frac{2\pi\alpha_{SS}}{\kappa\dot{M}_{\mathrm{accr}}}\frac{c_s^2 R}{V_K} = \frac{2\pi\alpha_{SS}}{\kappa\dot{M}_{\mathrm{accr}}}\frac{\mathcal{R}TR^{3/2}}{\sqrt{GM}}.$$

For characteristic disk temperatures $T \simeq 15\,000$ K, the absorption coefficient depends only weakly on the density, and is equal to $\simeq 100$ cm^2/g [23]. Assuming $T = 15\,000$ K, $R = 50R_\odot = A/10$, and $M = 0.6M_\odot$ (in this case, $c_s = 11$ km/s, $V_K = 49$ km/s, $H = 11R_\odot$), we obtain

$$\frac{l^{\tau=1}}{H} = 8 \times 10^{-3} \left(\frac{\alpha_{SS}}{0.1}\right) \left(\frac{\kappa}{100 \text{ cm}^2/\text{yr}}\right)^{-1}$$
$$\times \left(\frac{\dot{M}_{\text{accr}}}{10^{-8}M_\odot/\text{yr}}\right)^{-1};$$

i.e., for $\dot{M}_{\text{accr}} = 4.5 \times 10^{-9}M_\odot$/yr, the optical depth $\tau = 1$ corresponds to less than 2% of the disk thickness.

The parameters of Z And were taken from [4] and are listed in the table.

The above system of two-dimensional gas-dynamical equations was solved using the Roe scheme [24] with flux limits in the form given by Osher [25]. This scheme is quasi-monotonic and has third-order accuracy in space and first-order accuracy in time. In our computations, we used a spatially uniform finite-difference grid of 301×301 grid points on the square $[-A \ldots 2A] \times [-3/2A \ldots 3/2A]$ with circles whose radii equal the radii of the system components centered on the system components cut out. The condition of free outflow of matter was adopted at the boundary of the computation domain. The boundary conditions at the surface of the compact object were specified in the form $\mathbf{u} = 0$, $P = 0$, which corresponds to the case of complete accretion of all material that arrives at this component. The boundary value of the density at the donor surface does not affect the solution, since the system of equations considered admits scaling in ρ (with simultaneous scaling in P). The boundary conditions at the donor surface were a density of $\rho = 1$, a temperature of $T = 3200$ K, and the injection of gas into the system normal to the surface at a wind velocity V. We carried out simulations for wind speeds V ranging from 25 to 75 km/s.

The initial conditions within the computation domain corresponded to a low-density motionless gas, which was subsequently ejected from the system by the gas outflowing from the primary. The system of equations was solved using the steady-state method, starting from the arbitrarily chosen initial conditions $\rho_0 = 10^{-5}\rho(R_1)$, $P_0 = 10^{-4}\rho(R_1)c^2(R_1)/\gamma$, $\mathbf{u}_0 = 0$ ($\rho(R_1)$ and $c(R_1)$ refer to the donor surface) and continuing until the solution reached a steady-state regime.

3. RESULTS

We ran a number of simulations for various stellar-wind speeds.

At a wind velocity of $V = 25$ km/s, an accretion disk forms in a system with a steady-state matter flow. We believe that the steady-state regime is established when the matter flow into the computation domain becomes equal to the outflow from this domain (some material is accreted, and the rest escapes through the outer boundary). Beginning with that time, the amount of matter in the system no longer changes, and the accretion rate settles down to a constant value. Our calculations show that the accretion rate stops changing approximately four orbital periods after the beginning of the computation run and makes up $\sim 1\%$ of the matter flow from the donor surface.

Figures 2 and 3 illustrate the morphology of the flow for $V = 25$ km/s 11 orbital periods after the beginning of the run. Distances are given in solar radii. The left panel in Fig. 2 shows the density field and velocity vectors (shown by arrows) in the computation subdomain $[0 \ldots 1.6A] \times [-0.8A \ldots 0.8A]$. The donor surface is indicated by a semicircle of radius R_1 centered on $(0, 0)$. The dashed lines are equipotentials of the standard Roche potential. The star marks the accretor.

The flow structure in binaries with components that do not fill their Roche lobes is determined by the direct flow of matter onto the compact object and by the stream due to the orbital motion of the accretor in the stellar-wind gas. The interaction of these two flows produces a pattern with two detached shock waves (see the left panel in Fig. 2, where the shocks are visible as regions of crowding of the density contours).

An expanded view of the neighborhood of the accretor is given in the left panel of Fig. 2. The domain shown is $[0.8A \ldots 1.2A] \times [-0.2A \ldots 0.2A]$, or 40×40 grid cells. The detached shock wave is separated from the accretor by a distance of about $40R_\odot$. Moreover, a spiral shock can be seen but can be described in detail only on denser grids than the one used. Analysis of the velocity vectors and density contours plotted in the figure suggests that a disk is present around the accreting component.

The presence of an accretion disk is confirmed by Fig. 3. Curves *1* and *2* are streamlines. The material moving along curve *1* flows around the accretor and leaves its neighborhood, while the material whose trajectory is curve *2* (winding around the accretor) reaches the accretor. Curve *2* is the limiting form of the path along which the material arrives at the accretor; in other words, all gas particles whose trajectories pass at larger distances from the accretor flow around it (e.g., along curve *1*). Assuming that
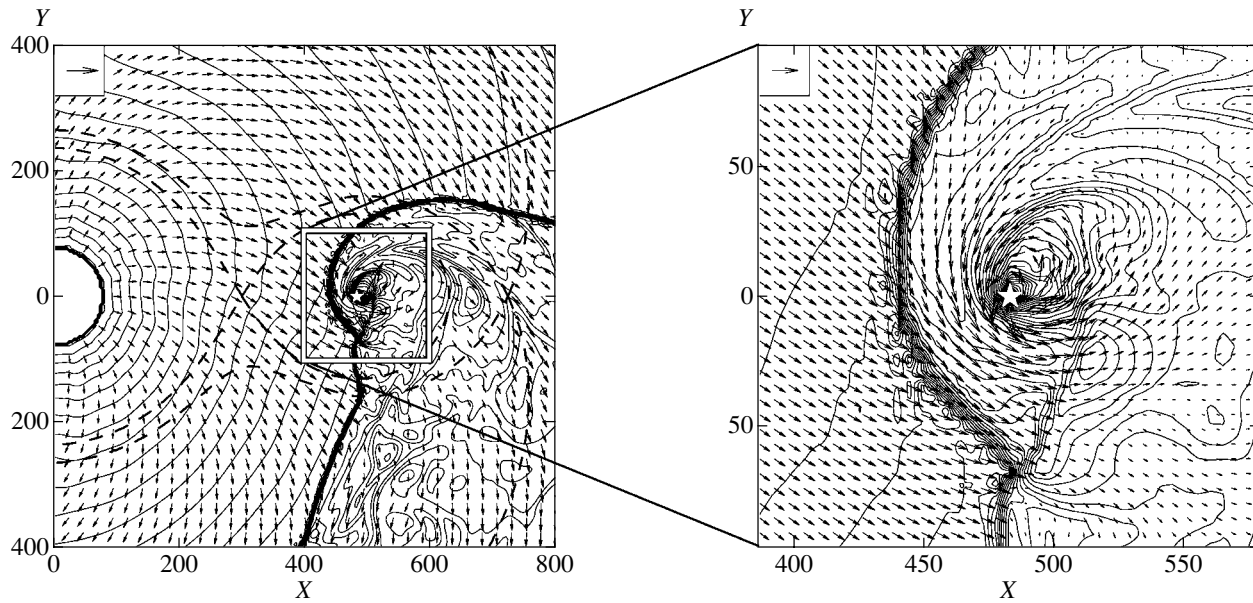
Fig. 2. Left: density field and velocity vectors for the steady state at $V = 25$ km/s 11 orbital periods after the beginning of the run. The contours of the density logarithm are shown with a constant increment and a range from 10^{-5} to 1 (in units of the density at the donor surface). Distances are given in solar radii. The arrow in the upper left corner corresponds to 100 km/s. The dashed lines are equipotentials of the standard Roche potential, and the accretor is marked with a star. The square delimits the subregion shown in the right panel of this figure and in Fig. 3. Right: expanded view of the neighborhood of the accretor. The density contours range from 10^{-2} to 1 (in units of the density at the donor surface).
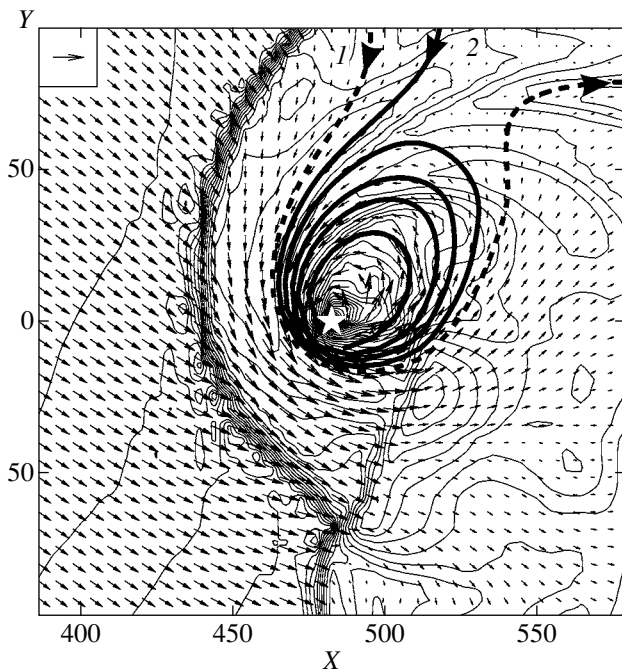

Fig. 3. Same as the right panel in Fig. 2, with two streamlines (heavy curves): the dashed curve (*1*) represents the streamline flowing around the accretor, while the solid curve (*2*) shows the trajectory of the material falling onto the accretor.

curve *2* corresponds to the edge of an accretion disk, we obtain the estimate $a \sim 0.1A$ for the semimajor axis of the disk and $e \sim 0.65$ for its eccentricity.

In runs with higher donor-wind speeds, the shock is closer to the accreting component, and becomes attached to it at sufficiently high speeds. Figure 4 shows the morphology of the flow for $V = 75$ km/s 9.5 orbital periods after the start of the run, when a steady-state regime has already been established in the system. As in Fig. 2, the density fields and velocity vectors are plotted. The sizes of the regions depicted in Fig. 4 and the notation are the same as in Fig. 2. In stark contrast to the case of the limiting wind velocity $V = 25$ km/s (Fig. 2), a conical wave is observed instead of a detached shock, and no accretion disk is present. We can see in the right panel of Fig. 4, which shows an expanded view of the vicinity of the accretor, that the shock contacts the accreting component within the spatial resolution chosen for our computations. This inhibits the formation of a disk, and accretion from the flow takes place instead of disk accretion. The accretion rate is much higher in this case, $\sim 2\%$ of the rate of mass loss from the donor surface.

These examples demonstrate that two substantially different situations with different accretion regimes correspond to a small difference in the wind
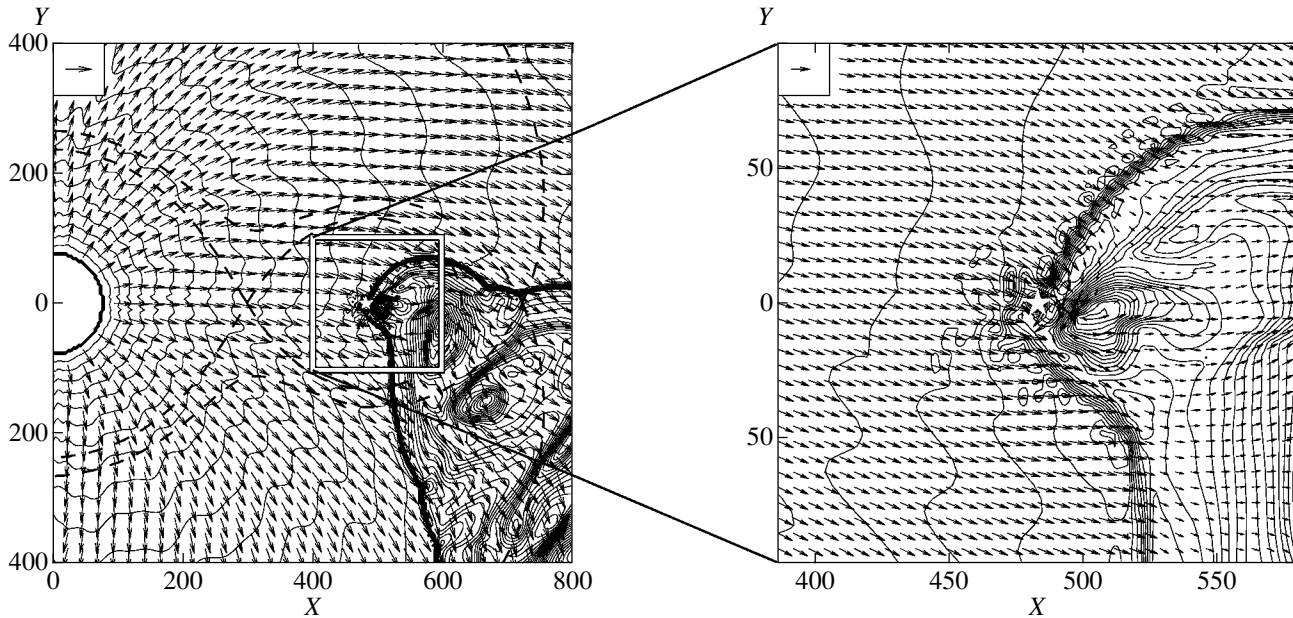
Fig. 4. Same as Fig. 2 for $V = 75$ km/s and 9.5 orbital periods after the beginning of the run. The density contours in the right panel correspond to values from 0.04 to 0.55 (in units of the density at the donor surface).

velocities. To determine the critical donor-wind velocity dividing the different accretion regimes, we ran a number of simulations for different wind speeds from 25 to 75 km/s. The results indicate that, for speeds of $V \lesssim 35$ km/s (~ 1.4 of the orbital speed of the accretor), a flow pattern with an accretion disk is established (Figs. 2, 3). At speeds $V \gtrsim 35$ km/s, a conical shock wave forms, and the resulting pattern is similar to that shown in Fig. 4.

To study the transition between these two regimes after an increase in the wind velocity, we took the steady-state solution for $V = 25$ km/s and a time of 11 orbital periods after the beginning of the run (the situation represented by Figs. 2, 3), raised the donor wind velocity to V_1, and continued the computations. Various cases with V_1 in the range 35 km/s $\leq V_1 \leq$ 75 km/s were studied. Obviously, the flow structure will change with the increase in the boundary wind velocity, and a transition will occur from the state shown in Fig. 2 to a new steady-state solution similar to that represented by the left panel in Fig. 4. The two most important times of the flow restructuring are illustrated in Fig. 5 for $V_1 = 75$ km/s. The domain size and the notation are analogous to those in the right panel in Fig. 2. Within $0.06 P_{\rm orb}$ (~ 45 days) after the change in the wind speed, the matter moving at the increased speed reaches the neighborhood of the accreting component; that is, it reaches the detached shock located in front of this component. This is illustrated in Fig. 5a, which corresponds to the time

of the interaction between the freshly incoming material and the shock. Afterwards, the wind advances further, "wrinkling" the disk and forcing its material to fall onto the accretor. As a result, the accretion rate jumps by a factor of several tens, reaching a maximum when the disk disappears, $0.08 P_{\rm orb}$ (~ 60 days) after the change in the wind parameters. Figure 5b corresponds to the time when the disk has been disrupted and the accretion rate has become maximum.
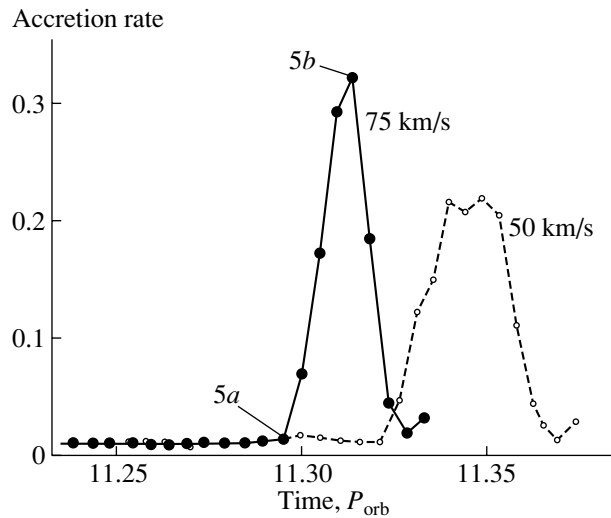
The time variation of the accretion rate after the change in the donor-wind velocity is shown in Fig. 6. The horizontal axis plots the time since the beginning of the run (in orbital periods). The vertical axis plots the accretion rate in fractions of the rate of mass loss from the donor surface. Two cases are shown. In the first, the donor-wind velocity was raised to $V_1 = 75$ km/s in the steady-state solution with $V = 25$ km/s; in the second, it was raised to $V_1 = 50$ km/s. The points corresponding to the times for which Figs. 5a and 5b are plotted are marked on the graph of the accretion rate as a function of time for $V_1 = 75$ km/s (bold curve). When the wind material moving at the increased speed reaches the shock surrounding the accretor, a transition regime ensues. The accretion rate increases dramatically and reaches a maximum ($\sim 30\%$) within ~ 15 days, followed by a rapid decline. If the boundary value of the wind velocity is raised to 50 km/s, the matter reaches the accretor somewhat later (within $\sim 0.09 P_{\rm orb}$), and the flow is restructured somewhat more slowly. Although the accretion rate in this case does not attain values
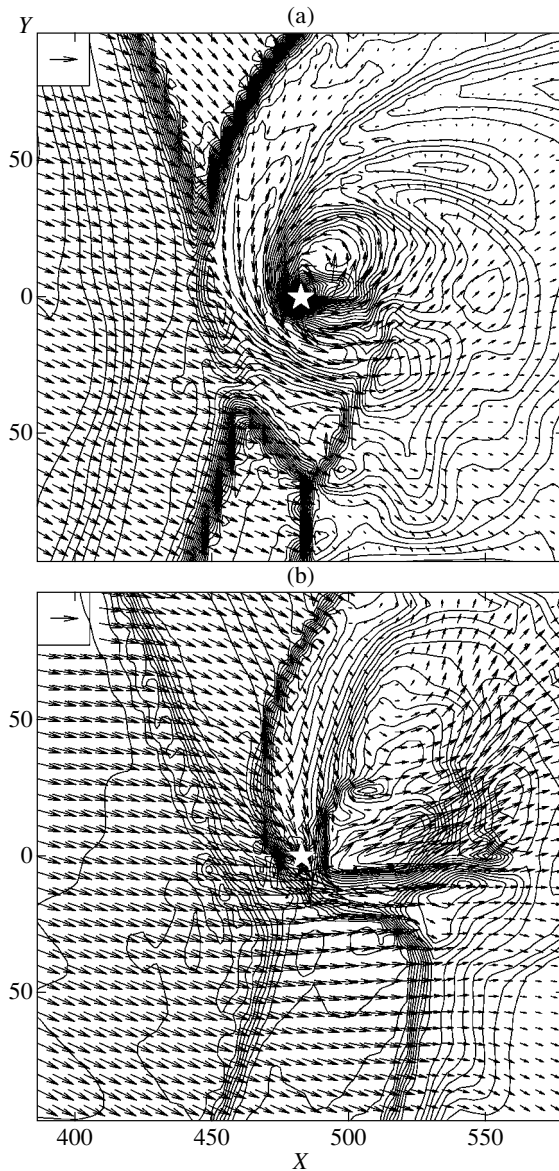
Fig. 5. Density field and velocity vectors around the accretor during the flow rearrangement when period the accretion disk is destroyed. (a) Time when the material moving with increased speed approaches the shock surrounding the accretor and disk ($0.06P_{\mathrm{orb}}$ after the increase in the wind velocity). (b) Time when the disk vanishes and the maximum accretion rate is observed ($0.08P_{\mathrm{orb}}$ after the increase in the wind velocity). Contours of the logarithm of the density (in units of the donor surface density) are plotted with a constant increment and range from (a) 0.015 to 1.21 and (b) 0.1 to 3.29. Distances are given in solar radii. The arrow at the upper left corner corresponds to a velocity of 100 km/s.

Fig. 6. Time variation of the accretion rate after the increase in the wind velocity from $V = 25$ km/s to $V_1 = 75$ km/s (bold curve with filled circles) and from $V = 25$ km/s to $V_1 = 50$ km/s (dashed curve with open circles). Time is measured in orbital periods. The time of the increase in the wind speed corresponds to 11.2 orbital periods after the beginning of the run. The accretion rate is measured in fractions of the donor mass-loss rate. In the graph for $V_1 = 75$ km/s, the marked points correspond to the times for which Figs. 5a and 5b are plotted.

as high as for $V_1 = 75$ km/s, it exceeds the quiescent-state value by more than a factor of 20.

Analysis of the data presented in Fig. 6 indicates that, during the transition period, the integral $\int \dot{M}_{\mathrm{accr}}dt$ yields nearly the same values for the different cases (0.0051 and 0.0061 for $V_1 = 75$ km/s and $V_1 = 50$ km/s, respectively), suggesting that nearly the same amount of material is accreted in both cases. This seems quite natural if we assume that the disk material is completely accreted. The slightly increased amount of material accreted when $V_1 = 50$ km/s can likely be accounted for by the fact that, at the larger speed of $V_1 = 75$ km/s, the disk material is partly swept out of the system and does not have enough time to be accreted.

We note that studies of the transition regime based on our model have limited value. After the sharp increase in the accretion rate, the adopted boundary conditions at the accretor fail, and our model no longer reflects the actual physical situation. Accordingly, the simulations of the transition regimes presented here are only valid at early stages of the process. For this reason, we have restricted our consideration to qualitative features of the proposed mechanism. A detailed quantitative analysis of the flow restructuring and of the related increase in the accretion rate requires that substantial enhancements be added to the model.

According to available estimates [5], the speed of the donor wind in Z And is 25–40 km/s for the quiescent state of the system. These speeds are close

to the critical value (35 km/s) separating the two accretion regimes. If weak fluctuations are present in the wind velocity (due, for example, to the activity of the giant [6]), the wind velocity could exceed the critical value. As a result, the flow structure and accretion regime will change, and the accretion rate will grow substantially during the transition period.

4. CONCLUSION

Based on our numerical simulations of the flow structure in Z And, we propose here a new mechanism for variations in the rate of accretion onto the compact component of the system that can explain the nova-like activity of symbiotic stars. The essence of the mechanism is a sharp alteration of the flow pattern near the hot component of the system as the result of small changes in the speed of the wind from the cool giant. These changes are manifest as a transition from disk accretion to accretion from the flow as the wind velocity increases.

Our two-dimensional numerical simulations of the gas dynamics of matter flows in Z And demonstrate that, under quiescent conditions with donor-wind speeds from 25 to 40 km/s, a stable accretion disk forms in the system. In this flow regime, the accretion efficiency is $\sim 1\%$ of the rate of mass loss by the donor star. As the wind velocity is increased above 35 km/s, the disk disappears, and a conical shock wave forms. The steady-state solutions for high-speed (35−75 km/s) regimes exhibit a slightly higher efficiency, $\sim 2\%$ of the donor mass-loss rate. During the flow rearrangement, however, when the wind with an increased velocity reaches the disk and wrinkles it, the accretion rate increases by a factor of several tens.

Analyses of observations of symbiotic stars in their active states show that most observed manifestations of their activity can be explained by the hypothesis that the accretor ejects an optically thick envelope [5]. The mechanism suggested here provides an increase in the accretion rate and a corresponding growth in the rate of energy release sufficient to eject some fraction of material from the accretor, endowing the flow with the features needed to explain the observations.

ACKNOWLEDGMENTS

REFERENCES

1. H. H. Plaskett, Publ. Dominion Astrophys Obs. **4**, 119 (1928).
2. A. A. Boyarchuk, Izv. CRAO **38**, 155 (1967).
3. A. A. Boyarchuk, Astron. Zh. **44**, 1016 (1967) [Sov. Astron. **11**, 818 (1967)].
4. T. Fernandez-Castro, A. Cassatella, A. Gimenez, *et al.*, Astrophys. J. **324**, 1016 (1988).
5. T. Fernandez-Castro, R. Gonzales-Riestra, A. Cassatella, *et al.*, Astrophys. J. **442**, 366 (1995).
6. J. Mikołajewska and S. J. Kenyon, Mon. Not. R. Astron. Soc. **256**, 177 (1992).
7. M. Friedjung, in *Cataclysmic Variables and Related Objects*, Ed. by M. Hack and C. La Douse (US Gov. Printing Office, Washington, 1993), p. 647.
8. A. A. Boyarchuk, in *Variable Stars and Galaxies*, ASP Conference Series, 1992, Vol. 30, p. 325.
9. S. J. Kenyon and J. S. Gallagher, Astron. J. **88**, 666 (1983).
10. A. V. Tutukov and L. R. Yungelson, Astrofizika **12**, 521 (1976).
11. B. Paczyński and A. Żytkow, Astrophys. J. **222**, 604 (1978).
12. B. Paczyński and B. Rudak, Astron. Astrophys. **82**, 349 (1980).
13. E. M. Sion, M. J. Acierno, and S. Tomczyk, Astrophys. J. **230**, 832 (1979).
14. I. Iben, Jr., Astrophys. J. **259**, 244 (1982).
15. M. Y. Fujimoto, Astrophys. J. **257**, 767 (1982).
16. I. Iben, Jr. and A. V. Tutukov, Astrophys. J. **342**, 430 (1989).
17. G. S. Bisnovatĭ-Kogan, Ya. M. Kazhdan, A. A. Klypin, *et al.*, Astron. Zh. **56**, 359 (1979) [Sov. Astron. **23**, 201 (1979)].
18. D. V. Bisikalo, A. A. Boyarchuk, O. A. Kuznetsov, *et al.*, Astron. Zh. **71**, 560 (1994) [Astron. Rep. **38**, 494 (1994)].
19. D. V. Bisikalo, A. A. Boyarchuk, O. A. Kuznetsov, *et al.*, Astron. Zh. **73**, 727 (1996) [Astron. Rep. **40**, 662 (1996)].
20. E. Kilpio, Odessa Astron. Publ. **14**, 41 (2001).
21. T. Theuns and A. Jorissen, Mon. Not. R. Astron. Soc. **265**, 946 (1993).
22. T. Theuns, H. M. J. Boffin, and A. Jorissen, Mon. Not. R. Astron. Soc. **280**, 1264 (1996).
23. K. R. Bell and D. N. Lin, Astrophys. J. **427**, 987 (1994).
24. P. L. Roe, Ann. Rev. Fluid Mech. **18**, 37 (1986).
25. S. Chakravarthy and S. Osher, AIAA Pap N 85−0363 (1985).

Translated by A. Getling

A Double-Head Photon-Counting Photometer for Fast Timing Observations

A. Piccioni[1], F. Giovanelli[2], K. Bartolini[1], I. Bruni[1], M. Frutti[1], and A. Guarnieri[1]

[1]*Dipartimento di Astronomia, Università di Bologna, Via Ranzani 1, Bologna, I 40127 Italy*

[2]*Istituto di Astrofisica Spaziale, CNR, Area di Ricerca di Roma Tor Vergata, Via del Fosso del Cavaliere 100, Roma, I 00133 Italy*

Received November 19, 2001; in final form, December 27, 2001

Abstract—The structure of the electronics of the two-head, high-speed photometer operating on the 152-cm G.D. Cassini telescope of Bologna University has been fully redesigned for high-time-resolution observations of fast variable sources, in particular, of the optical counterparts of X-ray binary systems. The fast photometer now permits sampling times from 0.1 ms to 100 s. The handling of the system clock and I/O configuration have been modified to provide rigorous synchronization of the sampling time with an external high-stability clock and the continuous acquisition of an uninterrupted data stream. The continuous data-acquisition process, which is driven by an external clock, is limited only by the capacity of the hard disk and is supported by a double-buffer SRAM memory designed to overcome any discontinuity in the asynchronous communication with the computer. Real-time monitoring of the data enables continuous evaluation of the weather conditions, and the directly displayed light curve can be used to determine the optimal management of the observations. © *2002 MAIK "Nauka/Interperiodica"*.

1. INTRODUCTION

High-accuracy, high-speed photometry is essential for observations of a great variety of objects: flare stars, cataclysmic variables, X-ray binaries, pulsars, pulsating degenerate stars, irregular variable stars (e.g., RS CVn, T Tauri, W Uma variables), pulsating nondegenerate stars, and extragalactic sources (e.g., BL Lac objects, quasars, active galactic nuclei).

Many phenomena observed in close binary systems occur on time scales from $\sim 10^{-3}$ to 10^7 s (e.g., [1]), depending on where the process is manifest. In particular, the following time scales are characteristic of the following processes:

—10^{-3}–10^2 s, typical of events occuring on or near the surfaces of collapsed objects (e.g., 0.5 ms for the SN 1987A pulsar [2], 33 ms for the Crab Pulsar [3], 7.5–10.7 s for the dwarf nova SS Cyg [4–6]), pulses from X-ray pulsars (see, e.g., [7]) and possibly related reprocessed oscillations in the optical, QPOs in low-mass binary systems (e.g., [8–10]) and in AM Her systems (e.g., the QPOs with period 1–3 s in E1405−451 [11]);

—10^{-1}–10^3 s, typical of phenomena occuring in accretion disks (e.g., the 1.24 s pulsation of the optically reflected X-ray beam in Her X1 [12], 32−36 s QPOs in SS Cyg [13], 71 s fluctuations associated with the disk-reprocessed beam in DQ Her [14] and in DQ Her stars in general [15]);

—10^0–10^2 s, characteristic of flickering in hot spots (e.g., in U Gem [16]) and inhomogeneities in accretion flows (e.g., in VV Pup [17]);

—10^4–10^5 s, typical of activity on the surface of a donor star (e.g., the 1−2 d optical transients in A0535+26, associated with episodes of mass ejection [18, 19]);

—10^4–10^7 s, typical of orbital periods (e.g., 6.6 h for SS Cyg [10, 21], 6.98 h for WX Ceti [22], 3.804 h for 4U/MXB1636 − 53 [23], 15.1 h for Cen X4 [24], 111 d for A0535+26 [25], 304 d for GX1+4 [26−28], and many other objects with orbital periods ranging from 11.6 d to 580 d in highly eccentric Be/X-ray binaries [29]).

Observations of phenomena with such a wide range of critical time scales require equipment specially designed in accordance with the following requirements:

—time resolution high enough to sample very short temporal structures (10^{-4} s minimum sampling time);

—sampling time adjustable to a maximum time window that allows "differential" corrections for atmospheric extinction.

Double-head photometers are able to remove variations in the atmospheric transmittance by performing simultaneous measurements of a target and comparison star and are therefore powerful tools in high
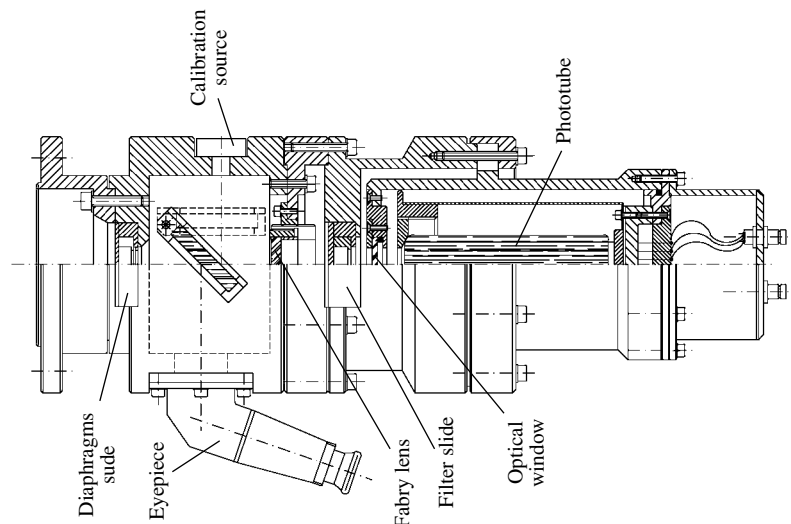
Fig. 1. Mechanical structure of one of the two identical heads of the photometer.

precision studies of stellar variability. The first version of our own two-head photometer became operative in September 1978 [30], enabling observations of V1668 Cyg during a brightness maximum [31]. The tape puncher used at that time as an output device was later replaced with a TM990/101 Texas Instruments computer [32].

The last upgrade, performed in 1997, was necessitated by the obsolescence of the computer. The main changes in the acquisition system were implemented to remove the limitation on the length of observing runs, achieve higher sampling rates, and obtain more direct and intuitive control and management of the observations. This extensive revision of a 20-year-old instrument was justified by the fact that there is currently no suitable alternative measurement technique that can be used for the astrophysical tasks outlined above. Indeed, none of the new panoramic detectors can attain the high speed and high sensitivity of photomultiplier tubes (PMTs) operated in a photon-counting mode.

2. THE OPTO-MECHANICAL STRUCTURE

The two heads of the photometer have the same structure (Fig. 1). They are normally supported by the octagonal mechanical interface of the 152-cm G.D. Cassini telescope at the Loiano Astronomical Station but are easily portable. Two mirrors are placed inside the mechanical interface and are used as beam splitters. One belongs to the offset system that supports the second head, which is used to observe a comparison star, while the other, which is aligned with the optical axis of the telescope, sends a beam to the first head for observations of a target.

This configuration, based on lateral mounting of the two photometric heads and the autoguide system in the Ritchey–Chrétien focal plane, leaves the possibility of simultaneously setting the BFOSC instrumentation [33] in the bottom flange. This enables fast switching from high-speed photometry to CCD imaging or faint-object spectroscopy: a crucial configuration for multi-technique and multi-frequency observations of peculiar objects, such as the accretion-driven sources that are the main targets of our observational program. However, the simultaneous installation of such varied instrumentation in the focal plane prevents us from mounting a third photometric head for simultaneous observations of the sky background.

A second important restriction is the reduced size of the field in which the second photometric head can be displaced to find a suitable comparison star. The mechanical constraints fix the distance between the two diaphragms to be from 13 to 21 arcmin in right ascension and from -6.5 to 6.5 arcmin in declination. A fiber-optic link is provided to enable simultaneous measurements of a tritium lamp calibration source by the two heads. This makes it possible to verify the threshold levels and the overall operation of the entire acquisition electronics. An alternative solution is to replace the optical link with light-emitting diode (LED) lamp calibrators, which is very useful for tests of the system performance.

Standard U, B, and V filters are mounted on a slide, which also has a hole to enable measurements of faint stars without any filter. The left part of Table 1 shows the bands, relative glasses, and thicknesses of the filters. In addition to the usual filter system, a special slide with UBV filters and an ORIEL neutral five-magnitude attenuation filter for each band is

Table 1. The two filter sets: standard (left) and supplementary (right)

Band	Glasses	Thickness, mm	Band	Glasses	Thickness, mm
U	UG2	2	*U*	UG2 + N	2 + 1
B	BG12 + GG385	1 + 2	*B*	BG12 + GG385 + N	1 + 2 + 1
V	GG485	2	*V*	GG485 + N	2 + 1 + 1
−	−	0	−	−	0

Table 2. Diaphragms of the photometer for head 1 (left) and head 2 (right)

Hole	Diameter, mm	Diameter, arcsec	Hole	Diameter, mm	Diameter, arcsec
1	1.10 ± 0.03	18.7	1	1.15 ± 0.03	19.6
2	1.80 ± 0.03	30.6	2	1.85 ± 0.03	31.5
3	2.43 ± 0.03	41.3	3	2.61 ± 0.03	44.4
4	2.80 ± 0.03	47.6	4	2.90 ± 0.03	49.3
5	20.0 ± 0.03	340.0	5	20.0 ± 0.03	340.0

Table 3. PMT characteristics

Head	Tube	Cathode sensitivity, A/L	Voltage, V	Dark current, nA
1	EMI 6256SA	9.3×10^{-2}	1170	1.4
2	EMI 6256SA	9.5×10^{-2}	1140	0.4

available. The right part of Table 1 shows the bands, relative glasses, and thicknesses corresponding to this filter set. The diaphragm holes are in a slide carrying five phosphore−bronze thin (0.3 mm) disks, as indicated in Table 2.

The old EMI 6256S PMTs were later replayed with two EMI 6256SA tubes selected because they have the same anode sensitivity at the same operating voltage (Table 3). Table 3 presents the cathode sensitivity, dark current at 2000 A/L, and voltage of these photomultipliers, which have a S13 spectral response.

The acquisition of a reliable and continuous time series requires regular motion of the telescope and a good auto-guide system. In our case, this is provided by a computer-controlled CCD tracking system, normally used for CCD imaging. We observe the target with the first photometric head, mounted in a flange centered on the optical axis corresponding to the normal output of the telescope. A strong offset cross slide [34] is used to shift the second photometric head in the focal plane to find a comparison star. No remote control of filters is needed and no mechanical actuators are used, so that the two photometric heads have

a very simple and durable structure. Two discriminators, which are modifications of the discriminator of Taylor [35], are mounted near the photomultipliers on thermostatic housings powered by active temperature controls.

3. DATA ACQUISITION SYSTEM

The electronics of the system have been fully rebuilt (Fig. 2). The two counters receive the three main synchronization signals: latch strobe, counts clear, and data-transmission start. These signals are produced by cascade monostables from a programmable timer unit that scales the 10 MHz oscillator frequency (HP 10811A/B) to the requested sampling time. In this way, all the twin counters' operation is driven by a high-stability oscillator that is used as an external clock reference. The photometer is the master: the sampling frequency is synchronous with the prescaled clock. The computer is slave: its job is to asynchronously transfer the data to the mass storage unit. The only condition that must be satisfied is that the transfer of the last obtained counts be completed before the refresh of the latches with the next set of incoming counts.
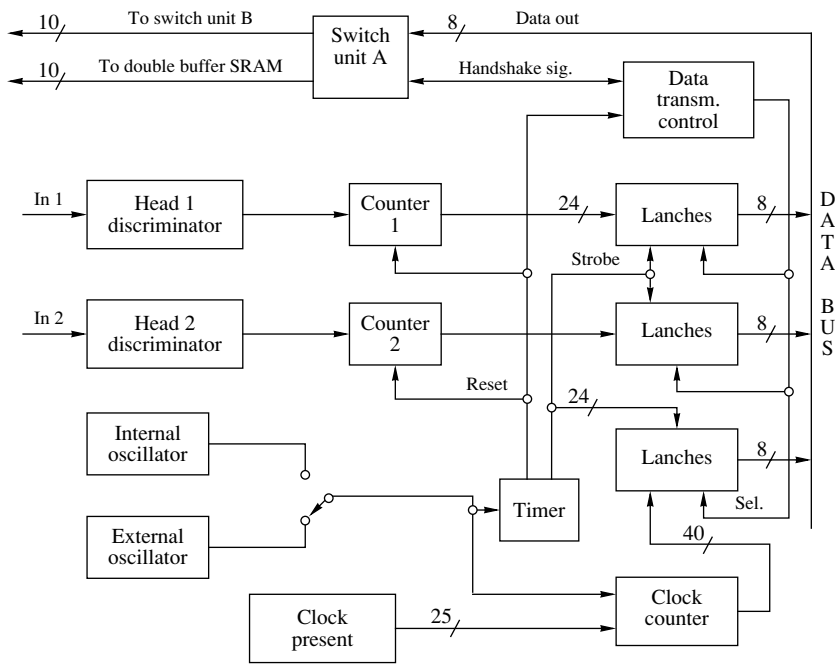
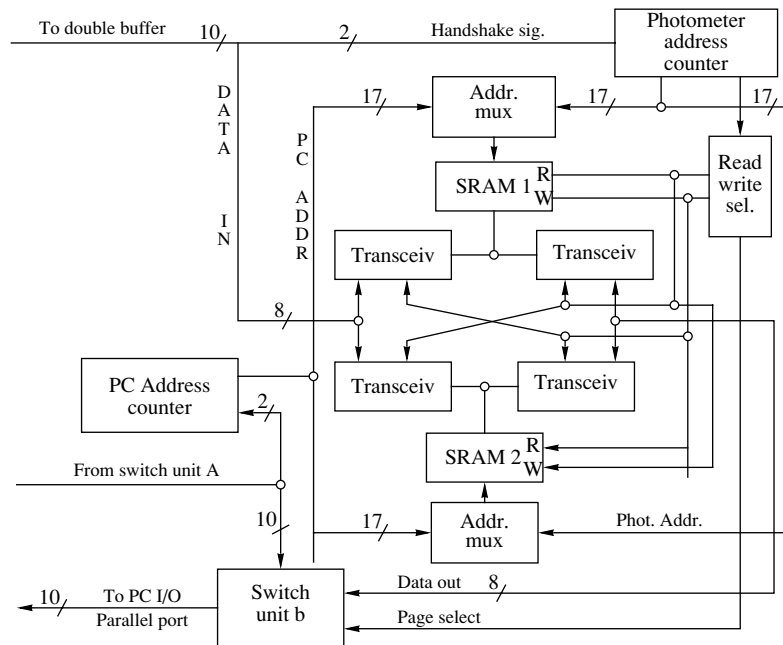**Fig. 2.** Block diagram of the system: counter electronics.

Fig. 3. Block diagram of the system: double buffer SRAM memory.

No cumulative delay is inserted in the sampling time, so that the acquisition is fully synchronous with the main clock. The output control of the three-state latches (used as temporary storage devices) is monitored during the data transfer to enable data transmission during the acquisition of the next set of counts. In this scheme, the personal computer is a slave machine, working only to discharge the latches and display the results on the PC monitor before the arrival of the new data. This fact imposes time constraints, mainly because the computer is a non-synchronous machine: during critical internal operations, such as the refresh cycles for the DRAM memory, it is not able to manage the handshake signals that drive the activity of the parallel-port interface. In practice, it is possible to take data without in-

troducing errors at rates of up to ten samples per second. A special dual-memory/dual-port buffer has been designed and installed in the data acquisition system to enable photometry with higher sampling rates.

4. THE INTERNAL SRAM DOUBLE BUFFER

The dual buffer is composed of two 128 kilobyte SRAM memories and the electronics needed to multiplex the address lines and the data lines between the computer and data acquisition system. When the photometer is writing on one section of the buffer, the computer is reading the other section. The generation of the addresses for the two memory blocks is done by two different address counters, working from the handshake signals of the photometer and computer, respectively. The exchange of the two memory pages and of the read/write control signals is driven by the photometer address counter with the leading edge of the higher address line, which is used only for this purpose. The complex structure of the dual-port double buffer is presented in the simplified block diagram in Fig. 3.

5. MONITORING OF OBSERVATIONS

Owing to the particular structure of the electronics, we can choose between two different data acquisition regimes: direct and double-buffer acquisition. In the direct regime, the dual-port double memory buffer is bypassed and the computer is connected directly to the photometer; in the double-buffer regime, the photometer is connected to the memory buffer, which works as an interface between the instrument and computer.

When the sampling time is sufficient to allow scaling calculations and the execution of simple graphic operations to switch on a pixel on the screen, the data are decoded and stored so that the light curve can be displayed in real time. The screen is divided in half by a horizontal line, enabling display of the light curve and the original data. The mean counts for the two heads are displayed in different colors in the upper window. A scaling factor is derived based on a preliminary analysis of the incoming data performed to obtain a stable mean and identify the median count levels for both heads. After the calculation of the optimal parameters for the window coordinates, the original counts are scaled and referenced to the center of the lower window, where the points are displayed as they are obtained. The window buffer is used cyclically: when the pixel position reaches the right edge of the screen, the trace restarts from the left edge.

The use of the real-time display is restricted to the direct-acquisition regime, since the storage of data in the double memory buffer prevents continuous reading of the data. Moreover, data acquisition in the double-buffer regime requires nearly all the CPU time for the data decoding and storing routines. Therefore, this regime is used only when the sampling rate is critical. The acquisition software for the direct-acquisition regime consists of a C++ program to receive and de-scramble the data, decode the 11 bytes carrying the BCD information of any single measurement, and draw the light curve and rebinned light curve on the screen. To ensure that the transfer of data in the double-buffer regime is constrained only by the capacity of the hard disk, we use a program in assembly code, without visual inspection of the data in real time. This case provides the minimum sampling time of 10^{-4} s.

6. DATA REDUCTION AND ANALYSIS

The main problem connected with the data analysis is detrending. Any trends coming from incorrect estimation of the extinction and from variations in the transparency during the observations introduce many peaks in the Fourier spectra, which must be treated as artefacts and eliminated if we wish to extract possible periodicities from the stellar fluxes. The data reduction can be considered a preliminary step in the preparation of the data for analysis and includes the following procedures:

—estimation of the difference between the instrumental magnitudes of the two stars;

—independent estimation of the instrumental magnitudes of the two stars;

—correction of the counts for the variable star using normalization coefficients derived from the data for the comparison star.

The first step can act successfully as a detrending procedure if the noise introduced by the comparison star during the calculation of the magnitude difference is negligible. This condition can be attained via digital filtering or obtaining "running means" of the counts for the comparison star. Since the two stars are in the same focal plane and are observed through nearly identical air masses, the extinction corrections become second-order effects and can be easily applied. This approach is subject to the inherent risk of ascribing some unknown periodicity associated with the comparison star to the variable star.

The second step eliminates this possibility via a comparison of the results of Fourier analyses for both the target and comparison star. Any periodicity in the signal of both stars is disregarded. If a periodicity is detected in the signal for the comparison star, additional observations using a different comparison star are needed.

The third step should be performed primarily when the comparison star is faint. In this case, direct calculation of the magnitude difference would introduce noise due to the numerical instability of the signal. Reliable normalization coefficients are obtained using a filtering process. If the color indices of the two stars differ, residual extinction effects can survive to the normalization process. To eliminate further problems in calculating the Fourier spectrum, we additionally flatten the normalized output file by subtracting a mean trend, obtained via a spline interpolation or other conventional smoothing methods.

After computing the Fourier power spectra, the most prominent peaks are compared with the local noise mean power [36], taken to represent the 1σ level. Peaks exceeding 5σ are considered "interesting" for further checks, which must be performed using folding techniques, as described in [37].

7. PERFORMANCE TESTS

During normal photometer operations, the BetaLight tritium lamp calibration source is connected to the photometric heads using two fiber-optics bundles. During the calibration test, we replaced the fiber bundles with two LED light sources. In each photometric head, the LED light is sent to the PMT by the optically polished and aluminized retrosurface of the mirror normally used for the diaphragm viewer. The experimental setup is shown in Fig. 4. The signal produced by a sinusoidal oscillator is mixed with the voltage coming from a DC power supply and is sent to the light emitter of head-1, while the light emitter of head-2 is fed by a second DC generator.

The next few figures show the results of a short selection of the full tests we performed to check the response of the instrument to high and low modulation depths and to low (from 0.1 to 5 Hz) and high (from 10 Hz to more than 1 kHz) modulation frequencies. The upper panels of Fig. 5 present the results of a test in which the light was pulsed with a frequency of 0.401 Hz and a modulation depth of 83%. The measurements were obtained in the direct-acquisition regime, taking 1704 samples with a sampling frequency of 10 Hz. The presence of harmonics can be easily explained by the distortion of the sinusoidal light due to the poor quality of the generator, and the non-linear output of the LEDs when powered with high-amplitude pulses.

Results of a second test are shown in the lower panel of the same figure. The LED light was pulsed at a frequency of 0.7446 Hz with a 0.5% modulation depth, and was measured in the direct-acquisition regime, taking 13 042 samples with the same sampling frequency of 10 Hz.

The upper panel of Fig. 6 presents the results of a test with a higher sampling frequency: the modulation depth was 5%, the light modulation frequency was about 5 Hz, the sampling frequency was 100 Hz, and the number of samples was 3303. We used the double-buffer acquisition regime for these measurements. The middle panel shows an example of fast double-buffer measurements: the sampling time was 1 ms, the modulation depth was 5%, and the number of samples was 11 889. The Fourier-amplitude plot shows a restricted view of the frequency domain. No other harmonics exceeding the 3σ level are present in the full frequency range.

An example of a very fast measurement is shown in the lower panel of Fig. 6: the sampling frequency was 10 KHz, the calibration lamp was pulsed at a frequency of 41.275 Hz with a modulation depth of 2.59%, and the duration of the acquisition run was 59.5769 s. The light curve for this run appears poor, due to the low counting rate obtained in each 0.1 ms bin, and does not show the sinusoidal modulation, which is hidden by quantization noise. However, the power spectrum (left panel) and an enlarged view (right panel) show the high purity of the spectrum and the high stability against noise due to the large number of samples and the absence of contamination from atmospheric transmission.

8. LINEARITY TESTS

An additional test was performed to check the linearity of the system. The main source of deviations from linearity is poor determination of the discriminator dead time. The dead time of our discriminator was determined in the construction phase to be 150 ns, taking into account the suggested maximum output current to provide the best stability and longevity of the photomultiplier tubes. This value, which is well matched with the chosen maximum count rate of 0.5 MHz, corresponds under operational conditions (anode sensitivity 2000 A/L, gain 2.1×10^7) to a mean anode current of $\sim 2\mu$A, which is low enough to ensure longevity and good stability of the PMTs. This choice also provides a good match to the pulse duration required for safe operation of the TTL and CMOS logic circuits used in the counter electronics.

The chosen dead time needed to be confirmed with good precision measurements. There are two ways to do this: the dead time can be determined by fitting observational data for a sample of stars with very different luminosities or it can be derived from laboratory measurements. Because the first method is strongly dependent on the atmospheric conditions on the observation night, we chose the second method. The measurement system consisted of a double-pulse generator, a variable attenuator to match the output
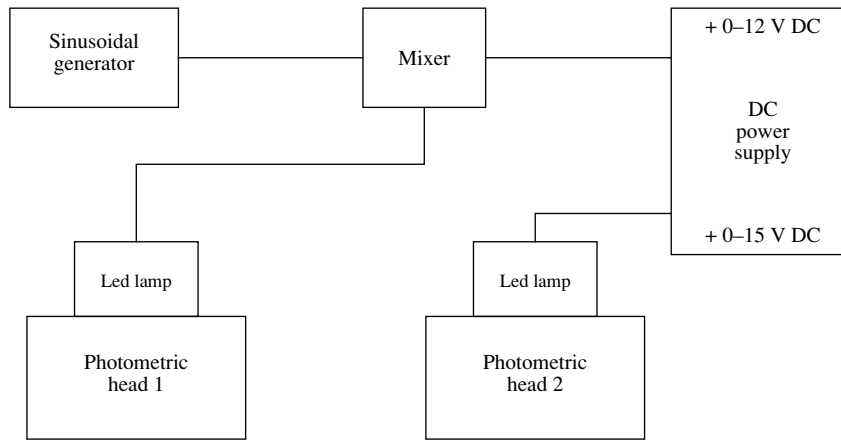
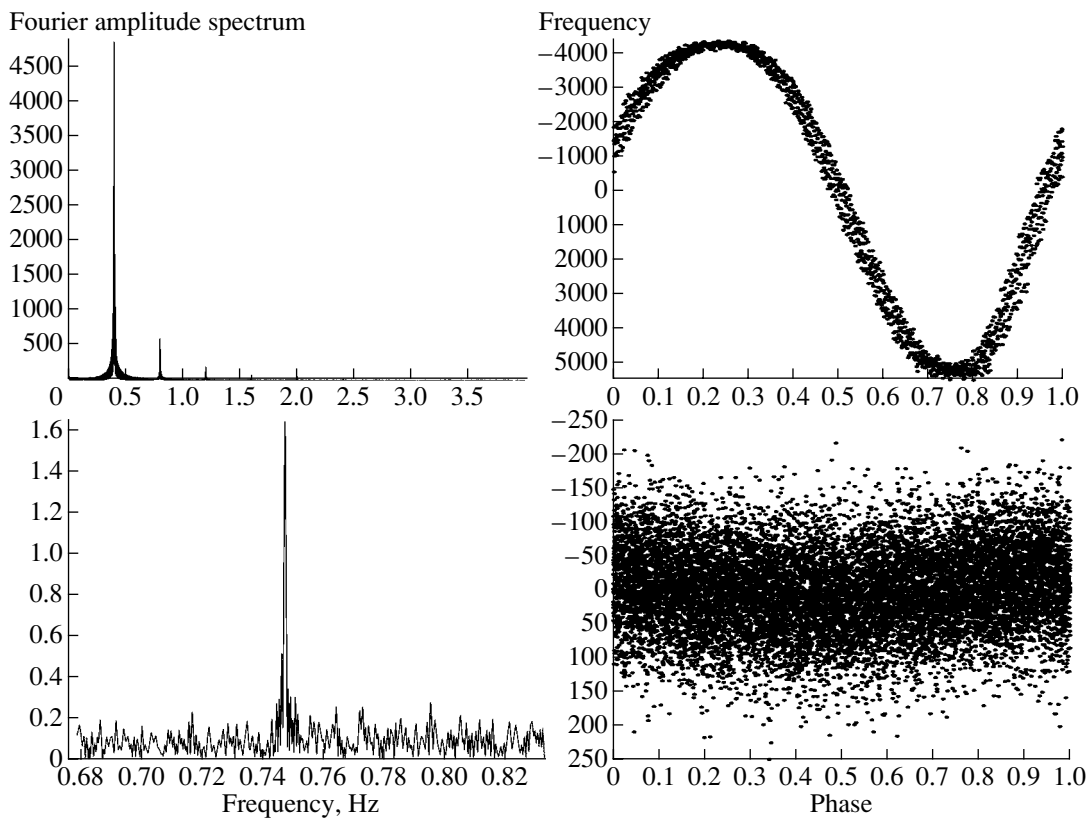**Fig. 4.** Experimental setup for test measurements.

Fig. 5. Direct acquisition regime. Upper panels: test with high modulation depth. Lower panels: test with very low modulation depth.

signal of the generator to the input level of the discriminators, and a good dual-trace oscilloscope.

Looking at the output of the discriminator, we changed the delay between the pair of pulses (1 ns rise-time, 10 ns duration) until the oscilloscope output showed only one pulse in place of two, indicating that the incoming double pulses were separated by less than the dead time. Using this value, we then did a second check observing a standard light source with a set of neutral filters. The plots of these measurements did not show any significant deviation from linearity.

9. EXAMPLES OF REAL OBSERVATIONS

We changed the configuration of the data acquisition system to enable real-time monitoring of the data
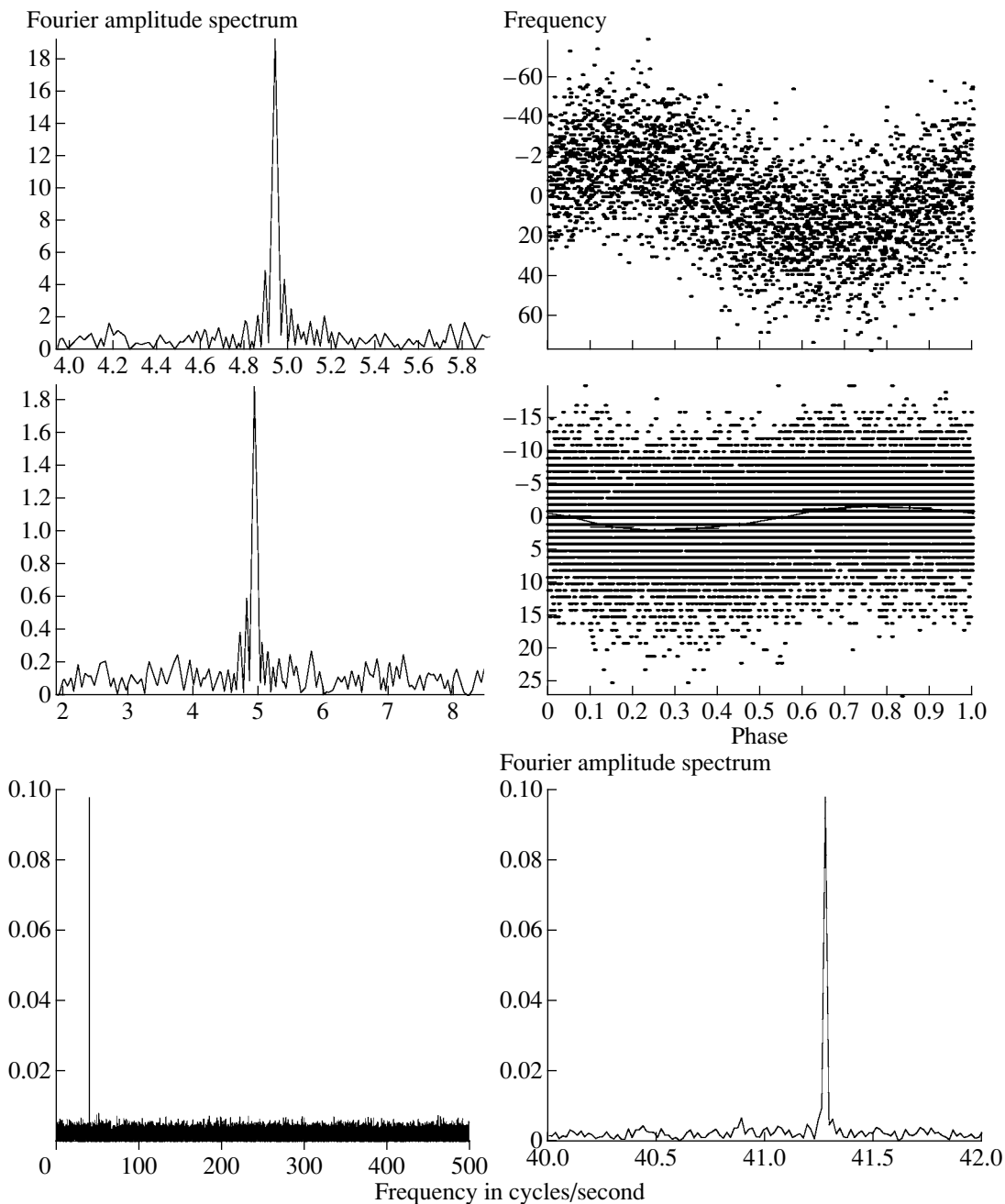
Fig. 6. Tests with double-buffer acquisition regime. Upper panels: low modulation depth, sampling frequency 100 Hz. Middle panels: low modulation, high sampling frequency (1 kHz). Lower panels: very high sampling frequency (10 kHz).

and the possibility of fast observations of unlimited duration. This did not change the photometric quality of the system, so that we will consider examples of observations without regard to the observation date.

The possibility of removing trends purely by calculating the magnitude difference for the two stars (i.e., without correcting for differential extinction) is illustrated by a comparison of the two light curves in the upper panels of Fig. 7. Each plot shows the difference in the magnitudes of the two stars (target

and comparison) and the instrumental magnitude of the comparison star.

Observations of large variations of the contact binary XY Leo were obtained with the old photometer configuration on January 25, 1991 under good sky conditions (upper left-panel). The umbrella-like shape of the comparison light curve is due to the atmospheric extinction. We observed the full orbital period of this object ($V_{\min} = 10.93^m$) over a continuous run of ~ 7.7 h with 1-s sampling time, interrupted
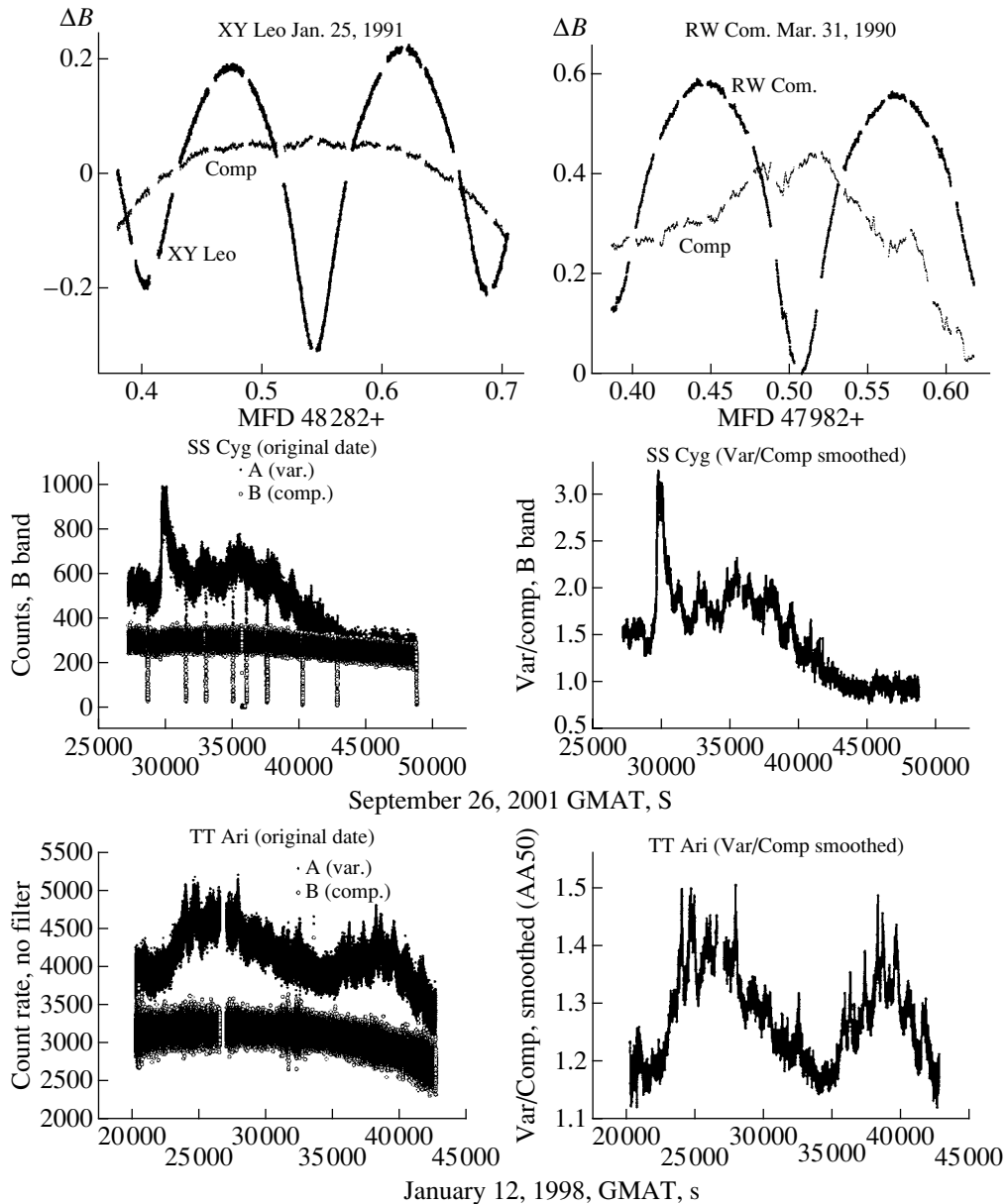
Fig. 7. Test on sky. The two rebinned light curves in the upper panels show similar results under quite different sky conditions: good conditions for observations of XY Leo (left) and bad conditions for observations of RW Com (right). The middle panels show observations of a miniburst in SS Cyg (left) and the corresponding detrended light curve (right). The lower panels show observations of TT Ari with a sampling time of 0.1 s. The original data (left) and the ratio of the target and comparison star counts after sky subtraction (right) are shown. The two contiguous runs are separated by a short break due to the sky background measurements.

only by a few short breaks to measure the sky background.

B-band observations of the similar system RW Com ($V_{\min} = 11.76^m$) were obtained using the same procedure on March 31, 1990 under poor sky conditions. The run length was ~ 6.2 h and the sampling time was 3 s. In this case, the light curve of the comparison star shows large variations in the sky transparency, which cannot be removed by the atmospheric-extinction calculations, as is usually

done for observations obtained under photometric conditions.

The magnitude differences reported in the two graphs were derived from the sky-detrended count ratios without additional correction for differential extinction. These magnitude-difference plots illustrate that, even at this incomplete phase in the data reduction, large variations in the atmospheric transmittance are almost fully removed in both cases.

The middle left panel of Fig. 7 presents a re-
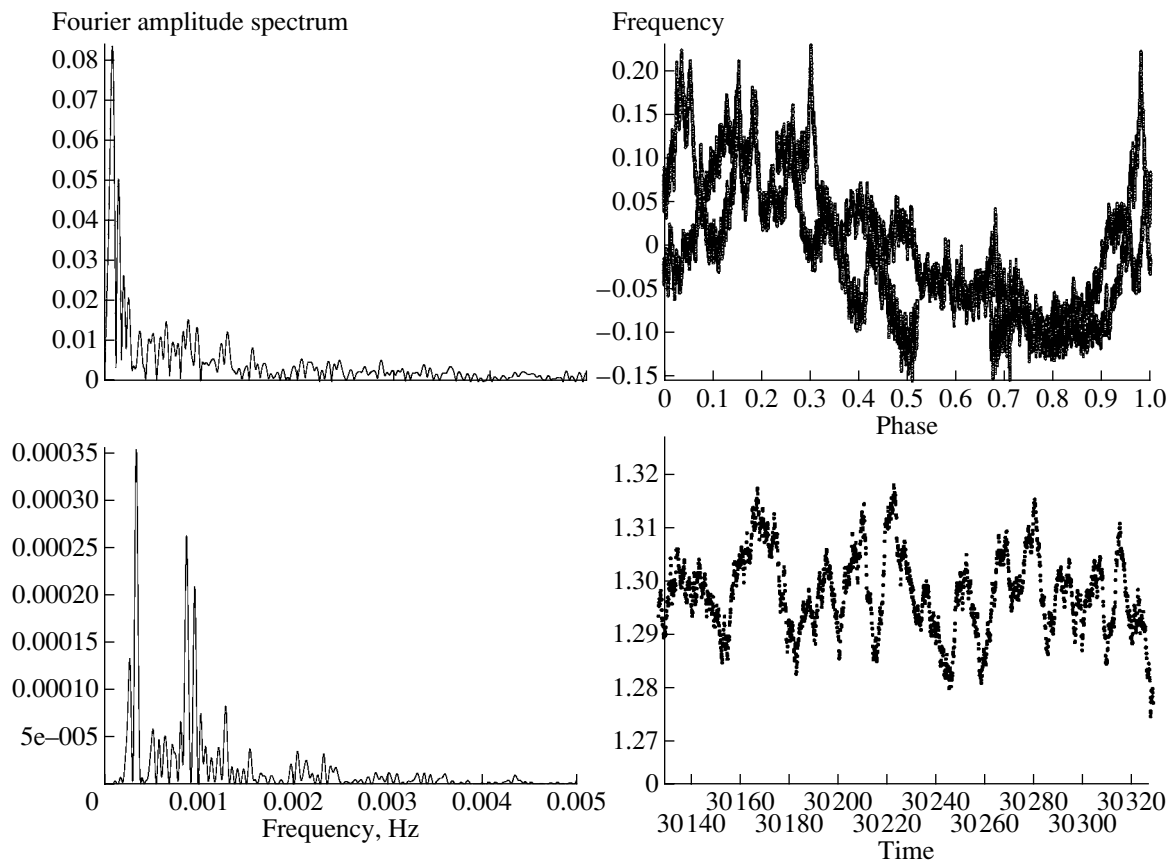
Fig. 8. Discrete Fourier Transforms of the TT Ari light curve. The upper-left panel shows the Fourier amplitude spectrum obtained from the count ratios. The upper-right panel shows the phase graph computed for the frequency featuring the highest amplitude. The lower-left panel presents the spectral power derived from an analysis of the residuals after subtracting the first three highest-amplitude frequencies from the data stream. The lower-right panel presents the complex temporal structures characterizing the TT Ari light curve in more detail.

cent B-band observation of SS Cyg (215 381 points) obtained with the new photometer configuration on September 26, 2001. The transient event observed is not unusual for SS Cyg during quiescent phases. It sometimes shows such "small" outbursts, which can also be observed in some other dwarf novae and are due to a sporadic enhancement of the accretion-disk luminosity (e.g. [5]). The sharp leading edge of the transient profile is described with good time resolution (0.1 s sampling time). The vertical lines are the traces of the sky measurements, performed, in this case, by moving the telescope without interrupting the observation. The upper curve (A) corresponds to the target count rate, while the lower curve (B) corresponds to the comparison star. The middle right panel of Fig. 7 shows a more detailed view of the light curve processed with a running mean filter over 50 samples, which obviously reduces the noise as well as fast variability traces. The input file for the numerical filter was obtained after dividing the sky-subtracted target counts by those of the comparison star.

The lower left panel of Fig. 7 shows the original data for an observation of the cataclysmic variable TT Ari ($V_{\min} = 11.8^m$) on January 18, 1998 covering more than one orbital period, while the lower right panel shows the ratio of the signals for the target and comparison star after subtracting the sky background. No smoothing or correction for differential extinction or for the displacement from the solar-system barycenter has been applied to either the counts or the times in this very preliminary phase of the data analysis.

A first crude temporal analysis performed using Discrete Fourier Transforms highlights the complex structure of the light curve (Fig. 8), which is dominated by a large photometric wave that hides fast variations and appears to be correlated with the orbital phase. The phase graph shows that the asymmetric photometric wave modulated by the fast variations is consistent with the orbital periodicity reported in [38]; the fine structures seem to be correlated with the orbital phase. The fifth highest frequency in amplitude

in the plot obtained from the residual analysis corresponds within the errors to the 13.9-min periodicity suggested in [39].

Other examples of light curves obtained with our double-head photon-counting photometer during a campaign with the so-called Whole Earth Telescope [40] can be accessed over the internet [41]. Our photometer has also been used recently in an observing campaign targeting a sample of hot sdBs and sdOs subdwarf stars, searching for pulsational instabilities [37, 42]; we were able to detect oscillations to the very low amplitude of 3 mmag.

Information about the dynamics of the photometer can be gleaned from our observations of Nova Cyg 78 [31]. Our first observations of this object using the photometer on the 1.5-m G. D. Cassini telescope of Bologna University were obtained when it was at its maximum brightness ($V_{\max} \sim 6.8^m$) on September 12, 1978; two years later, on August 27, 1981, we measured its brightness to be $V \sim 17.9^m$.

The paper [43] demonstrates the possibilities provided by the ability to simultaneously mount a photometer and spectrograph: the Nova Cyg 78 spectrum was obtained on September 29, 1978, after photometric observations performed with our photometer. Obviously, this ability must be traded off with a restricted range of slide displacements when searching for suitable comparison stars.

10. ACKNOWLEDGMENTS

REFERENCES

1. F. Giovannelli and L. Sabau-Graziati, Astrophys. Space Sci. **276**, 67 (2001).
2. J. Kristian, C. R. Pennypacker, M. A. Middletich, *et al.*, Nature **338**, 234 (1989).
3. B. Warner, in *IAU Colloquium № 15, 1972,* p. 144.
4. F. Giovannelli, Space Sci. Rev. **30**, 213 (1981).
5. F. Giovannelli and G. Martinez-Pais, Space Sci. Rev. **56**, 313 (1991).
6. K. Horne and R. Gomer, Astrophys. J. **237**, 845 (1980).
7. S. Mereghetti, in *Frontier Objects in Astrophysics and Particle Physics,* Ed. by F. Giovannelli and G. Mannocchi, SIF Conf. Proc. **73**, 239 (2001).
8. M. van der Klis, in *The Origin and Evolution of Neutron Stars,* Ed. by D. J. Helfand and J. H. Huang (D. Reidel, Dordrecht, 1987), p. 321.
9. M. van der Klis, Ann. Rev. Astron. Astrophys. **27**, 517 (1989).
10. M. van der Klis, Ann. Rev. Astron. Astrophys. **38**, 717 (2000).
11. M. Cropper, J. W. Menzies, and S. Tapia, Mon. Not. R. Astron. Soc. **218**, 201 (1986).
12. J. Middleditch and J. Nelson, Astrophys. J. **208**, 567 (1976).
13. J. Patterson, E. L. Robinson, and A. L. Kiplinger, Astrophys. J. Lett. **226**, L137 (1978).
14. R. E. Nather, Publ. Astron. Soc. Pac. **90**, 447 (1978).
15. M. Cropper, Mon. Not. R. Astron. Soc. **222**, 225 (1986).
16. B. Warner, in *IAU Symposium № 73: Structure and Evolution of Close Binary Systems,* Ed. by P. Eggleton, S. Miton, and J. Whelan (D. Reidel, Dordrecht, 1976), p. 85.
17. M. Cropper and B. Warner, Mon. Not. R. Astron. Soc. **220**, 633 (1986).
18. C. Bartolini, G. Bianco, A. Guarnieri, *et al.*, Hvar Obs. Bull. **7** (1), 159 (1983).
19. F. Giovannelli and L. Sabau-Graziati, Space. Sci. Rev. **59**, 1 (1992).
20. R. H. Hildebrand, E. J. Spillar, and R. F. Stiening, Astrophys. J. **243**, 223 (1981).
21. I. G. Martinez-Pais, F. Giovannelli, C. Rossi, and S. Gaudenzi, Astron. Astrophys. **291**, 455 (1994).
22. J. van Paradijs, M. van der Klis, and H. Pedersen, Astron. Astrophys. **225**, L5 (1989).
23. J. van Paradijs, M. van der Klis, S. van Amerongen, *et al.*, Astron. Astrophys. **234**, 181 (1990).
24. C. Chevalier, S. A. Ilovaisky, J. van Paradijs, *et al.*, Astron. Astrophys. **210**, 114 (1989).
25. A. Guarnieri, C. Bartolini, A. Piccioni, and F. Giovannelli, in *Multifrequency Behavior of Galactic Accreting Sources,* Ed. by F. Giovannelli (Editrice SIDEREA, Roma, 1985), p. 310.
26. J. Braga, M. G. Pereira, and F. J. Jablonski, in *Proceedings of the Fifth Compton Symposium,* Ed. by M. L. McConnell and J. M. Ryan, AIP Conf. Proc. **510**, 188 (2000).
27. M. G. Pereira, J. Braga, and F. J. Jablonski, Astrophys. J. Lett. **526**, L105 (1999).
28. M. G. Pereira, J. Braga, and F. J. Jablonski, Astrophys. J. Lett. **533**, L69 (2000).
29. G. M. H. J. Habets, Astron. Astrophys. **184**, 209 (1987).
30. A. Piccioni, C. Bartolini, A. Guarnieri, and F. Giovannelli, Acta Astron. **29** (3), 463 (1979).
31. A. Piccioni, A. Guarnieri, C. Bartolini, and F. Giovannelli, Acta Astron. **34** (4), 473 (1984).
32. G. Cosentino, Thesis (Bologna University, 1985).
33. R. Merighi, M. Mignoli, C. Ciattaglia, *et al., BFOS: Bologna Faint Object Spectrograph and Camera,* Bologna Astronomical Observatory Internal Report 09-1994-05.
34. A. Braccesi, Giornale di Astronomia (SAIt) **1**, 135 (1975).

35. D. J. Taylor, Publ. Astron. Soc. Pac. **92**, 108 (1980).

36. J. Kepler, Baltic Astron. **2**, 515 (1993).

37. A. Piccioni, C. Bartolini, S. Bernabei, *et al.*, ESA SP-485 (2001) (in press).

38. A. Schwarzenberg-Czerny, Acta Astron. **37**, 213 (1987).

39. C. R. Robinson, Ph. D. Thesis (The Pennsylvania State University, 1996).

40. R. E. Nather, D. E. Winget, J. C. Clemens, *et al.*, Astrophys. J. **361**, 309 (1990).

41. http://wet.iitap.iastate.edu/xcov17/datalog/lo1004.gif−lo1013.gif−lo1614.gif−lo1804.gif

42. A. Piccioni, C. Bartolini, S. Bernabei, *et al.*, Astron. Astrophys. **354**, L13 (2000).

43. F. Giovannelli, C. Bartolini, A. Guarnieri, *et al.*, Acta Astron. **34** (4), 487 (1984).

Shock Tracers in the Molecular Cloud G1.6−0.025

S. V. Saliĭ, A. M. Sobolev, and N. D. Kalinina

Astronomical Observatory, Ural State University, pr. Lenina 51, Yekaterinburg, 620083 Russia
Received April 17, 2001; in final form, May 23, 2002

Abstract—Observations of the molecular cloud G1.6−0.025 in the 2_K-1_K and $J_0-J_{-1}E$ series and $5_{-1}-4_0E$ line of CH_3OH, the $(2-1)$ and $(3-2)$ lines of SiO, and the $7_{-7}-6_{-6}$ line of HNCO are described. Maps of the previously observed extended cloud with $V_{lsr} \sim 50$ km/s and high-velocity clump with $V_{lsr} \sim 160$ km/s, as well as a newly detected clump with $V_{lsr} \sim 0$ km/s, have been obtained. The extended cloud and high-velocity clump have a nonuniform structure. The linewidths associated with all the objects are between 20 and 35 km/s, as is typical of clouds of the Galactic center. In some directions, emission at velocities from 40 to 160 km/s and from −10 to +75 km/s is observed at the clump boundaries, testifying to a connection between the extended cloud and the high-velocity clump and clump at $V_{lsr} \sim 0$ km/s. Compact maser sources are probaby contributing appreciably to the emission of the extended cloud in the $5_{-1}-4_0E$ CH_3OH line. Non-LTE modeling of the methanol emission shows that the extended cloud and high-velocity clump have a relatively low hydrogen density ($< 10^4$ cm^{-3}). The specific column density of methanol in the extended cloud exceeds 6×10^8 cm^{-3}s, and is $4 \times 10^8-6 \times 10^9$ cm^{-3}s in the high-velocity clump. The kinetic temperatures of the extended cloud and high-velocity clump are estimated to be <80 K and 150−200 K, respectively. Possible mechanisms that can explain the link between the extended cloud with $V_{lsr} \sim 50$ km/s and the clumps with $V_{lsr} \sim 0$ km/s and ~ 160 km/s are briefly discussed. © *2002 MAIK "Nauka/Interperiodica".*

1. INTRODUCTION

The giant molecular cloud G1.6−0.025 (for brevity, we will call it G1.6) is located at the edge of the Galactic center gas−dust complex. This object was first discovered in an H_2CO-absorption survey of the Galactic center region [1]. Observations in NH_3 lines have shown that there are an extended gas cloud moving at velocity $V_{lsr} = 50-75$ km/s and a more compact, high-velocity clump with a size of $d = 5'$ (10 pc at the distance of the Galactic center) with a V_{lsr} of about 160 km/s [2, 3] in the direction of G1.6. The extended cloud consists of several clumps with sizes $d = 2'-5'$ [2]. Kinetic temperatures estimated from the rotational temperature of the NH_3 are ~ 50 K for the cloud with $V_{lsr} \sim 50$ km/s and ~ 120 K for the clump with $V_{lsr} \sim 160$ km/s [2, 3].

Molecular emission with $V_{lsr} \sim 50$ km/s (the extended cloud) and ~ 160 km/s (the high-velocity clump) in the direction of G1.6 is present in surveys of the Galactic center in the ^{13}CO (1−0), CS (2−1) [4], CS (1−0), $C^{34}S$ (1−0) [5], and HCN (1−0) [6] lines. The extended cloud and high-velocity clump have been mapped earlier in the CH_3OH (methanol) $2_0-3_{-1}E$ absorption line [7] and in the CH_3OH $4_{-1}-3_0E$ emission line [8].

The properties of the observed radio lines of various molecules testify to the presence of shock waves propagating in the G1.6 material. For example, G1.6 emits strongly in collisionally excited HNCO transitions, but the emission in radiatively excited transitions is very weak [9]. The ratios of the intensities of molecular-hydrogen emission lines also suggests that they are collisionally excited [10, 11]. Manifestations of shocks are most evident toward the position $\alpha_{1950} = 17^h46^m12^s$, $\delta_{1950} = -27°33'55''$, where narrow maser peaks in the CH_3OH $4_{-1}-3_0E$ line [8, 12], a maser source in the NH_3 (3,3) transition [2], and a probable protostellar cluster [3, 13] have been detected. These shocks probably arose during collisions between high-velocity clumps and the extended cloud [13].

The passage of a shock considerably increases the content of CH_3OH, HNCO, and SiO molecules in the gaseous phase. There is a significant enrichment of the gas in CH_3OH and HNCO molecules due to the release of material from the mantles of dust grains (see, for example, [14−16]). This process also increases the SiO (silicon monoxide) content, though the largest increases of the SiO abundance take place when the evaporation of the mantles is accompanied by the destruction of the cores of dust grains (see, for example, [17, 18]). More than 10^5 years after the

Table 1. System parameters at the observed line frequencies

Transition	Frequency, GHz	T_{sys}, K	HPBW	η_M	η_A	F_ν/T_A, Jy/K	δv, km/s
$CH_3OH\ 5_{-1}-4_0 E$	84.52121	153	58.5″	0.75	0.62	25.2	0.28
$CH_3OH\ 2_K-1_K$	~ 96.7	153	51.2	0.73	0.61	25.6	0.25
SiO (2−1)	86.84699	124	57.0	0.75	0.62	25.2	0.28
SiO (3−2)	130.26870	220	38.0	0.69	0.55	28.4	3.22
$HNCO\ 7_{-7}-6_{-6}$	153.86509	293	32.2	0.67	0.51	30.6	2.73
$CH_3OH\ J_0-J_{-1}, 2_1-3_0 A^+$	~ 157	318	32.0	0.66	0.50	30.7	2.68

passage of the shock, the content of these molecules decreases and comes into agreement with those observed in quiescent interstellar gas [18]. This explains why the largest contribution to the emission in the CH_3OH, SiO, and HNCO lines comes from regions whose chemical composition has been modified by the relatively recent passage of a shock.

Elucidating the physicochemical and evolutionary status of G1.6 is connected with studies of shock tracers. In this paper, we analyze the spatial distribution and intensity ratios of lines of CH_3OH, SiO, and HNCO, which are the brightest lines in the regions subject to the effects of the shocks.

2. OBSERVATIONS

The observations were carried out in March 1996 on the 15-m SEST telescope in La Silla (Chile). In the observations of the $CH_3OH\ 2_K-1_K$ line series and the SiO (2−1) and $CH_3OH\ 5_{-1}-4_0 E$ lines, we used a 100-GHz SIS receiver with an acousto-optical high-resolution spectrometer (HRS, 83.6 MHz bandwidth). We simultaneously observed the $HNCO\ 7_{-7}-6_{-6}$ and SiO (3−2) lines using a 150-GHz SIS receiver with a low-resolution spectrometer (LRS2, band 1000 MHz). The observations were carried out in an ON−OFF mode. The calibration was performed using the chopper-wheel method.

In October 1999, we additionally observed the $CH_3OH\ J_0-J_{-1} E$ line series using the 150-GHz SIS receiver with a low-resolution spectrometer (LRS1, band 1008 MHz). These observations were carried out in a dual beam-switching mode.

The system temperature (T_{sys}), beam size (HPBW), antenna efficiency (η_A), main beam efficiency (η_M), flux to antenna-temperature ratio (F_ν/T_A), and spectrometer resolution (δv) at the frequencies of the observed lines are listed in Table 1.

We mapped a $12' \times 8'$ region centered on $\alpha = 17^h 46^m 10^s$, $\delta = -27°33'00''$ with $60''$ steps in right ascension and declination. The integration time varied from one minute at the map edges to 16 min

toward the center. The spectra were processed using the CLASS software package. In the high-resolution spectra, we subtracted a first-order baseline level and, in the low-resolution spectra, a second- or third-order baseline level.

3. RESULTS

A selection of the most representative spectra of the observed lines is given in Figs. 1−3. Our spectra show components corresponding to the extended cloud with velocity ~ 50 km/s and high-velocity clump with velocity ~ 160 km/s. In addition, we detected emission from a compact clump with $V_{lsr} \sim 0$ km/s in the $CH_3OH\ 2_K-1_K$, SiO (2−1), and SiO (3−2) lines. We also found bright emission in the $CH_3OH\ 5_{-1}-4_0 E$ line in the direction $\sim (120'', -120'')$.

When the emission peaks in our observations agree in position and velocity with those in the Haystack observations of Haschick and Baan [8], we have used their notation for these peaks, Am−Fm. Two new components with $V_{lsr} \sim 160$ km/s and $V_{lsr} \sim 0$ km/s are present in our spectra. By analogy, we call the corresponding peaks Gm and Hm. The results of Gaussian fitting to the emission peaks are given in Table 2. The locations of the objects on the map of the $CH_3OH\ 2_K-1_K$ emission is shown in Fig. 4.

3.1. Extended Cloud with $V_{lsr} \sim 50$ km/s

The component corresponding to the extended cloud with a velocity of about 50 km/s is present in the spectra of all the lines. The line intensities at the map edges are comparable to those at the center (Fig. 4). Thus, we can only estimate a lower limit to the cloud size, $> 12' \times 8'$.

3.1.1. Blend of the $CH_3OH\ 2_K-1_K$ lines and the SiO (2−1) line. When centered on the $2_{-1}-1_{-1} E$ line at 96.73939 GHz, four methanol lines
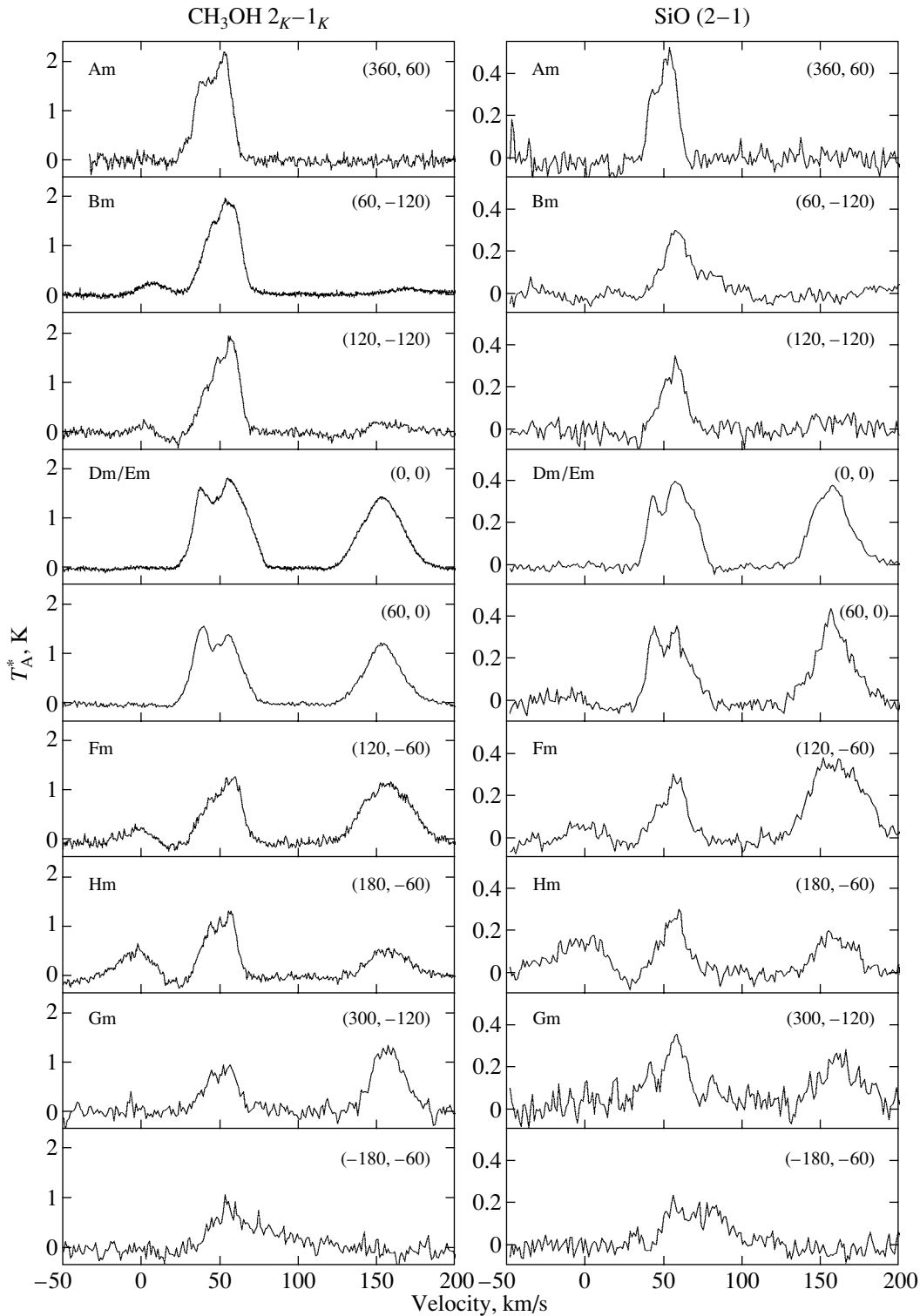
Fig. 1. Typical spectra of the CH$_3$OH 2_K−1_K and SiO $(2$−$1)$ lines. The top right corner of each spectrum gives the position of the observed point relative to the coordinate origin $(\alpha = 17^h46^m10^s, \delta = -27°33'00'')$ in arcsec. The top left corner gives the name assigned to the peak of the integrated intensity.

of the 2_K−1_K series fall within the spectrometer band. The 2_{-1}−$1_{-1}\,E$, 2_0−$1_0\,E$, and 2_0−$1_0\,A^+$ lines are blended. In various directions, the blend width varies

from 22 to 34 km/s, and the brightness temperatures, from 0.5 to 2 K. No emission in the CH$_3$OH 2_1−$1_1\,E$ line, which is separated from the blend by 16 MHz,
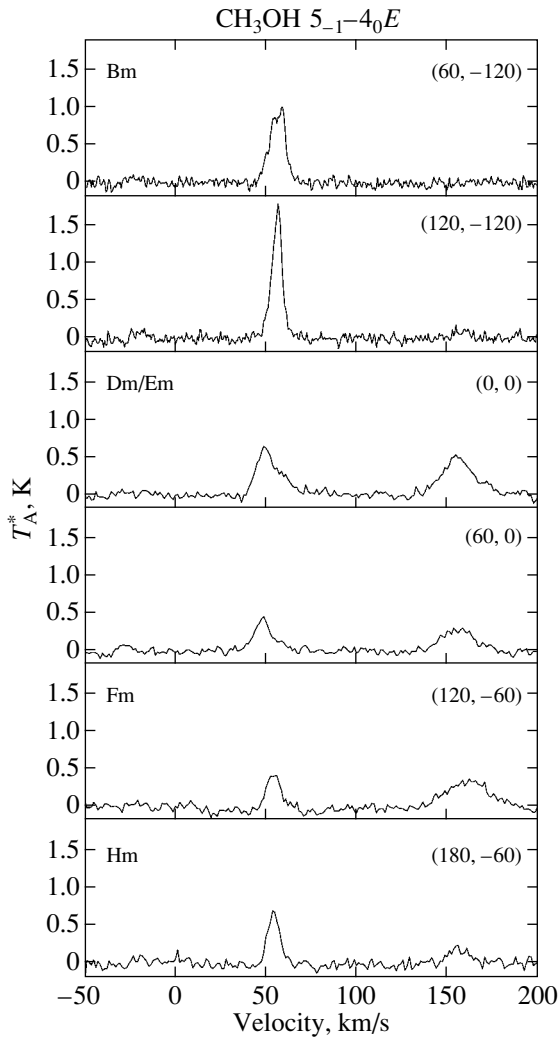
CH$_3$OH $5_{-1}-4_0 E$

Fig. 2. Same as Fig. 1 for the CH$_3$OH $5_{-1}-4_0 E$ line.

was detected. However, we cannot completely rule out the presence of emission in this line in directions where the component with $V_{lsr} \sim 0$ km/s (described in Section 3.3) is present.

The intensity distribution in the CH$_3$OH 2_K-1_K and SiO (2−1) lines has three maxima at $(360'', 60'')$, $(60'', -120'')$ and $(0'', 0'')$, corresponding to the Am, Bm, and Dm intensity peaks of [8]. The greatest intensity is observed toward Am (Table 2). The Am/Dm intensity ratio is ~1.1 for methanol and ~1.2 for silicon monoxide; the Am/Bm ratios are approximately 1.1 and 1.8, respectively.

The velocities of the main components of the extended cloud in the SiO (2−1) and CH$_3$OH 2_K-1_K lines vary across the mapped area from 45 to 75 km/s (Fig. 5). The velocity variations are similar to that observed in the NH$_3$ [2] and CH$_3$OH $2_{-1}-3_0 E$ [7] lines. The small differences are associated with differences

in the boundaries of the areas and the arrangement of the observed points.

At 20−80 km/s, the distribution of the integrated (over velocity) intensity in the CH$_3$OH 2_K-1_K lines has two pronounced peaks toward $(360'', 60'')$ and $(0'', 0'')$, which coincide with Am and Dm (Fig. 4). Here and below, we use the word "peak" to designate a maximum in the spatial distribution of the integrated intensity. At 50−60 km/s, there is a prominent peak in the integrated intensity toward $(60'', -120'')$, which coincides with Bm. The map of the SiO (2−1) line emission is similar to the emission in the CH$_3$OH 2_K-1_K lines.

In all directions, the line profiles differ significantly from Gaussians. The emission of the extended cloud is fitted well by a set of Gaussians with different velocities. Complex profiles cannot be uniquely decomposed into components. Nevertheless, we can confidently identify a spectral component with $V_{lsr} \sim 43$ km/s near $(0'', 0'')$, since it has clearly visible spectral counterparts (spectra toward $(60'', 0'')$, Figs. 1−3). This component is observed in the velocity interval $V_{lsr} = 43-45$ km/s in the SiO (2−1) line, and in the broader velocity range $V_{lsr} = 35-47$ km/s in the CH$_3$OH 2_K-1_K lines, since the latter emission is represented by a blend of three lines. The emission with $V_{lsr} \sim 43$ km/s is present in a $1' \times 1.5'$ region extended perpendicular to the line connecting the emission peaks of the high-velocity clump.

Some spectra of the CH$_3$OH 2_K-1_K and SiO (2−1) lines have an extended red wing to the northwest of $(0'', 0'')$, testifying to the presence of gas with velocities of 40−160 km/s in this region (see spectra toward $(-180'', 60'')$ in Fig. 1). The presence of material with such velocities is also reflected in the velocity−position plot in Fig. 6.

A single bright spectral component at a velocity of ~ 0 km/s is observed in the vicinity of $(180'', -60'')$ (Fig. 1). The parameters of this component are described in Section 3.3.

3.1.2. The CH$_3$OH $5_{-1}-4_0 E$ line. The integrated intensity of this line at velocities $V_{lsr} = 40-70$ km/s has peaks at $\sim (120'', -120'')$ and $(0'', 0'')$, corresponding to the Bm and Dm emission maxima (Fig. 7). The intensity peak corresponding to Bm is extended in the east−west direction. Analysis of the spectra shows that the position of the peak near Bm shifts westward with increasing velocity. The line profile differs significantly from Gaussian in all directions (Fig. 2), but the maser peaks are much less pronounced in the CH$_3$OH $5_{-1}-4_0 E$ line than in the CH$_3$OH $4_{-1}-3_0 E$ line [8].

The brightest emission is observed toward $\sim (120'', -120'')$. A good fit in this direction is
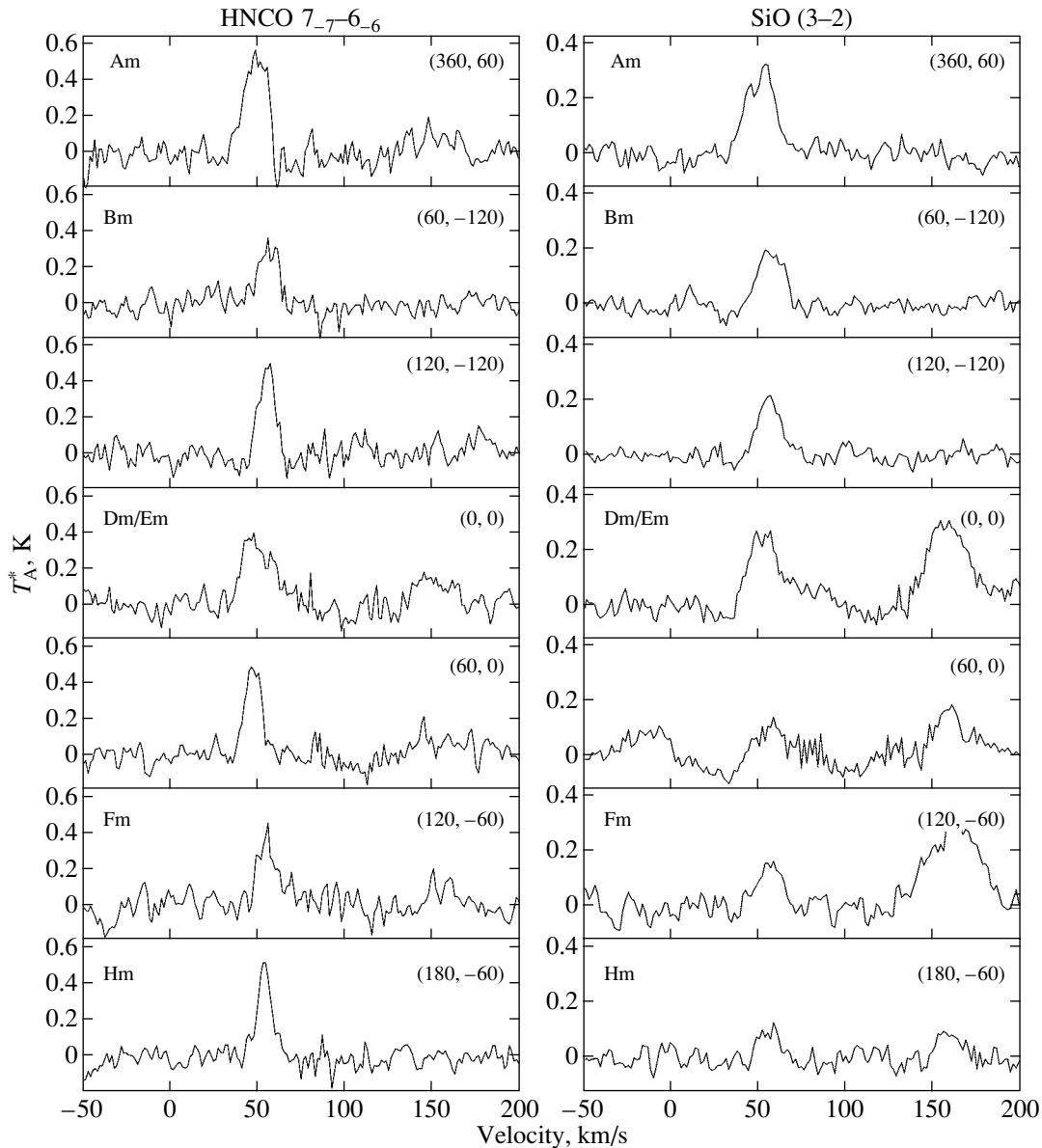
Fig. 3. Same as Fig. 1 for the HNCO 7_{-7}−6_{-6} and SiO (3−2) lines, observed with low spectral resolution.

achieved with two Gaussians with $V_{lsr} = 57.2$ and 55.7 km/s. The second emission maximum, which has about one-third the intensity of the main maximum, is observed toward $(0'', 0'')$. The spectrum in this direction is well approximated by two Gaussian components with $V_{lsr} \sim 45$ km/s and ~ 52 km/s. We can see on the radial-velocity map in Fig. 5 that the distribution of the emission-peak velocities is similar to that observed in the CH_3OH 2_K−1_K and SiO (2−1) lines.

An increase of the emission intensity in the northeast and southwest is observed at the map boundaries. This suggests the presence of other molecular clumps emitting in the CH_3OH 5_{-1}−4_0 E line in G1.6.

3.1.3. The HNCO 7_{-7}−6_{-6} and SiO (3−2) lines. The observations in these lines were carried out with low spectral resolution. The baselines of the low-resolution spectra for the ON−OFF-mode SEST observations are considerably nonlinear. This does not allow us to map the intensity distributions accurately. The line parameters are listed in Table 2. The spectra in selected directions are shown in Fig. 3.

The intensity distribution of the emission of the extended cloud in both lines is close to that observed in the CH_3OH 2_K−1_K and SiO (2−1) lines. The Am/Dm intensity ratio is ~ 1.6 in the HNCO 7_{-7}−6_{-6} line and approximately 1.2 in the SiO (2−1)

Table 2. Results of Gaussian fitting. The names of intensity maxima are listed

Transition	Central frequency, GHz	$\Delta\alpha, \Delta\delta$, arcsec	Name of intensity maximum	T_A^*, K	V_{lsr}, km/s	ΔV_{lsr}, km/s	$\int T_A^*$, K km/s
CH_3OH	96.74138	$(0, 0)$	Dm	1.78	58.25 ± 0.02	34.11 ± 0.04	64.7 ± 0.08
$2_K - 1_K$		$(60, -120)$	Bm	1.87	59.07 ± 0.03	22.45 ± 0.06	44.8 ± 0.11
		$(360, 60)$	Am	2.03	53.41 ± 0.09	23.41 ± 0.19	50.5 ± 0.39
		$(180, -60)$	Hm	0.58	2.06 ± 0.21	24.18 ± 0.47	15.0 ± 0.25
		$(0, 0)$	Em	1.42	159.49 ± 0.01	30.19 ± 0.06	45.6 ± 0.07
		$(120, -60)$	Fm	1.20	162.84 ± 0.53	36.75 ± 0.53	46.8 ± 0.28
		$(300, -120)$	Gm	1.29	163.18 ± 0.02	23.63 ± 0.70	32.4 ± 0.82
SiO	86.84699	$(0, 0)$	Dm	0.40	59.42 ± 0.10	22.80 ± 0.23	11.8 ± 0.06
$(2-1)$		$(60, -120)$	Bm	0.27	59.76 ± 0.28	24.11 ± 0.82	7.61 ± 0.16
		$(360, 60)$	Am	0.48	51.19 ± 0.17	16.67 ± 0.35	8.49 ± 0.17
		$(180, -60)$	Hm	0.14	-1.96 ± 0.77	26.75 ± 1.51	2.25 ± 0.17
		$(0, 0)$	Em	0.37	156.15 ± 0.01	27.30 ± 0.19	11.0 ± 0.09
		$(120, -60)$	Fm	0.37	159.57 ± 0.22	37.72 ± 0.49	16.5 ± 0.39
		$(300, -120)$	Gm	0.19	162.19 ± 0.69	28.23 ± 1.57	5.68 ± 0.33
CH_3OH	84.52121	$(0, 0)$	Dm	0.57	50.93 ± 0.13	14.61 ± 0.30	9.23 ± 0.22
$5_{-1} - 4_0\, E$		$(120, -120)$	Bm	1.66	56.25 ± 0.04	6.86 ± 0.10	12.1 ± 0.18
		$(0, 0)$	Em	0.48	156.27 ± 1.02	21.15 ± 0.43	11.0 ± 0.26
		$(120, -60)$	Fm	0.35	161.12 ± 0.30	26.87 ± 0.67	10.3 ± 0.32
CH_3OH	157.27085	$(0, 0)$	Dm	0.06	60.47 ± 1.94	26.64 ± 4.17	1.63 ± 0.22
$J_{-1} - J_0$		$(0, 0)$	Em	0.11	152.82 ± 0.96	30.42 ± 1.94	3.57 ± 0.22
CH_3OH	156.60241	$(0, 0)$	Dm	-0.11	51.80 ± 0.96	28.05 ± 2.08	-3.15 ± 0.21
$2_1 - 3_0\, A^+$		$(0, 0)$	Em	-0.09	161.84 ± 1.10	25.70 ± 2.89	-2.40 ± 0.22
SiO	130.26870	$(0, 0)$	Dm	0.26	54.10 ± 0.69	22.89 ± 1.66	5.76 ± 0.35
$(3-2)$		$(360, 60)$	Am	0.30	51.38 ± 0.17	19.56 ± 0.89	6.23 ± 0.25
		$(0, 0)$	Em	0.30	158.22 ± 0.62	26.97 ± 1.50	8.96 ± 0.47
		$(60, 0)$	Hm	0.10	-14.12 ± 1.90	23.64 ± 3.70	2.43 ± 0.37
HNCO	153.86509	$(0, 0)$	Dm	0.37	50.60 ± 0.84	27.96 ± 2.39	8.07 ± 0.57
$7_{-7} - 6_{-6}$		$(360, 60)$	Am	0.57	48.67 ± 0.32	13.97 ± 0.63	8.50 ± 0.41
		$(0, 0)$	Em	0.15	155.01 ± 3.48	63.71 ± 14.38	3.66 ± 0.47

line. Peaks corresponding to an additional component with $V_{lsr} \sim 43$ km/s are visible in the spectra near $(0'', -60'')$.

3.1.4. The CH$_3$OH $J_{-1} - J_0\, E$ line series and the CH$_3$OH $2_1 - 3_0\, A^+$ line. Observations of these lines were carried out in only two directions: $(0'', 0'')$ and $(180'', -60'')$. Eight CH$_3$OH lines of the $J_{-1} - J_0\, E$ series and the CH$_3$OH $2_1 - 3_0\, A^+$ line fell into the spectrometer bandwidth. The corresponding transitions are characterized by considerable deviations from LTE, and give rise to class II methanol masers, which are relatively bright and widespread [19, 20]. In our spectra, emission in the blend of the three CH$_3$OH lines $2_{-1} - 2_0\, E$, $3_{-1} - 3_0\, E$, and $1_{-1} - 1_0\, E$ and absorption in the CH$_3$OH $2_1 - 3_0\, A^+$
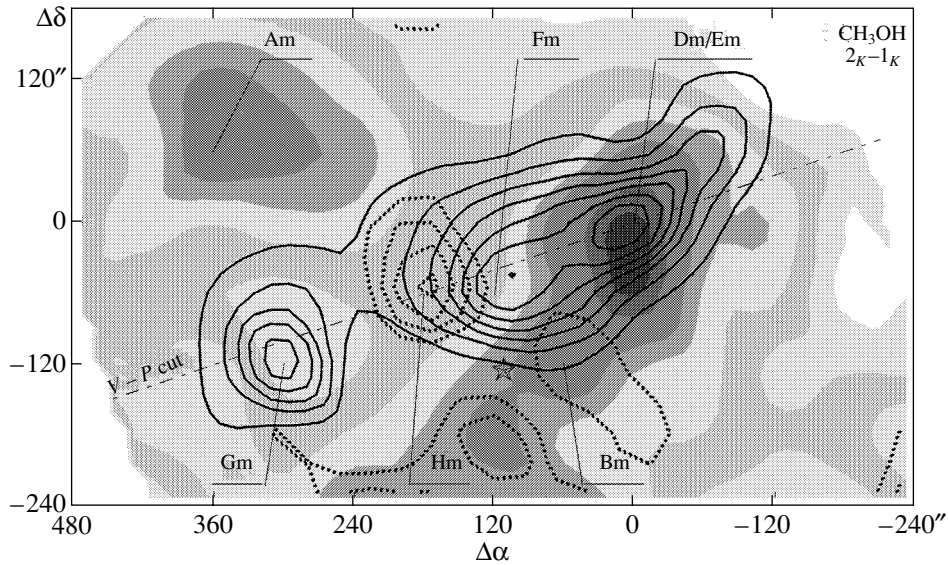
Fig. 4. Map of the intensity integrated over V_{lsr} in the CH_3OH 2_K-1_K line blend. The gray scale corresponds to the integrated emission of the extended cloud (V_{lsr} in the interval 20−80 km/s). The gray scale shows regions with integrated intensities from 6 to 62 K km/s in steps of 6 K km/s. The solid contours show the integrated emission of the high-velocity clump from 5 to 41 K km/s in steps of 6 K km/s. The dashed contours show the integrated emission of the clump with $V_{lsr} = 20-30$ km/s from 4 to 10 K km/s in steps of 2 K km/s. The dashed line marked "$V - P$ cut" shows the cross section used for the velocity−position plot. The star marks the position of the maser in the CH_3OH $5_{-1}-4_0$ E line.
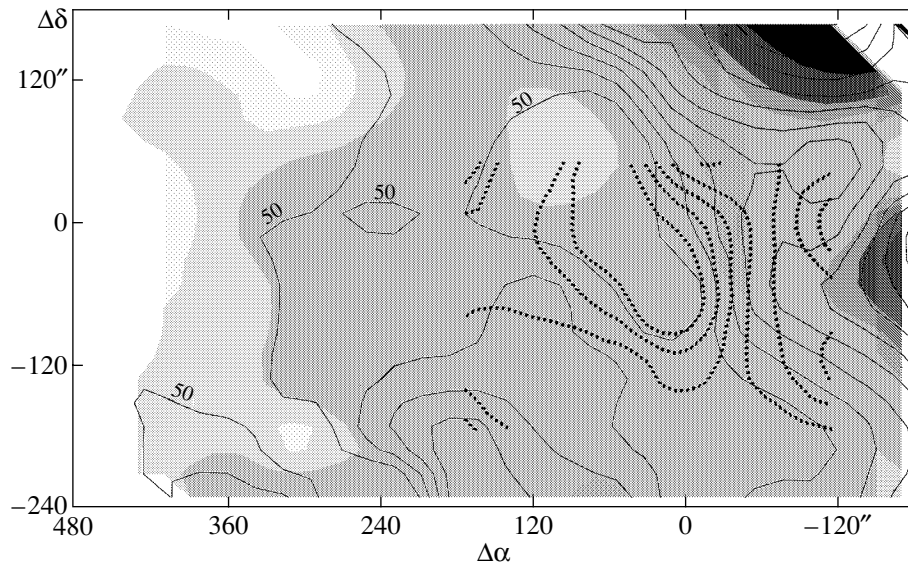
Fig. 5. Map of radial velocities from 50 to 80 km/s in steps of 5 km/s. The gray scale shows the emission in the SiO (2−1) line; the solid contours show the emission in the CH_3OH 2_K-1_K blend; and the dashed contours show the emission in the CH_3OH $5_{-1}-4_0$ E line. The CH_3OH $5_{-1}-4_0$ E contours are cut at the boundary of the area observed in this line.

line are confidently detected at a noise level of 0.04 K. The characteristics of the lines are listed in Table 2.

3.2. The High-Velocity Clump with $V_{lsr} \sim 160$ km/s

The component with a velocity of ~ 160 km/s, corresponding to the high-velocity clump, is confidently detected in the spectra of all the lines we

recorded. The emission is distributed in a region $\sim 8' \times 5'$ in size (at 10% of the peak intensity) that is extended from southeast to northwest. The width of the blend of the 2_K-1_K methanol lines varies from 20 to 35 km/s, the width of the SiO (2−1) line from 17 to 39 km/s, and the width of the methanol $5_{-1}-4_0$
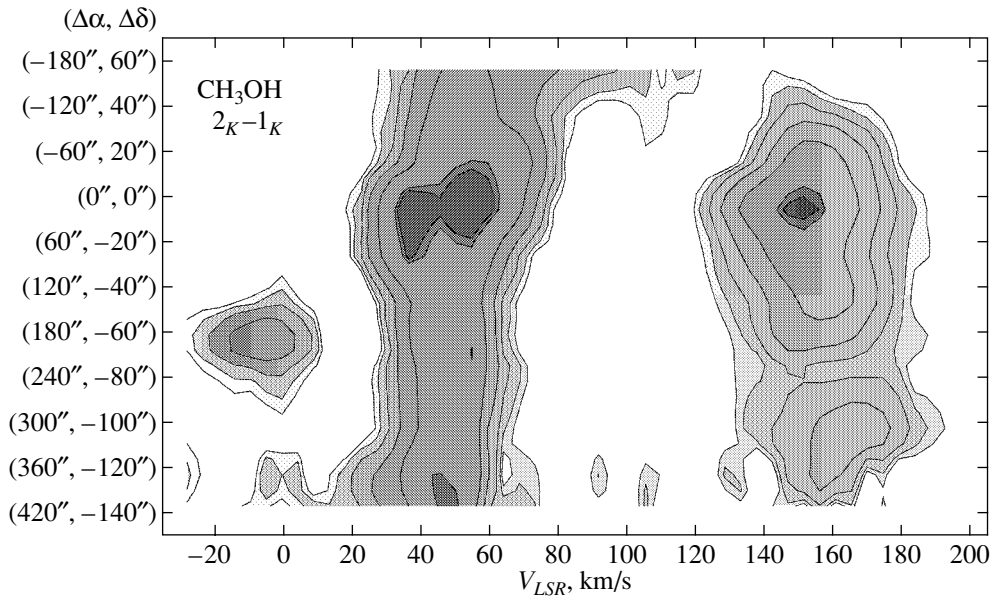
Fig. 6. Velocity–position plot for the CH_3OH 2_K-1_K blend.
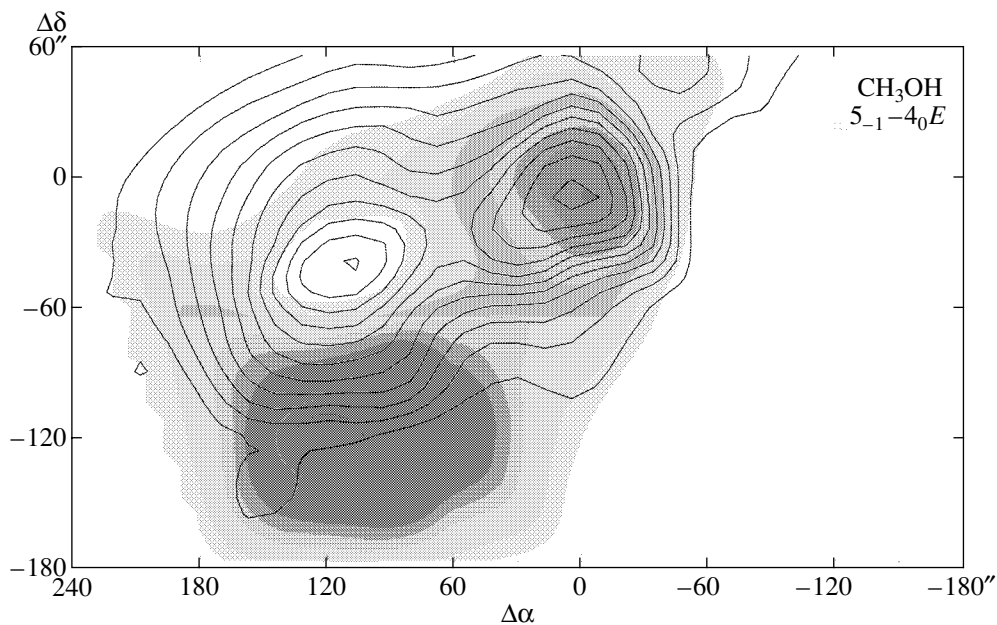
Fig. 7. Map of the integrated intensity in the CH_3OH $5_{-1}-4_0$ E line. The gray scale shows the integrated emission of the extended cloud from 1.3 to 13 K km/s in steps of 1.0 K km/s, and the solid contours show the integrated emission of the high-velocity clump from 1.1 to 12 K km/s in steps of 1.0 K km/s.

line from 16 to 27 km/s. The velocity V_{lsr} km/s varies from 150 to 170 km/s.

3.2.1. The blend of the CH_3OH 2_K-1_K lines and the SiO (2−1) line. The emission of these lines has three peaks of the integrated intensity in the velocity range $V_{lsr} = 120-180$ km/s (Fig. 4). Two of them coincide with the Em and Fm intensity maxima of [8]. The peak toward $(300'', -120'')$ had not

been detected in earlier observations. We have called this emission maximum Gm, by analogy with [8]. The intensities of Em, Fm, and Gm in the CH_3OH 2_K-1_K lines are ~ 1.4, ~ 1.2, and ~ 1.3 K, respectively. The corresponding intensities in the SiO (2−1) line are ~ 0.4, ~ 0.4, and ~ 0.2 K. Emission from the high-velocity clump was not detected in the CH_3OH 2_1-1_1 E line.

All the peaks are located along a single line in the southeast−northwest direction. We will call this the axis of the high-velocity clump. The separation between the Em and Fm maxima is $\sim 2'$, while Fm and Gm are separated by about $3'$. The position of Em in the lines we observed coincides with the position of the Dm maximum of the extended cloud. The positions of the Fm and Gm intensity peaks fall in the region of minimum integrated intensity of the extended cloud (Fig. 4). Differences in the radial velocities of the detected clumps are small compared to the linewidth (see Table 2).

3.2.2. The CH_3OH $5_{-1}-4_0$ E line. The peaks of the integrated intensity coinciding with Em and Fm are clearly distinguished (Fig. 7). We have no observations in the area of Gm. The peak corresponding to Em is observed in the same direction as the peak corresponding to the Dm maximum of the extended-cloud emission. The position of the Fm emission maximum coincides with the minimum extended-cloud emission. The emission in the region of Em is in the velocity interval 155−170 km/s and is in the broader interval 150−180 km/s in the vicinity of Fm. The Em intensity is ~ 0.5 K, and the Em/Fm intensity ratio is ~ 1.4. The linewidth varies from 21 to 27 km/s.

3.2.3. The HNCO $7_{-7}-6_{-6}$ and SiO $(3-2)$ lines. The positions of the intensity maxima of the high-velocity clump in the SiO $(3-2)$ line coincide with those in the CH_3OH 2_K-1_K and SiO $(2-1)$ lines. This similarity extends to the intensity ratios of the high-velocity clump and extended cloud.

The intensity distribution of the high-velocity clump emission in the HNCO $7_{-7}-6_{-6}$ line differs from that in the CH_3OH and SiO lines. In all the spectra, it is approximately a factor of 2.5 lower than the intensity of the extended-cloud emission. Toward the Gm maximum, the emission cannot be distinguished at a noise level of ~ 0.42 K. In addition to the weak emission corresponding to Em and Fm, emission is observed in the vicinity of $(360'', 60'')$, which is absent in the other lines (Fig. 3).

3.2.4. The CH_3OH $J_{-1}-J_0$ E series and the CH_3OH 2_1-3_0 A^+ line. There are components in the spectrum corresponding to the high-velocity clump toward $(0'', 0'')$. Like the extended cloud, the blend of the $2_{-1}-2_0$ E, $1_{-1}-1_0$ E, and $3_{-1}-3_0$ E lines is observed in emission, and the 2_1-3_0 A^+ line is observed in absorption. The characteristics of the spectra are listed in Table 2. The intensity of the blend emission in the high-velocity clump considerably exceeds that in the extended cloud. The intensity of the 2_1-3_0 A^+ line in the high-velocity clump is lower than in the extended cloud.

3.3. Emission of the Component with $V_{lsr} \sim 0$ km/s

In addition to the components corresponding to the extended cloud and high-velocity clump, emission with $V_{lsr} \sim 0$ km/s is observed in the CH_3OH 2_K-1_K, $J_{-1}-J_0$ E, and SiO $(2-1)$ and $(3-2)$ lines (Figs. 1, 3). The presence of this component in the spectra of different lines indicates that the emission is associated with a real physical object.

The maximum intensity of the emission in the CH_3OH 2_K-1_K and SiO $(2-1)$ lines is observed toward $(180'', -60'')$. The intensity in this direction is ~ 0.6 K in the CH_3OH 2_K-1_K line blend and ~ 0.1 K in the SiO $(2-1)$ line. The linewidths are typical of Galactic-center molecular clouds and are close to those observed in the extended cloud and high-velocity clump (Table 2).

The maximum of the emission with $V_{lsr} \sim 0$ km/s in the SiO $(3-2)$ spectra is shifted approximately $60''$ eastward with respect to the peak of the emission in the CH_3OH 2_K-1_K and SiO $(2-1)$ lines. This probably indicates the presence of a temperature gradient inside the cloud.

The peaks of the integrated intensity at radial velocities from -25 to 10 km/s in the SiO $(2-1)$ and CH_3OH 2_K-1_K lines are located at $(180'', -60'')$, which coincides with the region of minimum emission of the extended cloud, and also falls between the integrated-intensity peaks of the high-velocity clump (Fig. 4).

The velocity−position plot in Fig. 6 shows that emission in the velocity interval from -10 to 75 km/s is observed to the south of the maximum of the component with $V_{lsr} \sim 0$ km/s. This testifies to a probable genetic connection between the clump with $V_{lsr} \sim 0$ km/s and the extended cloud.

3.4. Discussion

Analysis of the observations shows that the extended cloud has a nonuniform structure. The integrated-intensity peaks we observe in the CH_3OH 2_K-1_K and SiO $(2-1)$ lines coincide positionally within the observational accuracy with the peaks of the integrated intensity in the CH_3OH $4_{-1}-3_0$ E line. The highest intensity among the lines considered is observed in Am, whereas the Bm maximum is brighter in the CH_3OH $4_{-1}-3_0$ E line [8]. This difference is most likely connected with the fact that the CH_3OH $4_{-1}-3_0$ E transition is a class I methanol maser transition. Consequently, the emission in this line may contain a considerable contribution from compact maser sources, whereas the emission in the SiO $(2-1)$ and CH_3OH 2_K-1_K lines is quasi-thermal and more accurately reflects the overall distribution of material in the object.

We also observe differences between the intensity maps in the CH$_3$OH 2_K-1_K blend and in the CH$_3$OH $5_{-1}-4_0\,E$ line. The $5_{-1}-4_0\,E$ and $4_{-1}-3_0\,E$ transitions are class I methanol maser transitions [21−23]. Therefore, compact maser sources may also appreciably contribute to the CH$_3$OH $5_{-1}-4_0\,E$ line emission.

The intensities in the CH$_3$OH $5_{-1}-4_0\,E$ line at 13 observed points located within $\leq 90''$ of $(120'', -120'')$ are well fitted by a Gaussian with a width corresponding to the telescope beam. Thus, a considerable fraction of the CH$_3$OH $5_{-1}-4_0\,E$ emission in the vicinity of $(120'', -120'')$ comes from a pointlike source, most probably a maser condensation. The best fit is achieved if the source is located at the point $(110'', -124'')$. Maser peaks in the CH$_3$OH $4_{-1}-3_0\,E$ line are observed near this position [8]. In spite of the obvious difference of the CH$_3$OH $5_{-1}-4_0\,E$ and CH$_3$OH $4_{-1}-3_0\,E$ line profiles, their spectra can be fitted by Gaussians with the same set of radial velocities. Most likely, the emission in these lines is produced by the same type of pumping mechanisms, which, according to theoretical calculations, have shown have a collisional−radiative nature [13]. The position of the maser sources in the CH$_3$OH $5_{-1}-4_0\,E$ and CH$_3$OH $4_{-1}-3_0\,E$ lines coincides with the boundary of the high-velocity clump (Fig. 4). A source of emission in the high-excitation NH$_3$ $(7,7)$ transition is observed in this region [24], implying a high temperature for the emitting object. The bright feature, which is prominent in the ammonia spectrum, has a radial velocity of ~ 58 km/s, close to that of the probable maser in the CH$_3$OH $5_{-1}-4_0\,E$ line.

Analysis of the profiles of the SiO $(2-1)$ and CH$_3$OH lines demonstrates that the velocity of the extended cloud changes from ~ 45 km/s in the eastern part of the mapped area to ~ 75 km/s in the northwestern part. In the northwest part, emission is observed from ~ 40 to ~ 160 km/s.

The spectra of the CH$_3$OH, SiO, and HNCO lines and the velocity-interval maps testify to the presence of an additional spectral component with $V_{\rm lsr} \sim 43$ km/s. The intensity distribution of this component is oriented perpendicular to the axis of the high-velocity clump. The intensity maximum coincides with the position of the source of intense, probably maser, emission in the NH$_3$ $(3,3)$ line with $V_{\rm lsr} \sim 43$ km/s [2].

A component with $V_{\rm lsr} \sim 0$ km/s is prominent in our spectra. Gas with velocities from ~ -10 to ~ 75 km/s is present near the peak corresponding to this component. A similar pattern is observed in survey maps of the Galactic center in the C^{32}S and C^{34}S $(1-0)$ lines [5]. This suggests that the clump corresponding to the emission with $V_{\rm lsr} \sim 0$ km/s is genetically related to the extended cloud.

The high-velocity clump and extended cloud have a nonuniform structure, which is most clearly traced in the CH$_3$OH $5_{-1}-4_0\,E$ line. Fragments are visible both in the intensity maps in the SiO $(2-1)$ and CH$_3$OH 2_K-1_K lines and in the velocity−position plot. The velocity differences between the fragments are considerably smaller than the linewidths. Our maps of the high-velocity clump contain a third emission peak that was not observed earlier, which we have designated Gm. The fragments are arranged along a straight line, which forms the axis of the high-velocity clump.

4. MODELING OF THE METHANOL EMISSION

To estimate the physical parameters of the extended cloud and high-velocity clump, we performed non-LTE modeling of the methanol-line intensities toward $(0'', 0'')$. The modeling was carried out in the Large Velocity Gradient (LVG) approximation. We chose the kinetic temperature T_k, hydrogen density $n_{\rm H}$, specific methanol column density $N_{\rm CH_3OH}/\Delta V$, and filling factor ϕ as model parameters.

We used the data from [7] for the $2_0-3_{-1}\,E$ transition. Since compact maser sources can make a significant contribution to the emission in the $5_{-1}-4_0\,E$ and $4_{-1}-3_0\,E$ lines, we did not use the data for these lines in our modeling. When calculating the intensities of line blends, we used the "all-or-nothing" method [26]. We considered lines to be blended if the relative difference of their frequencies did not exceed 10^{-4}; for nearby lines, this corresponds to a velocity shift of 30 km/s. We assumed that the brightnesses of such lines were identical and equal to the total brightness of the blend.

We searched for the parameters with which the model brightness temperatures were in best agreement with the observed antenna temperatures. The quality of the fit was estimated using the function

$$\chi^2 = \sum_i ((T_{B_i}^{\rm obs} - \phi T_{B_i}^{\rm mod})/\sigma_i)^2,$$

where $T_{B_i}^{\rm obs} = T_{A_i}^*/\eta_M$ is the antenna temperature of line i corrected for the antenna efficiency, $T_{A_i}^*$ the antenna temperature observed in line i (or the corresponding blend), η_M the antenna efficiency, $T_{B_i}^{\rm mod}$ the model brightness temperature of line i, and σ_i the uncertainty of the antenna temperature of line i.

The initial approximation for the temperature was based on temperatures estimated from the NH$_3$ lines [2]: $T_k = 120$ K for the high-velocity clump

**Table 3.** Results of modeling the molecular cloud G1.6−0.025

		Extended cloud			High-velocity clump	
		a1	b1		a2	b2
T_k, K		24.9	53.1		178.7	146.2
$N_{CH_3OH}/\Delta V$, 10^9 cm^{-3} s		4.0	1.7		1.2	0.7
n_H, 10^3 cm^{-3}		2.4	8.4		1.4	7.8
ϕ		0.67	0.34		0.45	0.47
χ^2		6.75	132.08		6.27	4.14
Frequency, GHz	Transition	T_B^{obs}, K	T_B^{mod}, K		T_B^{obs}, K	T_B^{mod}, K	
96.75551	$2_1-1_1 E$	0.00 ± 0.06	0.02	0.01	0.00 ± 0.06	0.00	0.00
96.73936	$2_{-1}-1_{-1} E$	2.44 ± 0.06	2.44	2.44	1.95 ± 0.06	1.95	1.95
96.74455	$2_0-1_0 E$	2.44 ± 0.06	2.44	2.44	1.95 ± 0.06	1.95	1.95
12.17844	$2_0-3_{-1} E$	-1.25 ± 0.18	-1.17	-0.45	-0.38 ± 0.18	-0.39	-0.27
156.48886	$8_0-8_{-1} E$	0.00 ± 0.04	0.00	0.00	0.00 ± 0.04	0.00	0.00
156.82853	$7_0-7_{-1} E$	0.00 ± 0.04	0.00	0.00	0.00 ± 0.04	0.00	0.00
157.04862	$6_0-6_{-1} E$	0.01 ± 0.04	0.00	0.01	0.01 ± 0.04	0.02	0.00
157.17901	$5_0-5_{-1} E$	0.00 ± 0.04	0.00	0.00	0.00 ± 0.04	-0.01	0.01
157.24605	$4_0-4_{-1} E$	0.00 ± 0.04	-0.06	-0.02	0.00 ± 0.04	-0.03	0.00
157.27085	$1_0-1_{-1} E$	0.09 ± 0.04	0.02	0.09	0.17 ± 0.04	-0.03	0.17
157.27239	$3_0-3_{-1} E$	0.09 ± 0.04	0.02	0.09	0.17 ± 0.04	-0.03	0.17
157.27605	$2_0-2_{-1} E$	0.09 ± 0.04	0.02	0.09	0.17 ± 0.04	-0.03	0.17
96.74138	$2_0-1_0 A^+$	2.44 ± 0.06	2.44	2.44	1.95 ± 0.06	1.95	1.95
156.60241	$2_1-3_0 A^+$	-0.17 ± 0.04	-0.15	-0.08	-0.13 ± 0.04	-0.09	-0.06

and $T_k = 50$ K for the extended cloud. The initial values of the hydrogen density and specific column density varied from 10^2 to 10^7 cm^{-3} and from 10^8 to 10^{12} cm^{-3} s, respectively. For both the extended cloud and high-velocity clump, we cannot simultaneously explain satisfactorily the depth of the absorption in the $2_0-3_{-1} E$ and $2_1-3_0 A^+$ lines and the brightness of the emission in the $J_0-J_{-1} E$ blend in a one-component approximation. The absorption in the $2_0-3_{-1} E$ and $2_1-3_0 A^+$ lines can be obtained in models with either lower densities ($\leq 10^{3.25}$ cm^{-3} for the extended cloud and high-velocity clump) or lower temperatures (≤ 25 K for the extended cloud, ≤ 80 K for the high-velocity clump). The emission lines in the $J_0-J_{-1} E$ blend and these absorption lines probably form in different parts of clouds with differing physical parameters. Table 3 presents the resulting models for the extended cloud and high-velocity clump in which the best fits for the absorption lines (columns a1, a2)

and for the emission of the $J_0-J_{-1} E$ blend (columns b1, b2) are achieved.

To find the ranges of physical parameters yielding a satisfactory agreement with the observations, we calculated a grid of models. The density and specific column density were varied in the intervals $\log(n_H$ [cm^{-3}]$) = 2.75-5.5$ and $\log(N_{CH_3OH}/\Delta V$ [cm^{-3}s]$) = 8.0-10.75$. The temperature was varied in the intervals $T_k = 10-120$ and $80-220$ K for the extended cloud and high-velocity clump, respectively.

The calculations demonstrate that the observational data impose the following restrictions on the cloud parameters: $\log(n_H$ [cm^{-3}]$) \leq 3.75$, $\log(N_{CH_3OH}/\Delta V$ [cm^{-3}s]$) \geq 8.75$, $T_k \leq 80$ K for the extended cloud and $\log(n_H$[cm^{-3}]$) \leq 4.25$, $\log(N_{CH_3OH}/\Delta V$ [cm^{-3}s]$) = 8.5-9.75$, $T_k = 150-200$ K for the high-velocity clump. The temperature dependence in the interval $80-220$ K is determined only by the data for the $J_0-J_{-1} E$ blend. The kinetic
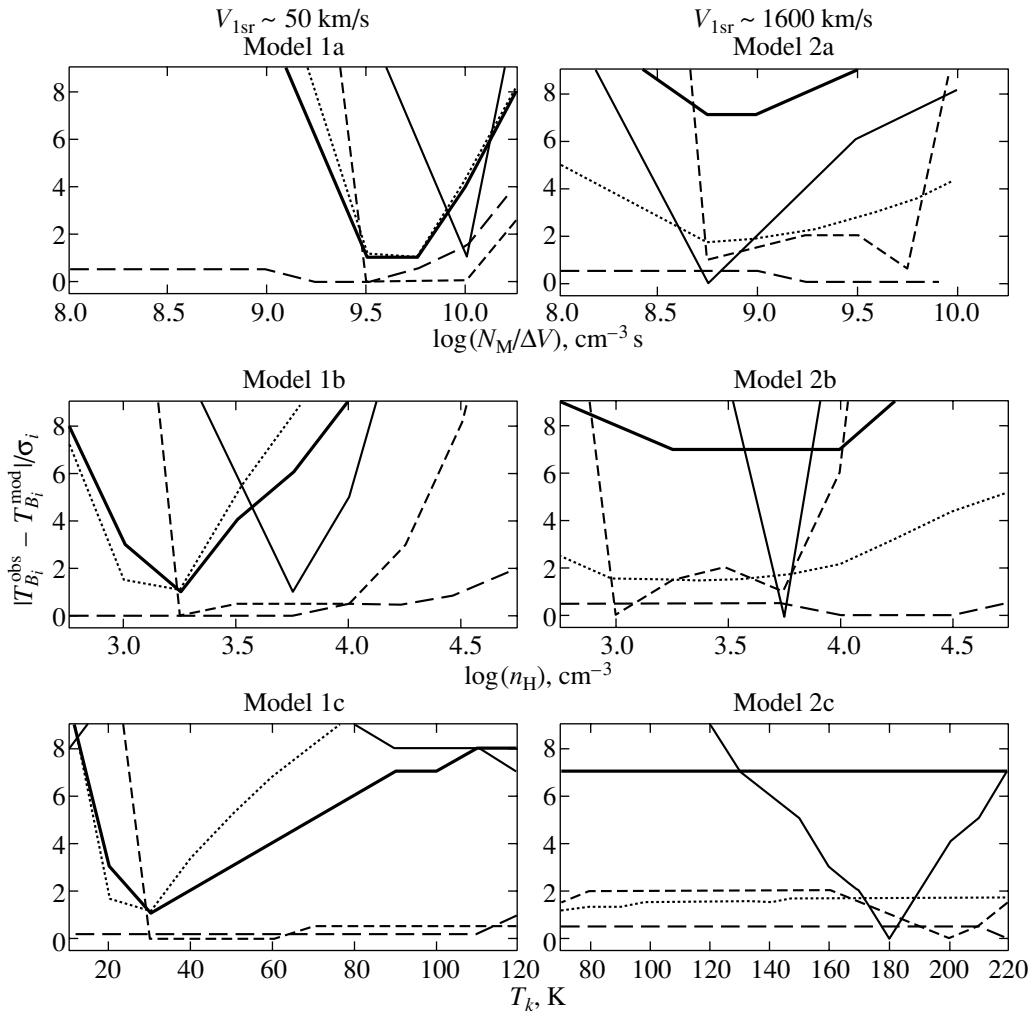
Fig. 8. Deviations of the calculated brightness temperatures $T_{B_i}^{mod}$ of individual lines from the observed values $T_{B_i}^{obs}$, normalized to the observed noise level σ_i for a series of models of the extended cloud ($V_{lsr} \sim 50$ km/s) and high-velocity clump ($V_{lsr} \sim 160$ km/s). Fixed parameters in the models are (1a) $\log(n_H[cm^{-3}]) = 3.25$, $T_k = 30$ K; (1b) $\log(N_M/\Delta V_H[cm^{-3}s]) = 9.5$, $T_k = 30$ K; (1c) $\log(n_H[cm^{-3}]) = 3.25$, $\log(N_M/\Delta V_H[cm^{-3}s]) = 9.5$; (2a) $\log(n_H[cm^{-3}]) = 3.75$, $T_k = 180$ K; (2b) $\log(N_M/\Delta V_H[cm^{-3}s]) = 8.75$, $T_k = 180$ K; (2c) $\log(n_H[cm^{-3}]) = 3.75$, $\log(N_M/\Delta V_H[cm^{-3}s]) = 8.75$. Shown are results for the 2_1-1_1 E line (long dashed curve), 2_K-1_K blend (short dashed curve), 2_0-3_{-1} E line (dotted curve), J_0-J_{-1} blend (thin solid curve), and 2_1-3_0 A^+ line (bold solid curve).

temperatures derived are in satisfactory agreement with the estimated rotational temperature for the NH$_3$ levels [2].

Figure 8 shows the deviations of the calculated brightness temperatures of individual lines from the observed temperatures as functions of one of the model parameters for a number of models. The other two parameters correspond to the reference model, for which we have adopted the model with the minimum χ^2. The left and right columns present the dependences for the extended cloud ($V_{lsr} \sim 50$ km/s) and high-velocity clump ($V_{lsr} \sim 160$ km/s). Note that, in the model with minimum χ^2, both for the extended cloud and the high-velocity clump, not all the lines

show their minimum deviations between calculated and observed brightness temperatures. If we choose different values for the parameters of the reference model, the positions and magnitudes of the minima of the deviations for individual lines change appreciably. However, the approximations in the minimum χ^2 model are satisfactory, since the model intensities for both the extended cloud and high-velocity clump differ from the observed intensities by less than 3σ for virtually all the lines. The only exception is the 2_1-3_0 A^+ line, for which a good fit is obtained with a significantly different set of parameters.

These results suggest that we observe relatively low-density clouds ($< 10^4$ cm^{-3}) in G1.6, and the

cloud material is considerably inhomogeneous. A more accurate approximation of the observed line brightnesses would be obtained in a model taking into account the structure of the object. The realization of such a model requires observations with higher spatial resolution.

5. CONCLUSION

We have presented observations of the molecular cloud G1.6−0.025 in the CH_3OH 2_K-1_K and CH_3OH $J_0-J_{-1}E$ line series and the CH_3OH $5_{-1}-4_0E$, SiO (2−1), SiO (3−2), and HNCO $7_{-7}-6_{-6}$ lines.

Analysis of the CH_3OH, SiO, and HNCO spectra shows that their line profiles contain components corresponding to an extended cloud with $V_{lsr} \sim 50$ km/s that is $> 12' \times 8'$ in size, as well as to smaller clouds: a previously observed high-velocity clump with $V_{lsr} \sim 160$ km/s and a size of $\sim 8' \times 5'$ and a newly detected clump with $V_{lsr} \sim 0$ km/s and a size of $\sim 2'$.

Non-LTE modeling of the methanol emission toward $(0'', 0'')$ shows that both the extended cloud and high-velocity clump have a relatively low hydrogen density $< 10^4$ cm^{-3}. The specific column density of methanol is $\geq 6 \times 10^8$ cm^{-3}s in the extended cloud and $(4 \times 10^8 - 6 \times 10^9)$ cm^{-3}s in the high-velocity clump. The kinetic temperatures of the extended cloud and high-velocity clump are < 80 K and $150-200$ K, respectively.

Three peaks of the integrated intensity arranged in a line (the clump axis) can be distinguished in the maps of the high-velocity clump emission. The radial velocities of the lines toward the peaks are similar and lie in the range $150-170$ km/s. One of the peaks is located at $(0'', 0'')$ and coincides with the peaks in the previous observations of the CH_3OH $4_{-1}-3_0E$ [8] and CH_3OH $2_0-3_{-1}E$ [7] lines. We have detected the emission peak at $(300'', -120'')$ for the first time.

The emission of the extended cloud is distributed nonuniformly: three peaks of the integrated intensity that coincide with the previously observed maxima of the CH_3OH $4_{-1}-3_0$ line [8] can be distinguished. We have identified the emission that comes from a probable compact maser source in the CH_3OH $5_{-1}-4_0$ line. Its position coincides with the boundary of the high-velocity clump. An additional component with $V_{lsr} \sim 43$ km/s is distinguished in the profiles of all the observed lines. The peak emission of this component is extended perpendicular to the axis of the high-velocity clump and coincides with the NH$_3$ maser and a probable star-forming region. Emission from 40 to 160 km/s is observed in the northwest part of the extended cloud, suggesting a connection between this cloud and the high-velocity clump.

A component with $V_{lsr} \sim 0$ km/s has been detected for the first time. The peak of the component's integrated emission lies on the axis of the high-velocity clump. In a number of the spectra, there is emission in the interval from -10 to 75 km/s, indicating a probable genetic connection between the clump with $V_{lsr} \sim 0$ km/s and the extended cloud.

The available observational data suggest complex mechanisms for the interaction of the extended cloud and compact clumps with $V_{lsr} \sim 160$ km/s, ~ 0 km/s and ~ 43 km/s. In particular, the presence of methanol and ammonia masers in directions close to the compact clumps favors the hypothesis of interacting molecular clouds. Let us mention two possible scenarios that could lead to the appearance of cloudy clumps moving with large relative velocities in G1.6.

(1) Collisions of low-density ($n_H < 10^4$ cm^{-3}) objects, for example, between the relatively compact ($\sim 8' \times 5'$), high-velocity ($V_{lsr} \sim 160$ km/s) clump and the extended ($> 12' \times 8'$) cloud. The relative velocity of the collision is of the order of 100 km/s. The spectra with emission extending from 40 to 160 km/s suggest we are observing the initial stage of the collision process. The complex dynamical processes arising during powerful cloud collisions can result in the appearance of components with velocities considerably differing from those of the colliding clouds (see, for example, [27, 28]). The components with $V_{lsr} \sim 0$ km/s and ~ 43 km/s could have such an origin.

(2) The extended cloud, high-velocity clump, and clump with $V_{lsr} \sim 0$ km/s are parts of the same cloud subject to the effect of a nonuniform stellar wind. The source of this wind could be the probable young stellar cluster—the infrared source with Galactic coordinates $l = 1.57°$ and $b = -0.38°$ [29], $\sim 26'$ southeast from G1.6 along the axis of the high-velocity clump. The nonuniformity of the stellar wind could be due to the inhomogeneity of the medium through which it is propagating and with which it is interacting.

To elucidate the nature of processes taking place in G1.6, additional observations with higher spatial resolution are required: mapping in lines tracing high-density material (HNCO, CS, etc.) and in lines tracing high-velocity outflows (H$_2$, CO isotopes, etc.).

ACKNOWLEDGMENTS

REFERENCES

1. J. B. Whiteoak and F. F. Gardner, Mon. Not. R. Astron. Soc. **188**, 445 (1979).
2. F. F. Gardner, J. B. Whiteoak, J. R. Forster, *et al.*, Proc. Astron. Soc. Aust. **6**, 176 (1985).
3. F. F. Gardner and F. Boes, Proc. Astron. Soc. Aust. **7**, 185 (1987).
4. J. Bally, A. A. Stark, R. W. Wilson, and C. Hencel, Astrophys. J., Suppl. Ser. **65**, 13 (1987).
5. M. Tsuboi, T. Handa, and N. Ukita, Astrophys. J., Suppl. Ser. **120** (1), 1 (1999).
6. C. W. Lee, Astrophys. J., Suppl. Ser. **105**, 129 (1996).
7. J. B. Whiteoak and R.-S. Peng, Mon. Not. R. Astron. Soc. **239**, 677 (1989).
8. A. D. Haschick and W. A. Baan, Astrophys. J. **410**, 663 (1993).
9. G. Dahmen, S. Huttemeister, and W. L. Duschl, *The Central Regions of the Galaxies (IAU Symp. 184)*, p. 95.
10. S. Pak, D. T. Jaffe, and L. D. Keller, Astrophys. J. Lett. **457**, L43 (1996).
11. S. Pak, private communication.
12. I. I. Berulis, S. V. Kalenski, A. M. Sobolev, and V. S. Strelnitski, Astron. Astrophys. Trans. **1**, 231 (1992).
13. A. M. Sobolev, Astron. Zh. **69** (6), 1148 (1992) [Sov. Astron. **36**, 590 (1992)].
14. S. Saito, H. Mikami, S. Yamamoto, *et al.*, Astron. Soc. Pac. Conf. Ser. **59**, 241 (1994).
15. T. W. Hartquist, K. M. Menten, S. Lepp, and A. Dalgarno, Mon. Not. R. Astron. Soc. **272** (1), 184 (1995).
16. Y-J. Kuan and L. E. Snyder, Astrophys. J. **470**, 981 (1996).
17. P. Schilke, C. M. Walmsley, G. Pineau des Forêts, and D. R. Flower, Astron. Astrophys. **321**, 293 (1997).
18. P. Caselli, T. W. Hartquist, and O. Havnes, Astron. Astrophys. **322**, 296 (1997).
19. V. I. Slysh, S. V. Kalenski, and I. E. Val'tts, Astrophys. J. **442** (2), 668 (1995).
20. J. L. Caswell, Yi. Jiyune, R. S. Booth, and D. M. Cragg, Mon. Not. R. Astron. Soc. **313** (3), 599 (2000).
21. W. Batrla and K. M. Menten, Astrophys. J. Lett. **329** (1), L117 (1988).
22. A. M. Sobolev, Astron. Tsirk., No. 1543, 7 (1990).
23. S. V. Kalenskiĭ, V. I. Slysh, I. E. Val'tts, *et al.*, Astron. Zh. **78**, 31 (2001) [Astron. Rep. **45**, 26 (2001)].
24. R. Mauersberger, C. Henkel, T. L. Wilson, and C. M. Walmsley, Astron. Astrophys. **162**, 199 (1986).
25. Y. Cao, S. Therebey, T. A. Prince, and C. A. Beichman, http://irsa.ipac.caltech.edu/applications/IGA/ (1997).
26. R. Cesaroni and C. M. Walmsley, Astron. Astrophys. **241** (2), 537 (1991).
27. P. A. Voinovich and A. D. Chernin, Pis'ma Astron. Zh. **21** (6), 926 (1995) [Astron. Lett. **21**, 835 (1995)].
28. A. D. Chernin, New Astron. **5** (6), 327 (2000).
29. C. M. Durtra and E. Bica, Astron. Astrophys. **359**, L9 (2000).

Translated by G. Rudnitskiĭ

Methanol and H₂O Masers in a Disk around GL 2789

V. I. Slysh[1], M. A. Voronkov[1], I. E. Val'tts[1], and V. Migenes[2]

[1]*Astro Space Center, Lebedev Physical Institute, Profsoyuznaya ul. 84/32, Moscow, 117997 Russia*
[2]*Departamento de Astronomía, Universidad de Guanjuato, Guanjuato, Mexico*
Received March 20, 2002; in final form, May 23, 2002

Abstract—VLBA and EVN radio observations of H₂O masers at 22 GHz and methanol masers at 6.67 GHz have been used to obtain images of the maser spots in the infrared object GL 2789, which is associated with the young stellar object V645 Cyg. The position of these masers coincides with that of the optical object to within $0\overset{''}{.}2$. The maser spots are located in a line oriented north–south, and their positions and radial velocities can be described by a model with a Keplerian disk with maximum radius 40 AU for the H₂O masers and 800 AU for the methanol masers. The H₂O and methanol masers spots are unresolved, and the lower limits for their brightness temperatures are 2×10^{13} K and 1.4×10^9 K, respectively. A model in which the maser radiation is formed in extended water–methanol clouds associated with ice planets forming around the young star is proposed. © *2002 MAIK "Nauka/Interperiodica"*.

1. INTRODUCTION

GL 2789 is an infrared source that coincides with an optical reflection nebula and the star-like object V645 Cyg [1]. The optical image contains the star-like condensation N0 and several filamentary nebulae, the brightest of which is called N1. Cohen [1] suggests that this object is associated with a young O7 star at a distance of 6 kpc that is surrounded by a bipolar nebula. Humphreys *et al.* [2] concluded that the optical spectrum of the nebulosity around V645 Cyg corresponded to that of an A star surrounded by a shell, and estimated a smaller distance to the object of about 3.5 kpc (see also Goodrich [3]). In both cases, the mass of the star was estimated to be 10 $M_\odot$. V645 Cyg is located at the center of a molecular cloud that emits CO and NH₃ lines, with the CO line emission showing signs of a bipolar outflow [4, 5]. The optical object V645 Cyg is also located at the center of a source of thermal radio continuum emission about 7″ in size [6]. Lada *et al.* [7] discovered H₂O masers with radial velocities of −48.9 km/s and −44.5 km/s, whose position was determined with an accuracy of $0\overset{''}{.}2$ and coincides with the position of the optical component N0. The VLA observations of Tofani *et al.* [8] obtained 13 years later showed H₂O masers with radial velocities of −43.3 km/s and −41.0 km/s at the same position. OH maser emission at 1665 MHz at radial velocities ranging from −45 km/s to −41.6 km/s was detected by Morris and Kazés [9]. Slysh *et al.* [10] detected a class II maser in the 5_1−6_0A^+ methanol line at 6.7 GHz at radial velocities from −43.5 km/s to −40.5 km/s. Since maser emission is associated

with early stages of stellar evolution, the presence of OH, H₂O, and methonol masers suggests that V645 Cyg is a protostar or young stellar object. Investigations of the fine structure of the maser sources could shed light on mechanisms for interactions between the young star or protostar and its surrounding medium. Here, we present the results of high-angular-resolution (milliarcsecond-scale) studies of the structure of the H₂O and methanol masers associated with this source.

2. OBSERVATIONS

The H₂O-maser observations of GL 2789 were carried out at 22 GHz on the VLBA on June 5, 1996 as part of a prelaunch survey for the VSOP space-VLBI project [11]. The VLBA consists of ten 25-m radio telescopes located at various points on US territory, and provides a maximum baseline length of about 8000 km. The observations were conducted in a snapshot mode with the individual scans being five minutes in duration. The resulting synthesized beam was 0.3×0.95 mas. The total recorded bandwidth of 8 MHz was divided into 512 spectral channels during the correlation of the data, providing a spectral resolution of 15.6 kHz per channel or 0.21 km/s. The sensitivity achieved during the five-minute accumulation time was 100 mJy/beam. The delay and bandpass calibration was performed using observations of the continuum sources 3C 273 and 3C 84. The post-correlation reduction included amplitude calibration and fringe fitting. The fringe fitting was carried out in two stages: (1) the residual delays for the radio telescopes were determined using the continuum sources
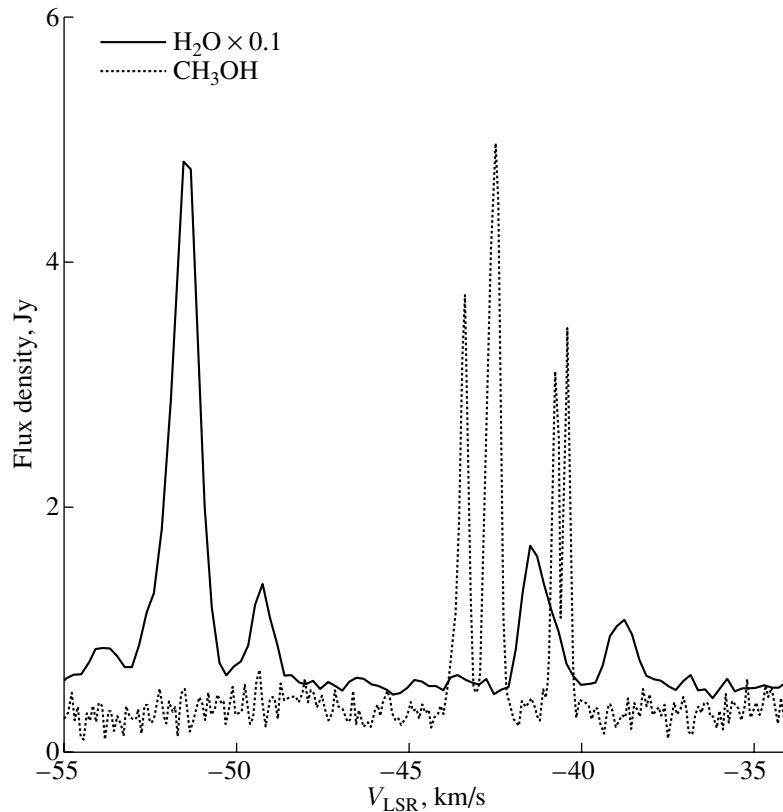
Fig. 1. Water vapor (solid) and methanol (dotted) maser spectra of GL 2789. The CH_3OH maser spectrum was constructed from observations obtained in 1998. The flux density of the H_2O maser has been decreased by a factor of ten.

and (2) the residual fringe rate was determined for each of the sources individually using its strongest spectral features. We also applied a correction for the Doppler shift of each telescope.

Observations of the class II methonol maser in the $5_1-6_0 A^+$ transition were carried out at 6.7 GHz on the European VLBI network (EVN) in 1998 and 2000. Five telescopes equiped with 6.7-GHz receivers participated: the 100 m Effelsberg, 25 m Jodrell Bank, 32 m Medicina (in the 2000 session, the Hoto 32-m antenna was used in place of this antenna) 25 m Onsala, and 32 m Torun antennas. In 1998 and 2000, GL 2789 was observed during four and three 10-min scans, respectively. The resulting synthesized beams were 4.3×8.2 mas. The recorded bandwidth of 2 MHz was divided into 1024 spectral channels, providing a spectral resolution of 1.95 kHz or 0.088 km/s. The sensitivity of the observations was 400 mJy/beam. The delay and bandpass calibration was conducted using observations of several continuum sources. The post-correlation reduction of the methanol observations was carried out in the same way as the reduction of the H_2O-maser data.

The subsequent processing of the data consisted of determining the absolute coordinates of the masers

and the relative positions of the maser spots, and constructing images of the spots themselves. This was carried out in the AIPS package.

3. RESULTS

3.1. Spectra

Figure 1 presents the spectra of the H_2O (solid) and methonol (dotted) masers observed in 1998. Each spectrum contains four features, however the H_2O maser occupies a broader velocity interval than the methanol maser. The entire methanol spectrum is located in the red half of the H_2O radial-velocity spectrum. No methanol maser feature coincides in radial velocity with any of the H_2O maser features. A comparison with the earlier observations of Lada *et al*. [7] and Tofani *et al*. [8] shows that the H_2O spectra experienced substantial variations. In 1998, the brightest feature had a radial velocity of -51.5 km/s, while the brightest features in 1979 [7] and 1992 [8] had radial velocities of -50.2 km/s and -43.3 km/s, respectively. Features at radial velocities of -39 km/s and -41.5 km/s have also appeared. The methanol maser spectrum for the 1998 EVN observations differs markedly from a spectrum observed at
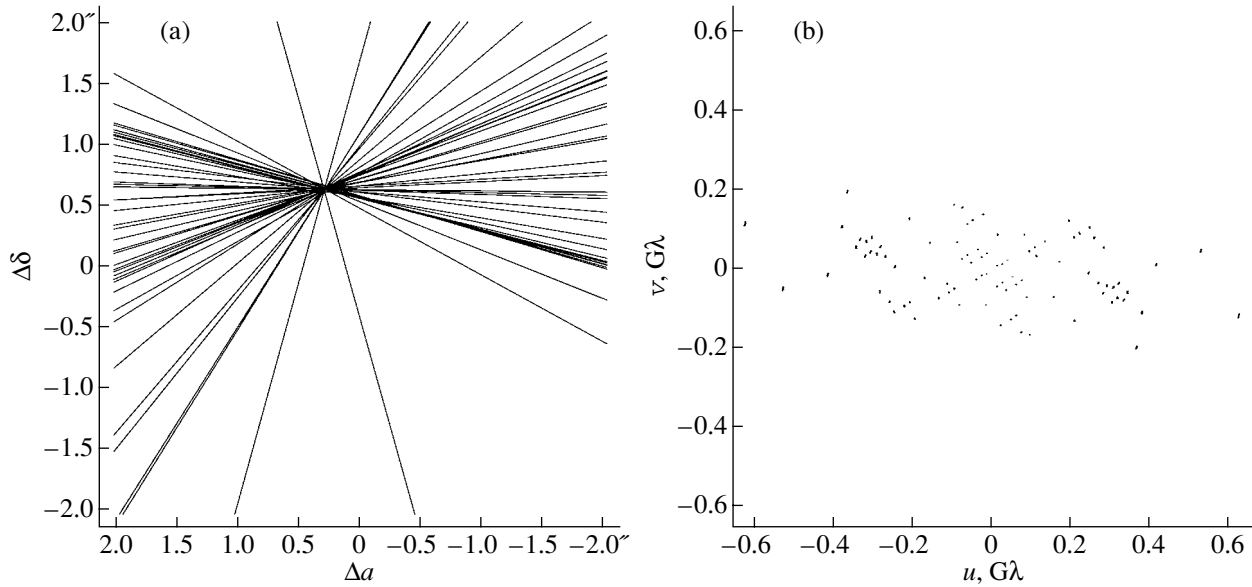
Fig. 2. (a) Determination of the absolute coordinates of the H_2O maser ($v = -51.8$ km/s). The shift of the intersection point from the phase center (0,0) is $\Delta\alpha = 293.9 \pm 11.6$ mas, $\Delta\delta = 650.8 \pm 3.7$ mas and corresponds to the difference between the true maser coordinates at epoch and the coordinates used during correlation. (b) uv coverage for the observations of the H_2O maser in GL 2789.

Medicina in 1995 but nearly coincides with the spectrum obtained by Szymczak *et al*. [12] in 1999. While the brightest feature in 1995 had a radial velocity of -43.6 km/s and a flux of 19 Jy, the brightest features in 1998, 1999, and 2000 were at radial velocities of -42.5 km/s (flux 7.5 Jy), -40.9 km/s (flux 7 Jy), and -40.4 km/s (flux 27 Jy), respectively. At the same time, the character of the spectrum remained nearly unchanged, always containing the same four features, with only their relative fluxes varying.

3.2. Absolute coordinates

We determined the absolute coordinates of the masers using the method of fringe-rate mapping. Figure 2a shows the result of measuring the absolute coordinates of the H_2O feature at -51.8 km/s. Each line corresponds to the locus of possible source positions for which the fringe rate for one of the VLBA baselines is equal to the measured value. The number of lines is equal to the number of baselines (the number of pairs of antennas). Since the VLBA consists of ten antennas, the number of baselines is 45. The point of intersection of all the lines corresponds to the true position of the source. The accuracy of the absolute coordinates of H_2O masers obtained in this way varies from fractions of an arcsecond to several milliarcseconds. The coordinates of the methanol masers were determined in the same fashion.

Table 1 presents the coordinates of the brightest maser features. The table presents the coordinates

obtained from both our 1998 and 2000 methanol observations, which agree within their errors ($< 2\sigma$). The coordinates of the H_2O maser coincide with those presented by Lada *et al*. [7] and Tofani *et al*. [8] within their errors, although they correspond to different spectral features. The accuracy for the H_2O maser coordinates provided by our observations was more than an order of magnitude higher than for the observations of Lada *et al*. [7] and Tofani *et al*. [8]. The methanol maser is shifted relative to the H_2O maser by $0\rlap{.}''08 \pm 0\rlap{.}''07$ to the east and $0\rlap{.}''09 \pm 0\rlap{.}''05$ to the south. The coordinates of both masers coincide with those for the optical object N0 and the source of continuum radio emission, which are known with much lower accuracy. Nevertheless, we can assert with certainty that the masers are located within the extended continuum radio source, which has a diameter of $7''$.

3.3. The Images

3.3.1. The H_2O maser. To construct the image of the H_2O maser, we performed self-calibration of the VLBA data using the strongest spectral feature, at a radial velocity of -51.8 km/s. We were not able to calibrate using external sources, i.e., strong point-like continuum sources, since the amplitude and phase characteristics of the array did not remain sufficiently constant between observations of the calibrator and maser sources, due to changing conditions in the atmosphere. During the self-calibration on a maser

Table 1. Coordinates of the brightest H_2O and CH_3OH maser features in GL 2789

Measurement	α_{2000}	δ_{2000}	Reference
Optical, N0	$21^h39^m58^s27 \pm 0^s03$	$50°14'20''.9 \pm 0''.2$	Cohen [1]
Radio, 3.6 and 6 cm, VLA	21 39 58.26 ± 0.05	50 14 21.3 ± 0.5	Skinner *et al.* [6]
H_2O maser, VLA (-43.3 km/s)	21 39 58.27 ± 0.01	50 14 21.0 ± 0.1	Tofani *et al.* [8]
H_2O maser, VLBI (-50.2 km/s)	21 39 58.28 ± 0.03	50 14 21.0 ± 0.2	Lada *et al.* [7]
H_2O maser, VLBA (-51.8 km/s)	21 39 58.277 ± 0.001	50 14 21.041 ± 0.005	Current paper
Methanol, EVN 1998 (-42.5 km/s)	21 39 58.286 ± 0.006	50 14 20.98 ± 0.05	Current paper
Methanol, EVN 2000 (-42.5 km/s)	21 39 58.286 ± 0.005	50 14 20.6 ± 0.2	Current paper

feature, the amplitude and phase characteristics of the antennas were determined simultaneously with the image of the maser itself, and variations in these characteristics and in the atmospheric characteristics were removed from the data.

Figure 2b shows the coverage of the *uv* plane for the observations of GL 2789. Since each of the individual observations was short (5 min), the tracks corresponding to individual pairs of antennas are represented by short segments of ellipses that appear nearly like dots. We can see that the range for *u* (horizontal direction) is appreciably larger than the range for *v* (vertical direction). This is due to the locations of the antennas in the VLBA, whose extent in the east–west direction is somewhat larger than in the north–south direction. As a result, the synthesized beam has an elliptical shape with a 3 : 1 axial ratio.

The self-calibration procedure yielded an image of the reference feature at -51.8 km/s, as well as images of all the remaining features with radial velocities from -38.0 km/s to -55 km/s. The maser spots are concentrated primarily in two groups. The southern group contains features with radial velocities from -49 km/s to -55 km/s, while radial velocities in the northern group are from -38 km/s to -42 km/s. Figures 3 and 4 present images of the maser spots of the northern and southern groups in all channels where there was an appreciable signal. These images are super-resolved; i.e., the images were convolved with a beam 0.1 mas in size. This is admissible in the presence of high signal to noise. A map of the masers in the southern group constructed for all the channels is shown in Fig. 5a, an analogous map for the northern group is shown in Fig. 5b, and a combined map is shown in Fig. 5c. We can see that the southern group of maser spots forms a structure that is elongated in the east–west direction, while the northern group is elongated roughly north–south. Within the northern group, the radial velocity decreases from south to north, contrary to the general tendency for the radial

velocity for the maser as a whole to grow from south to north. One weak feature with a radial velocity of -50.5 km/s has a peculiar location, separated from the southern group by about 5.6 mas to the southwest. In all, we detected eight maser spots in the image of GL 2789. Their mutual locations relative to the reference feature at -51.8 km/s are presented in Table 2 and shown in Fig. 5d. This maser source was the most compact of all those observed during the survey: the maximum distance between individual features does not exceed 10 mas.

The spots themselves are very compact, and are not resolved even on the longest VLBA baselines. Figure 6 shows the dependence of the correlated flux on the baseline length for one of the spots. We can see that the correlated flux is nearly independent of the baseline length, indicating that this maser spot is not resolved by any of the baselines. The remaining spots are also unresolved. The upper limit to their angular size is 0.05 mas (or 50 μarcsec), and the corresponding lower limit to their brigthness temperature is 2×10^{13} K.

3.3.2. The Methanol maser. The mapping of the methanol maser was carried out in the same way as for the H_2O maser. The four spectral features visible in Fig. 1 correspond to four maser spots (Table 3), as we can see in Fig. 7a, which presents the image made from the 1998 data. The spots are located roughly along a north–south line and form two groups of two spots. The distance between the groups is about 100 mas, and the radial velocity of the southern group is 2.5 km/s higher than that of the northern group. As for the H_2O maser spots, the spots themselves are not resolved; their sizes are less than 2 mas, corresponding to a lower limit for the brightness temperature of 1.4×10^9 K. Figure 7b shows the map of the GL 2789 methanol maser emission obtained using the 2000 data. Since the methanol observations were carried out twice with a time interval of two years, we can estimate possible changes in the relative positions of
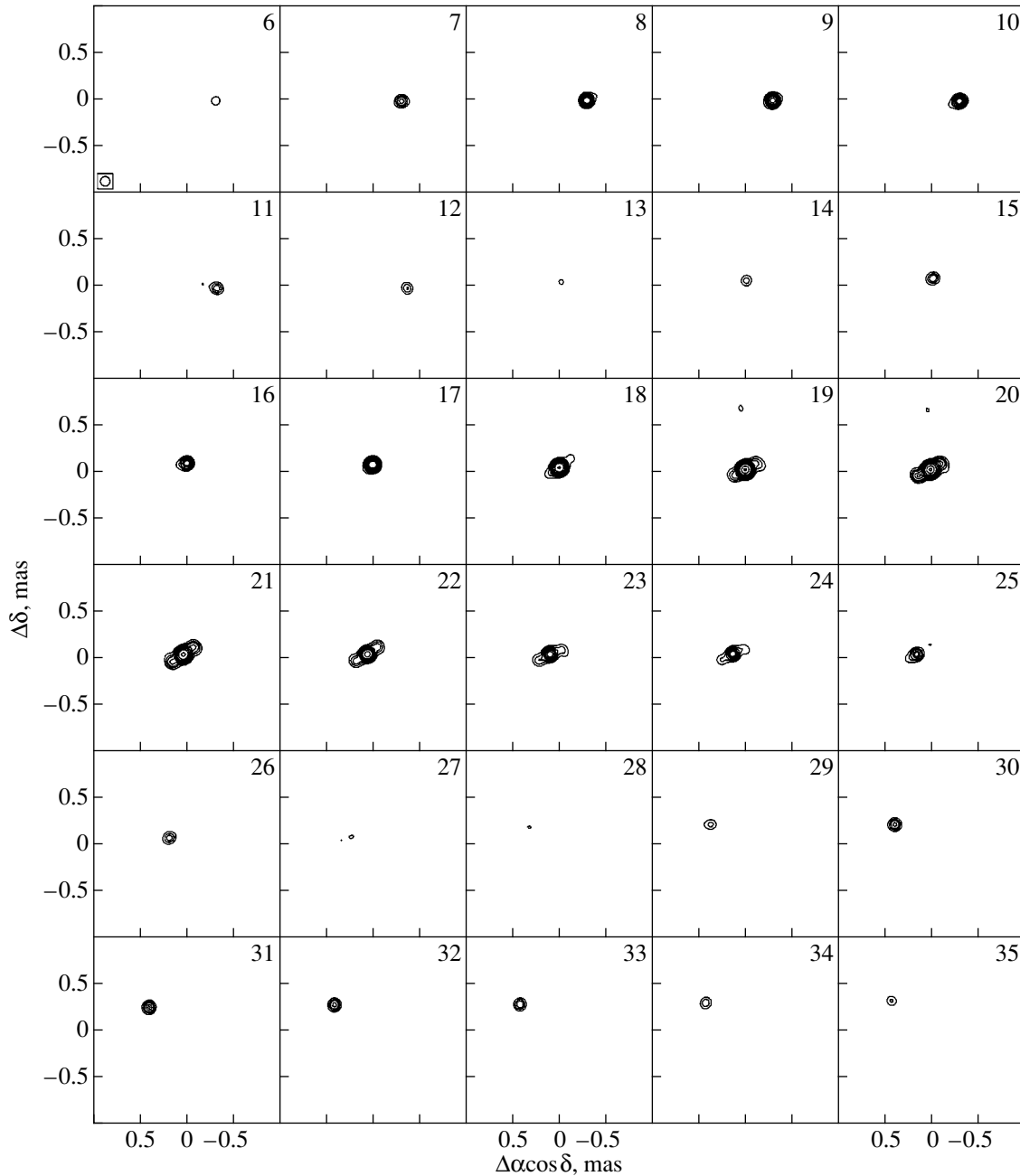
Fig. 3. Images of the southern group of water maser spots in various channels. The contours are drawn at $3.7 \times (0.3, 0.5, 0.7, 1, 1.2, 1.5, 2, 3, 5, 6, 7, 8, 9)$ Jy/beam.

the spots. A comparison of the two images indicates that the distances between the spots did not change significantly, by less than 2 mas, which is within the observational errors. The position of spot B changed by 2.5 mas in the line wings. The intensity and profile of the line corresponding to spot B also varied. These variations may indicate a weakening of the previous spot B and the appearance of another spot near the old position at a slightly different velocity.

4. MODEL FOR THE MASERS

Figure 7c shows the relative positions of the H_2O and methanol masers. In both masers, the spots are distributed roughly along a north–south line, with the center of the methanol maser shifted 90 mas south from the center of the H_2O maser. The accuracy of the position of the methanol maser relative to the water maser is not high, so that it is reasonable to suppose that both masers are located approximately on a north–south line similar to those corresponding
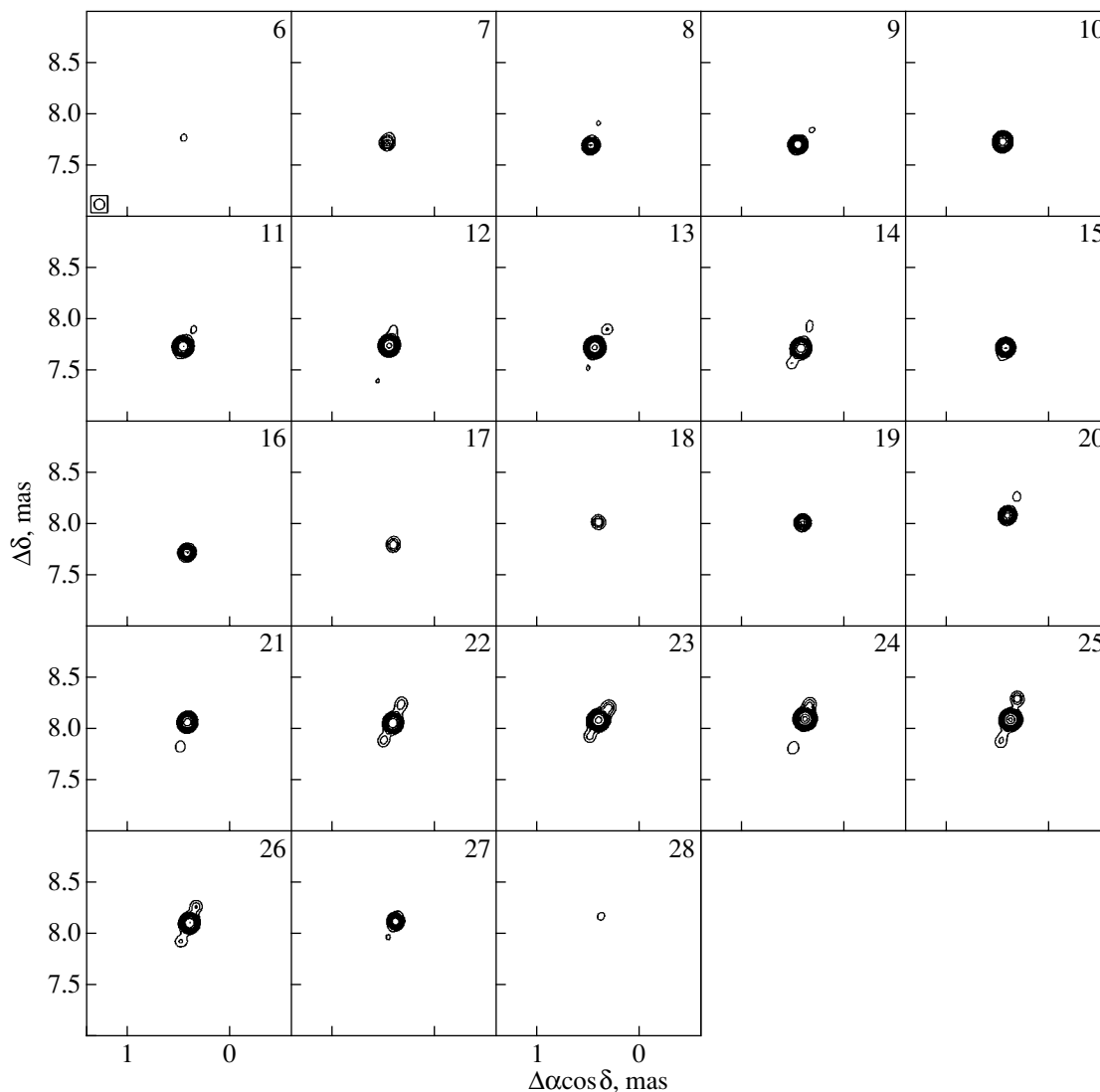
Fig. 4. Images of the southern group of water maser spots in various channels. The contours are drawn at $1.1 \times (0.3, 0.5, 0.7, 1, 1.2, 1.5, 2, 3, 5, 6, 7, 8, 9)$ Jy/beam.

to the structure of the maser spots. The maximum distance between the methanol-maser components is roughly a factor of ten greater than for the H_2O maser, while the difference in radial velocities is about a factor of three smaller. The radial velocity of the molecular cloud associated with GL 2789, -45.6 km/s, is within the interval of velocities for the H_2O maser and at the blue edge of the velocity interval for the methanol maser. The radial-velocity gradients for the methanol and H_2O masers have different signs: while the methanol radial velocity decreases in the direction of the H_2O maser, from south to north, the H_2O radial velocity increases from south to north.

The variations of the radial velocity in the north–south direction are shown in Fig. 7d. These properties can be explained using a model in which the masers lie in a Keplerian disk viewed nearly edge-on rotating

around the supposed central star. The position of the star, which may correspond to the optical object N0, is not known with sufficient accuracy to establish the parameters of the Keplerian orbit. As we can see from Table 1, both masers coincide with the object N0 to within the accuracy of its coordinates, $0''.2$. From general considerations, it seems likely that the H_2O masers are closer to the star than the methanol maser. This is supported by their large radial-velocity dispersion, consistent with the idea that the H_2O masers move in Keplerian orbits at closer distances to the star, and the smaller linear scale of the H_2O maser source, about 50 AU (while the size of the region of methanol-maser emission is of the order of 600 AU). In addition, the H_2O maser requires a higher gas temperature (300–400 K) and higher den-
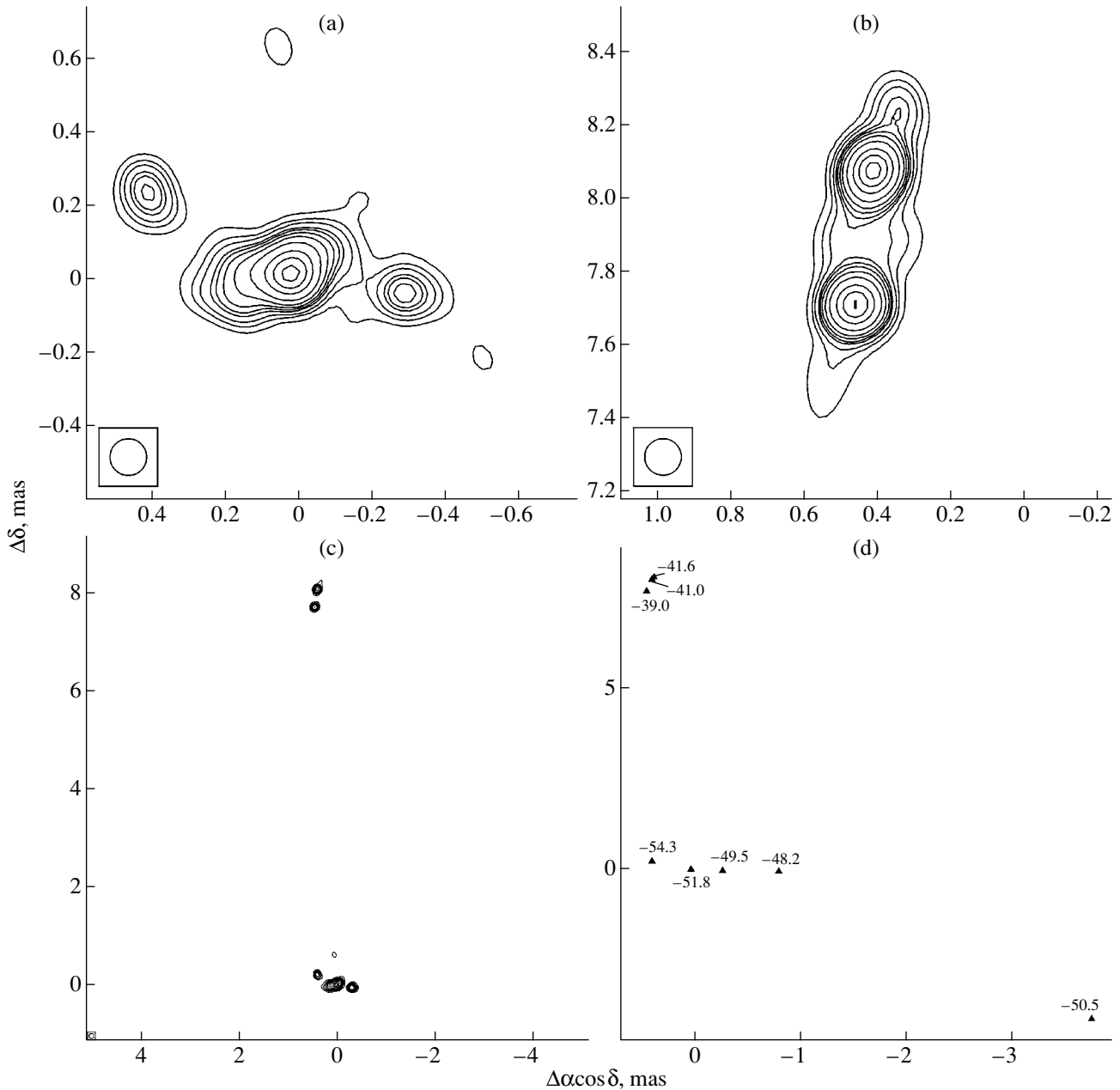
Fig. 5. Summed maps of the H_2O masers of the (a) southern and (b) northern groups. (c) Total map, where the brightness of each point is determined by the maximum of the brightnesses of the maps at that point for all spectral channels. The contours are drawn at 0.03, 0.05, 0.07, 0.1, 0.12, 0.15, 0.2, 0.3, 0.5, 0.6, 0.7, 0.8 and 0.9 of the maximum, which are 3.9 Jy/beam for map (a), 1.9 Jy/beam for map (b), and 3.9 Jy/beam for map (c). (d) Positions of the water maser spots in GL 2789 relative to the reference feature at -51.8 km/s.

sity ($\sim 10^9$ cm^{-3}), while the methanol masers require temperatures not exceeding 100 K and gas densities not exceeding 10^7 cm^{-3}.

It is natural to suppose that the gas temperature and density are higher closer to the star than further from it. The opposite velocity gradients for the H_2O and methanol masers are consistent with a disk model only if the star is located between the north-

ern and southern components of the H_2O maser. In that case, the opposite radial-velocity gradient for the H_2O maser can be explained by the fact that the masers are distributed in the direction toward the star and have radial velocities that are close to the systematic radial velocity of the star. The methanol masers arise in directions tangential to the disk and have radial velocities equal to the velocity of rotation
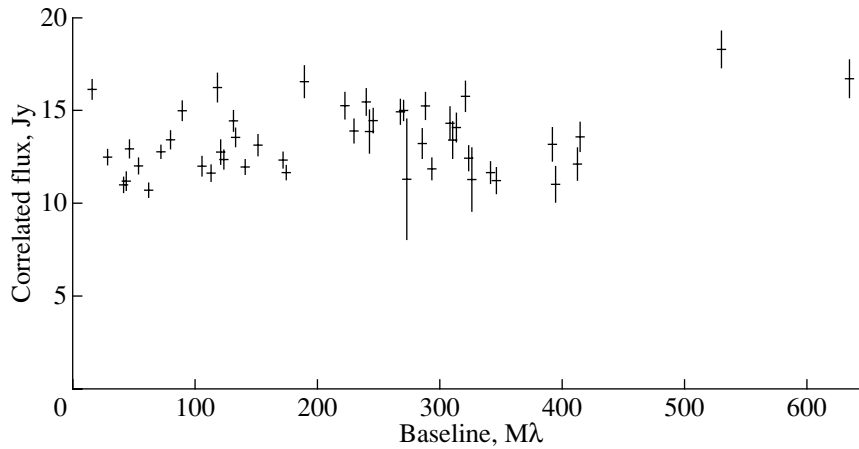
Fig. 6. Dependence of the correlated flux on the baseline length for one of the water-maser spots (the feature at -41.6 km/s).

of the disk at the corresponding distance from the star. In GL 2789, we see only emission from the side of the disk that is moving away from the observer and experiences a red shift. Components arising in regions of the disk that are approaching and have blue shifts are not visible for some reason, possibly due to differences in the pumping conditions.

Figure 8 shows a schematic of the disk and the distribution of the masers and star. In this model, if the mass of the star is 10 $M_\odot$, the H_2O masers are located at a distance $R = 41.1$ AU, while the methanol masers are at distances between 200 AU and 800 AU, for the adopted distance to the source of 6 kpc. This follows from the relation for a Keplerian disk [13]

$$\frac{dV}{dx} = 30 \text{ km s}^{-1}\text{AU}^{-1}\sqrt{M/R^3}, \qquad (1)$$

where ΔV is the observed radial-velocity interval ($\Delta V = 17.3$ km/s for the H_2O maser), Δx is the apparent extent of the maser source ($\Delta x = 8$ mas (or

Table 2. Relative positions of the H_2O maser spots

Radial velocity, km/s	$\Delta\alpha\cos\delta$, mas	$\Delta\delta$, mas	Flux, Jy
-54.3	0.40	0.22	4.7
-51.8	0.03	0.00	36.0
-50.5	-3.76	-4.16	1.8
-49.5	-0.27	-0.04	10.0
-48.2	-0.80	-0.06	0.6
-41.6	0.38	8.10	6.6
-41.0	0.40	8.04	6.4
-39.0	0.45	7.71	7.3

48 AU), M is the mass of the star in solar masses, and R is the distance from the star to the H_2O maser in AU. This model is similar to the model for a disk associated with a black hole in the nucleus of the galaxy NGC 4258 [14]. In that case, H_2O masers observed at radial velocities close to the systematic velocity of the galaxy are distributed near the direction toward the center of the disk, with high-velocity features located at tangential points of the disk. In our model, in contrast to the model for NGC 4258, the H_2O masers are observed only in the direction toward the center of the disk, and the role of the high-velocity features is played by the methanol masers, which show only blue features.

The disk model for the H_2O and methanol masers in GL 2789 can be verified if time variations in the radial velocities of the H_2O components can be detected: in the model, the expected acceleration is 1.1 km/s per year, and the proper motion of the H_2O masers spots should be 0.52 mas/yr. Both effects are associated with rotation of the disk, whose linear velocity is 14.8 km/s at a distance of 41.1 AU from a star with a mass of 10 $M_\odot$, where the H_2O masers are located. The acceleration and proper motion of the methanol masers should be small, since they are observed in the tangential direction. The disk model predicts a Keplerian dependence of the radial velocity of the methanol masers on their distance from the star, $V \sim R^{-\frac{1}{2}}$. The results of observations shown in Fig. 7d are consistent with the Keplerian model, although the number of points is too small to draw definitive conclusions. No proper motions of the methanol maser spots relative to the reference feature were detected, as was noted above, and an upper limit to the proper motion of 2 mas over 2 yrs corresponds to an upper limit for the linear velocity of the relative motion of the maser spots of 28.5 km/s. This limit is

Table 3. Relative positions of the CH$_3$OH maser spots. The positions are given relative to the reference water-maser spot at -51.8 km/s. This shift was determined from the absolute-coordinate measurements and has an accuracy of about 50 mas. The accuracy of the relative coordinates of the spots for lines emitted by a single molecule is about 1 mas

Spectral feature	Radial velocity, km/s	1998 Observations			2000 Observations		
		$\Delta\alpha\cos\delta$, mas	$\Delta\delta$, mas	Flux, Jy	$\Delta\alpha\cos\delta$, mas	$\Delta\delta$, mas	Flux, Jy
A	-43.4	76.0	-45.1	2.0	77.7	-45.4	2.5
B	-42.5	85.0	-65.0	2.5	83.5	-64.4	1.2
B$_1^*$	-42.8	83.7	-63.2	1.0	82.8	-64.7	0.9
C	-40.8	82.9	-134.2	2.0	82.8	-134.5	1.7
D	-40.4	94.2	-143.2	2.2	94.1	-143.3	3.0

* Component corresponds to the wing of the feature at -42.5 km/s.

consistent with the absence of proper motion during tangential motion of the maser spots.

We can also consider other models for the GL 2789 maser sources. Historically, the first models for H$_2$O masers associated with massive stars were expanding-envelope models [15]. This type of model is also of interest for GL 2789, since it is known from optical observations that the star emits a stellar wind with a velocity of more than 600 km/s [1]. However, such high velocities are not observed in the H$_2$O and methanol maser lines. Torrelles *et al.* [16] suggest that H$_2$O masers are associated with one-sided jets ejected by the star. Such a jet is observed in the radio continuum of W75N [16]. However, no jets have been detected in the case of GL 2789; in addition, the radio continuum source is much larger than the maser-emission region [6] and is probably associated with the region of the stellar wind that is traced by the SII optical lines. The dimensions of the region of SII emission and of the region of radio-continuum emission coincide, as do the estimates on the mean density in this zone derived from these observations, on the order of 2×10^4 cm^{-3}. The analysis of the SII line profile performed by Hamann and Persson [17] led them to conclude that, in addition to its stellar wind, V645 Cyg possesses a dense circumstellar disk. This was based on the presence of only blue components in the SII line profile, corresponding to material moving toward the observer. The red wing associated with the stellar-wind material moving away from the observer was absent from the SII spectrum, and Hamann and Persson [17] proposed that the emission in the red wing was screened by the disk. The presence of a disk is also supported by the emission in the KI, FeI, and CaII lines, which arise in comparatively cool material with a density of the order of 10^{10} cm^{-3}.

Figure 6 of [17] shows a model with a disk surrounding the star, together with an extended region of stellar wind radiating in SII and H$_\alpha$ lines. In this model, the H$_2$O and methanol masers could be located in the disk proposed by Hamman and Persson [17]. Since the densities required for the H$_2$O, and especially the methanol, masers are lower than the density of the inner part of the disk derived from optical line data, these masers must be located in a lower-density region of the disk, at larger distances from the star.

In this model, the bipolar flow observed in GL 2789 [4] is emitted perpendicular to the disk and moves away from the star and masers at very large distances or tens of thousands of AU.

5. DISCUSSION

The detection of a class II methanol maser and the demonstration that it is associated with the optical object V645 Cyg, as well as the confirmation of the connection between this object and the H$_2$O maser, provide additional arguments that V645 Cyg is a young stellar object. The source of thermal radio emission surrounding this object is most likely not a classical HII region, and instead a region filled with stellar wind.

Another important characteristic of this young stellar object is the presence of a cool circumstellar disk, in which compact sources of H$_2$O, methanol, and possibly OH maser emission are immersed. In [18], which was dedicated to the methanol masers in W3(OH), it was suggested that individual features in the methanol and OH spectra were generated in extended envelopes surrounding ice planets. It is natural to suppose that such planets are located in a disk and move in Keplerian orbits. The chemical composition of these extended envelopes reflects the composition of the interstellar dust grains, or more precisely of their mantles. It is known that the mantles
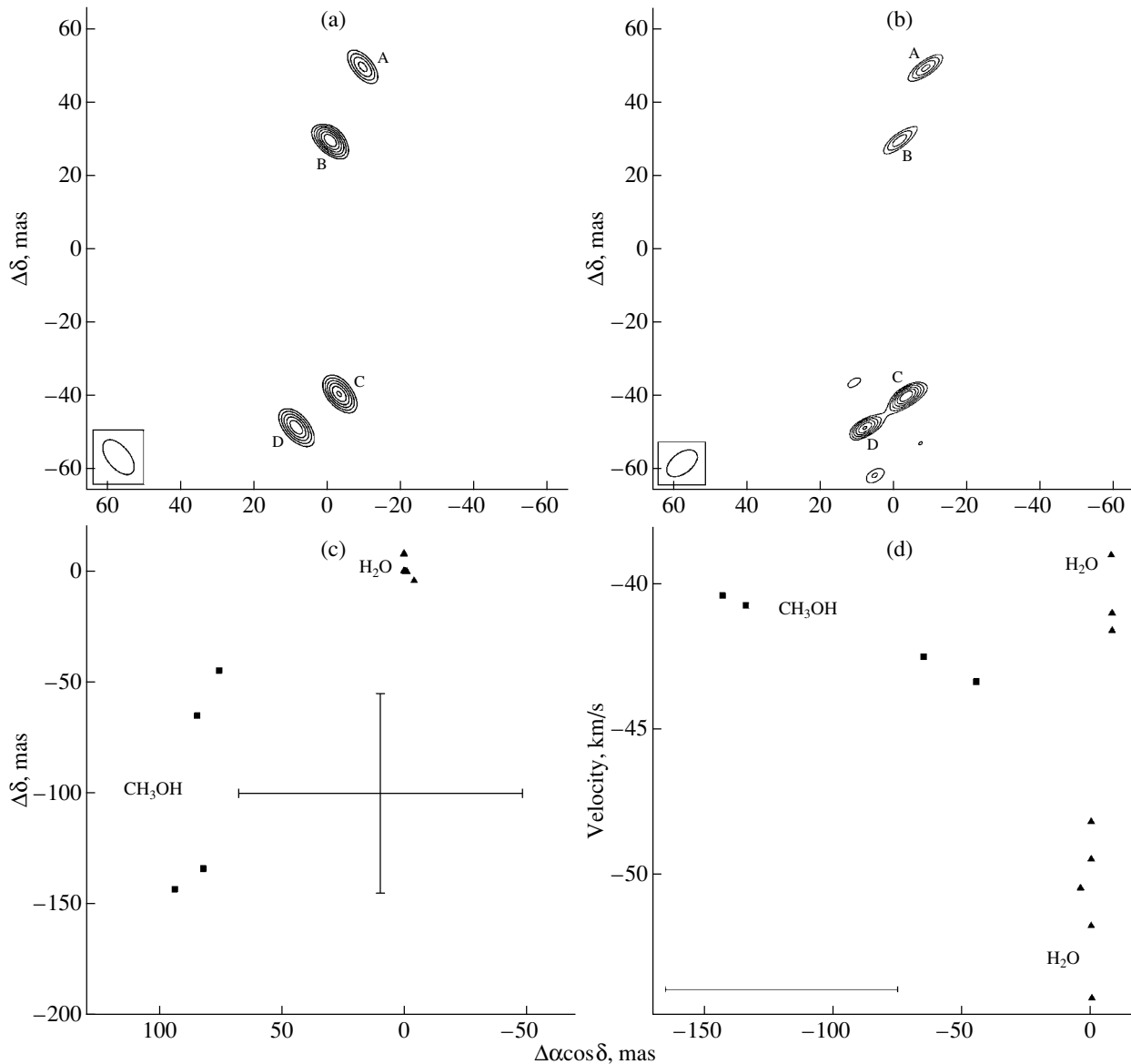
Fig. 7. Map of the methanol maser in GL 2789. (a) 1998 observations with contours at $0.22 \times (4, 5, 6, 7, 8, 9)$ Jy/beam. (b) 2000 observations with contours at $0.35 \times (4, 5, 6, 7, 8, 9)$ Jy/beam. Components A, B, C, and D correspond to spectral features with velocities of -43.4, -42.5, -40.7, and -40.4, respectively. (c) Relative positions of the methanol and water maser spots. The cross shows the error in the relative position of the methanol and water masers. (d) Variations of the radial velocity in the north–south direction. The error in the relative position of H_2O and CH_3OH masers is shown in the lower left corner.

of dust grains consist primarily of ice, and methanol is the second most abundant ice material after water. For example, in the direction toward the high-mass protostars GL7009S and W33A, the abundances of methanol ice relative to water ice are 30% and 5–22% for GL7009S and W33A, respectively [19]. The methanol abundance in the direction of NGC 7538 IRS9 is 25% [20], and is 8.7% in the direction of GL 2136 [21]. In other sources that have been studied, the methanol abundances does not exceed several per cent [19].

In cool disks surrounding protostars and very young stars, dust grains can adhere to larger bodies, ultimately reaching the dimensions of small planets. This is how the objects in Kuiper's belt were formed in the solar system. At sufficiently close distances to the star, water and methanol evaporate from the surfaces of planets and leave the gravitational fields of these planets if their masses are sufficiently low. Envelopes consisting primarily of water and methanol will thus form around these planets, whose extent can be much larger than the dimensions of a planet. This same picture is observed in miniature in our solar system, with cometary nuclei in place of ice planets.

With approach toward the Sun, ice and methanol are evaporated from the surfaces of cometary nuclei, forming extended envelopes.

The water in such envelopes dissociates into atoms of hydrogen and molecules of OH, and conditions favorable for water, OH, and methanol maser emission are created: (a) rather high abundances, reaching 90% for water and OH and about 10% for methanol—much higher than in the interstellar medium; (b) high column densities of water and methanol molecules—10^{16} cm^{-2} for methanol and 10^{18} cm^{-2} for H_2O for an envelope 10^9 cm (10 000 km) in size—required to create high optical depths and, accordingly, high maser amplifications; (c) the required ranges of temperature and density—from 400 K and 10^9 cm^{-3} for the H_2O masers to 100 K and 10^6-10^7 cm^{-3} for the OH and class II methanol masers; (d) intense radiation near the rotational transitions of these molecules (submillimeter wavelengths and the far infrared), provided by reprocessing of the radiation of the young star by the dust.

These conditions are adopted in standard models for maser pumping. It is obvious that comets in the solar system are too small to form such extended dense envelopes; the optical depth in lines of H_2O and methanol is too low, and no maser emission is observed. In GL 2789, the planets responsible for the water-vapor line emission move in Keplerian orbits at a distance from the star of about 40 AU, with each of the eight maser spots (Table 2) corresponding to a separate planet. The OH and methanol masers are located further from the star, at distances of 200–800 AU. At such large distances, the orbits of planets may not be located in a disk, due to possible perturbations in their motions. This could explain the presence of individual maser spots outside the disk.

This simple model can easily be verified using further observations. This requires monitoring of the radial velocities and positions of the maser spots to measure accelerations and linear translations due to the Keplerian motion. The most suitable masers for such observations are the H_2O masers, which should be in the orbits that are closest to the star and move with the highest speeds. The corresponding estimates are presented in the previous section. In the model presented here, the period of revolution of the planets responsible for the H_2O maser emission is about 83 yrs. Therefore, using spectral and angular measurements with sufficiently high accuracy, it should be possible to determine the accelerations and velocities of the maser spots over fairly short time scales, less than one year. Such measurements must be conducted often due to the strong variability of the H_2O maser emission. However, on short time scales, the accuracy of measurements such as proper-motion
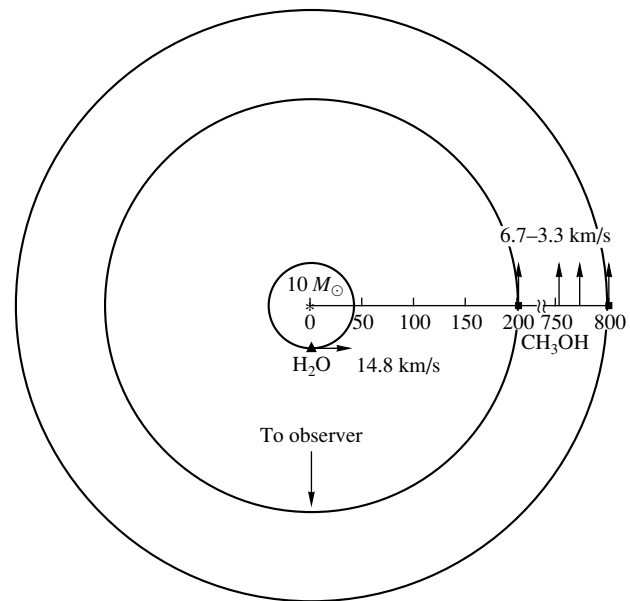
Fig. 8. Schematic of the disk in GL 2789. The numbers show distance from the star in AU, and the arrows show the direction and magnitude of the orbital velocity in km/s for the H_2O and methanol masers.

measurements could prove to be insufficient, even using arrays with the longest possible baselines, such as the VLBA.

One possibility is the use of ground–space interferometers, which can attain angular resolutions exceeding that of ground-based interferometers by a factor of a few, or even an order of magnitude more than this. The measurement of proper motions using ground–space interferometers requires that the masers have sufficiently small angular sizes—smaller than the width of the interferometer fringe. We have shown that the maser spots in GL 2789 are very compact, and are not resolved by the VLBA (Figs. 2b, 6). Therefore, they may be suitable for measurements using a ground–space interferometer. Other models with expanding components or jets predict that the spots should move uniformly and linearly, which could also be verified using observations with very high angular resolution.

6. CONCLUSION

The linear structure of the H_2O and methanol masers is in best agreement with a disk model. If the mass of the star is 10 $M_\odot$ and it is located at a distance of 6 kpc, the H_2O maser components are located about 40 AU from the star, with the methanol masers at distances of 200–800 AU. The physical objects responsible for the emission of individual maser spectral features could be ice planets surrounded by extended water–methanol envelopes moving in Keplerian orbits around the star. Such planets are similar

to the objects of Kuiper's belt in the solar system. This model can be verified using observations with high angular resolution, using either ground-based or ground–space interferometers.

REFERENCES

1. M. Cohen, Astrophys. J. **215**, 533 (1977).
2. R. M. Humphreys, K. M. Merrill, and J. H. Black, Astrophys. J. Lett. **237**, L17 (1980).
3. R. W. Goodrich, Astrophys. J. **311**, 882 (1986).
4. A. Schulz, J. H. Black, C. J. Lada, *et al.*, Astrophys. J. **341**, 288 (1989).
5. J. M. Torrelles, G. Anglada, L. F. Rodríguez, *et al.*, Astron. Astrophys. **177**, 171 (1987).
6. S. L. Skinner, A. Brown, and R. T. Stewart, Astrophys. J., Suppl. Ser. **87**, 217 (1993).
7. C. J. Lada, L. Blitz, M. J. Reid, and J. M. Moran, Astrophys. J. **243**, 769 (1981).
8. G. Tofani, M. Felli, G. B. Taylor, and T. R. Hunter, Astron. Astrophys., Suppl. Ser. **112**, 299 (1995).
9. M. Morris and I. Kazés, Astron. Astrophys. **111**, 239 (1982).
10. V. I. Slysh, I. E. Val'tts, S. V. Kalenskii, *et al.*, Astron. Astrophys., Suppl. Ser. **134**, 115 (1999).
11. V. Migenes, S. Horiuchi, V. I. Slysh, *et al.*, Astrophys. J., Suppl. Ser. **123**, 487 (1999).
12. M. Szymczak, G. Hrynek, and A. J. Kus, Astron. Astrophys., Suppl. Ser. **143**, 269 (2000).
13. V. Minier, R. S. Conway, and R. S. Booth, Astron. Astrophys. **362**, 1093 (2000).
14. M. Miyoshi, J. Moran, J. Herrnstein, *et al.*, Nature **373**, 127 (1995).
15. R. Genzel, D. Downes, J. M. Moran, *et al.*, Astron. Astrophys. **66**, 13 (1978).
16. J. M. Torrelles, J. F. Gomez, L. F. Rodríguez, *et al.*, Astrophys. J. **489**, 744 (1997).
17. F. Hamann and S. E. Persson, Astrophys. J. **339**, 1078 (1989).
18. V. I. Slysh, I. E. Val'tts, S. V. Kalenskiĭ, *et al.*, Astron. Zh. **76**, 751 (1999) [Astron. Rep. **43**, 657 (1999)].
19. E. Dartois, W. Shutte, T. R. Geballe, *et al.*, Astron. Astrophys. **342**, L32 (1999).
20. W. A. Shutte, A. G. G. M. Tielens, D. C. Whittet, *et al.*, Astron. Astrophys. **315**, L333 (1996).
21. C. J. Skinner, A. G. G. M.Tielens, M. J. Barlow, and K. Justtanont, Astrophys. J. Lett. **399**, L79 (1992).

Translated by D. Gabuzda

Optical Features of the Accretion Disk in the HZ Her/Her X-1 System during the Anomalous Low State in 1999

E. K. Sheffer, I. B. Voloshina, V. P. Goransky, and V. M. Lyuty

Sternberg Astronomical Institute, Moscow State University, Universitetskiĭ pr. 13, Moscow, 119992 Russia
Received January 6, 2002; in final form, March 15, 2002

Abstract—We present the results of UBV photoelectric and CCD observations of Her X-1/HZ Her near its primary minimum in 1999, when the object was in an anomalous low X-ray state, together with UBV observations accumulated since 1988. We compare the orbital light curves in the normal and anomalous low state, which differ considerably. The differences can be interpreted as being due to changes in the temperature and size of the hot spot on the stellar surface illuminated by the X-ray pulsar. The observations show that the accretion-disk luminosity was a factor of six to ten lower in 1999 than in the normal state. We used all available photoelectric data to compute the power spectrum in the B band. The only significant peaks are those corresponding to the orbital period and to beating of the orbital period with the periods characterizing gaps in the observations (one year and one day) and with the 35-day period. We conclude that it is impossible to determine the direction of the disk precession from the power spectrum alone. © 2002 MAIK "Nauka/Interperiodica".

1. INTRODUCTION

The low-mass close binary system HZ Her/Her X-1 presents unique possibilities for multi-wavelength astrophysical studies, since we are able to directly observe and study the accretion disk around a neutron star—the X-ray pulsar Her X-1 [1]. The pulsar was discovered in late 1971 by the UHURU X-ray satellite [2]; since then, it has been an object of study for 30 years, especially in the last decade. Soon after its discovery, the pulsar was identified with the variable star HZ Her [3], and extensive optical investigations of the HZ Her/Her X-1 system were initiated.

Subsequent studies showed that one of the system's components was a low-mass optical star with spectral type A7V, whereas the other component, which is orbiting in a circular orbit with a period of 1.7^d, is a neutron star. The main origin of the X-ray orbital variability is eclipses of the neutron star (X-ray source) by the optical star, and the optical variability is due to the star's heating by the X-ray radiation from the pulsar, similar to the reflection effect [4, 5].

One of the system's characteristic features is its 35-day cycle, during which the X-ray flux demonstrates three different states: "main-on," the main state when the X-ray flux is turned on, the "low state," when the X-ray flux is off, and "short-on," a short transition of the X-ray flux to the on state in the middle of the low state. It is generally believed that the origin of the 35-day cycle is the precession of a tilted and twisted gaseous disk around the neutron

star, which periodically blocks the X-ray flux from the observer [6–8]. The X-ray flux during the low state is usually 2–3% of that during the main-on state. Extended intervals in which the X-ray flux of the HZ Her/Her X-1 system was at low levels, called the "anomalous low state" (ALS), were observed in 1983 and 1993 [9, 10]. During these intervals, the X-ray flux dropped still lower (by about a factor of two) than its level in the normal low state. However, there was not a genuine shutdown of the X-ray source, like that of 1949–1955 [11, 12]: the reflection effect in the optical was still present, basically without appreciable distorsions [10, 13, 14]. A similar ALS of the X-ray flux was observed in 1999–2000 [15].

The 35-day X-ray cycle, presumed to be due to precession of the accretion disk, is also clearly reflected in variations in the shape of the orbital light curve in the optical [8, 16]. Since the reflection effect does not disappear during an ALS, this state must somehow be caused by the state of the accretion disk. The eclipsing system HZ Her/Her X-1 provides a unique chance to observe the accretion disk almost directly: at the beginning of the X-ray eclipse (orbital phase 0.93), we see half of the accretion disk plus the unheated side of the optical star and, at the end of the X-ray eclipse, we see the other half of the disk and the star. Since the star is larger than the accretion disk, the disk is completely covered by the star at phases 0.00 ± 0.02. Thus, it is possible to derive the colorimetric characteristics of the optical star and

accretion disk of this binary system from observations around the primary minimum.

Precisely this method was used to derive the mean integrated color characteristics of the accretion disk in the HZ Her/Her X-1 system [17], together with their variations along the disk radius [18]. Sheffer and Lyutiĭ [18] found that the color indices of the outer regions of the disk were very different when entering and emerging from eclipse, which can readily be explained by models in which the accretion disk is twisted and there is significant curvature of its outer edge due to the disk's precessional motion.

In the present study, we analyze a large amount of observational data, including both new UBV observations of HZ Her and earlier published data. Our detailed comparison of the system's light curves in the ordinary and in anomalous low states reveals significant differences. This contradicts the conclusion of [13, 14] that the orbital curve in the ALS does not differ from that in the normal state. This incorrect conclusion was apparently the result of the insufficient amount of data analyzed or of inadequate analysis of those data. We pay special attention to photometric measurements around the primary minimum in 1999, during a prolonged low X-ray state. The principal aim of our study was to search for changes in the disk's optical features during that time, compared to the ordinary state of the binary system.

2. OBSERVATIONS AND REDUCTION

In late March 1999, the HZ Her/Her X-1 system entered a prolonged low state, when the X-ray flux decreased approximately sevenfold. However, the system remained in its ordinary state in the optical, testifying to the continued illumination of the optical star by X-rays from the pulsar [15]. We began our observations in April 1999 with the CCD photometer of the Sternberg Astronomical Institute's Crimean Laboratory, at the Newtonian focus of the 125 cm telescope (relative aperture 1/4). The light detector was a ST-6UV camera sensitive in the ultraviolet, making possible measurements in the UBV bands. In July, we continued observations with the CCD photometer in the B and V bands using the 60 cm telescope. In August, we used the 60 cm telescope with the UBV photometer and an EMI 9789 photomultiplier as a detector.

In our observations with the UBV photometer, we used the star C3, and in the observations with the CCD photometer, the star C4 as local standards. The magnitudes and color indices of the two comparison stars were determined by Lyuty [19]: $V = 12.558^m$, $B - V = 0.558^m$, $U - B = -0.018^m$ for C3 and $V = 13.462^m$, $B - V = 0.642^m$, $U - B = 0.115^m$ for C4.

The rms errors of the individual measurements in V and B were $0.01^m - 0.02^m$ during maximum brightness and $0.02^m - 0.03^m$ during minimum brightness. The corresponding uncertainties in U were $0.02^m - 0.03^m$ and $0.04^m - 0.06^m$. However, the scatter of the data sometimes significantly exceeds the uncertainties, especially in U, due to possible short-timescale brightness variability of the optical star [17].

All our observations at brightness minimum are collected in Table 1. The last column contains information about the instrument used (phe: the UBV photometer, CCD: the CCD photometer) and the observer who made the observations (Vol: Voloshina, Gor: Goransky, Lyu: Lyuty).

In addition to the observations of HZ Her near its minimum, aimed specifically at studies of the accretion disk, we conducted ordinary (monitoring) observations of the star as part of the Sternberg Astronomical Institute's long-term program of photometric studies of binary systems with X-ray components [17, 19]. The results of these observations for HZ Her through 1988 were published in [20] (which also contains references to earlier work). The data obtained since 1989 are presented in Table 2.

Our monitoring observations were usually made once to twice per night, and we acquired $10-30$ measurements per night only when observing near the primary minimum; other authors have collected long series of observations (up to 50 or more measurements per night) at a variety of orbital phases (cf., for instance, [21, 22]). To maintain uniformity with our series of observations when plotting mean light curves, we used only some fraction of such observations, usually the first and last observation, plus several measurements in between. We reduced the volume of our near-minimum observations for the mean curve in a similar way.

In our reduction of the data obtained near the primary minimum, we applied a modified version of the algorithm used in [18]. We transformed the data presented in Table 1 in magnitudes into radiation fluxes, $\nu F_\nu^{V,B,U}$, using the calibrations from [23]. We then performed a fourth-order polynomial least-squares fit of the fluxes at phases in the range $0.91-0.09$ observed in each band. Using an orbital phase increment of 0.0005 in the same phase interval, we computed the flux from the surface of the optical star without the reflection effect, taking into account the star's ellipsoidal shape and limb darkening. We assumed the temperature at the star's pole was 8200 ± 100 K [24]. We determined the mean flux from the star's undisturbed photosphere using the orbital phase interval $0.98-0.02$ (Table 1), where the effect of the star's ellipsoidal shape is not very pronounced. The accretion disk is totally eclipsed in this phase range, as it shown by the constant-flux "plateau" of the system's

Table 1. The 1999 observations of HZ Her near the primary minimum

JD 2451000+	φ	ψ_{35}	V	B	U	Remarks
282.4235	1.0391	0.442	14.385	14.617	14.739	CCD Gor
282.4335	1.0449	0.443	14.397	14.606	14.798	CCD Gor
282.4376	1.0474	0.443	14.368	14.632	14.621	CCD Gor
282.4438	1.0510	0.443	14.373	14.598	14.753	CCD Gor
282.4500	1.0546	0.443	14.341	14.554	14.546	CCD Gor
282.4570	1.0588	0.443	14.321	14.537	14.784	CCD Gor
282.4631	1.0624	0.443	14.306	14.494	14.364	CCD Gor
282.4721	1.0676	0.444	14.285	14.474	14.524	CCD Gor
282.4798	1.0722	0.444	14.282	14.506	14.596	CCD Gor
282.4889	1.0775	0.444	14.274	14.493	14.542	CCD Gor
287.2915	0.9023	0.582	14.287	14.485	−	CCD Gor
287.3182	0.9180	0.583	14.302	14.568	−	CCD Gor
287.3311	0.9256	0.583	14.362	14.549	−	CCD Gor
287.3496	0.9365	0.584	14.258	14.512	−	CCD Gor
287.3627	0.9442	0.584	14.306	14.483	−	CCD Gor
287.3819	0.9555	0.584	14.358	14.487	−	CCD Gor
287.4282	0.9827	0.586	14.412	14.635	−	CCD Gor
287.4329	0.9855	0.586	14.413	14.605	−	CCD Gor
287.4387	0.9889	0.586	14.395	14.649	−	CCD Gor
287.4435	0.9917	0.586	14.374	14.645	−	CCD Gor
287.4565	0.9994	0.587	14.494	14.737	−	CCD Gor
287.4616	1.0024	0.587	14.479	14.715	−	CCD Gor
287.4668	1.0054	0.587	14.413	14.656	14.783	CCD Gor
287.4736	1.0094	0.587	14.417	14.692	−	CCD Gor
287.4796	1.0129	0.587	14.427	14.655	−	CCD Gor
287.4871	1.0174	0.587	14.449	14.748	−	CCD Gor
287.4945	1.0217	0.588	14.410	14.644	14.504	CCD Gor
287.5007	1.0254	0.588	14.404	14.651	−	CCD Gor
287.5075	1.0294	0.588	14.392	14.636	−	CCD Gor
287.5137	1.0330	0.588	14.360	14.639	−	CCD Gor
287.5216	1.0376	0.588	14.371	14.598	−	CCD Gor
287.5283	1.0416	0.589	14.375	14.676	14.538	CCD Gor
287.5350	1.0455	0.589	14.369	14.630	14.615	CCD Gor
287.5418	1.0495	0.589	14.323	14.544	−	CCD Gor
287.5492	1.0539	0.589	14.312	14.513	14.174	CCD Gor
287.5554	1.0575	0.589	14.272	14.473	14.247	CCD Gor
287.5616	1.0612	0.590	14.281	14.432	−	CCD Gor
287.5676	1.0647	0.590	14.256	14.575	14.189	CCD Gor
287.5738	1.0683	0.590	14.230	14.377	−	CCD Gor
372.3390	0.9253	0.021	14.380	14.520	−	CCD Lyu
372.3700	0.9434	0.021	14.400	14.570	−	CCD Lyu
372.383	0.9511	0.022	14.410	14.640	−	CCD Lyu
372.396	0.9586	0.022	14.390	14.620	−	CCD Lyu
372.408	0.9656	0.022	14.460	14.610	−	CCD Lyu
372.419	0.9726	0.023	14.530	14.580	−	CCD Lyu
372.432	0.9798	0.023	14.570	14.630	−	CCD Lyu
372.445	0.9876	0.024	14.580	14.620	−	CCD Lyu
372.457	0.9946	0.024	14.600	14.680	−	CCD Lyu
372.469	1.0016	0.024	14.580	14.630	−	CCD Lyu
379.315	1.0286	0.221	14.360	14.700	−	CCD Lyu
379.336	1.0409	0.221	14.340	14.630	−	CCD Lyu
379.353	1.0510	0.222	14.340	14.530	−	CCD Lyu
379.369	1.0599	0.222	14.380	14.410	−	CCD Lyu
384.288	0.9531	0.363	14.470	14.520	−	CCD Lyu
384.303	0.9623	0.364	14.480	14.540	−	CCD Lyu
384.316	0.9699	0.364	14.290	14.580	−	CCD Lyu

Table 1. (Contd.)

JD 2451000+	φ	ψ_{35}	V	B	U	Remarks
384.328	0.9768	0.364	14.300	14.620	−	CCD Lyu
384.339	0.9836	0.365	14.300	14.610	−	CCD Lyu
384.351	0.9905	0.365	14.300	14.610	−	CCD Lyu
384.363	0.9973	0.365	14.370	14.600	−	CCD Lyu
384.375	1.0044	0.366	14.410	14.570	−	CCD Lyu
384.387	1.0116	0.366	14.350	14.570	−	CCD Lyu
384.404	1.0216	0.366	14.350	14.580	−	CCD Lyu
384.422	1.0320	0.367	14.400	14.600	−	CCD Lyu
384.434	1.0391	0.367	14.370	14.620	−	CCD Lyu
384.450	1.0487	0.368	14.350	14.610	−	CCD Lyu
384.462	1.0555	0.368	14.300	14.540	−	CCD Lyu
384.472	1.0616	0.368	14.360	14.480	−	CCD Lyu
384.483	1.0681	0.369	14.330	14.460	−	CCD Lyu
384.495	1.0751	0.369	14.300	14.410	−	CCD Lyu
384.507	1.0822	0.369	14.240	14.350	−	CCD Lyu
396.2958	1.0162	0.707	14.546	14.700	15.053	Phe Vol
396.3108	1.0250	0.708	14.414	14.623	15.031	Phe Vol
396.3219	1.0315	0.708	14.435	14.629	15.005	Phe Vol
396.3330	1.0380	0.708	14.399	14.596	14.796	Phe Vol
396.3462	1.0458	0.709	14.306	14.552	14.743	Phe Vol
396.3576	1.0525	0.709	14.374	14.569	14.872	Phe Vol
396.3705	1.0601	0.710	14.379	14.530	14.465	Phe Vol
396.3844	1.0683	0.710	14.324	14.498	14.706	Phe Vol
396.3955	1.0748	0.710	14.319	14.512	14.445	Phe Vol
396.4059	1.0809	0.711	14.264	14.484	14.382	Phe Vol
396.4163	1.0870	0.711	14.286	14.495	14.678	Phe Vol
396.4278	1.0938	0.711	14.334	14.425	14.303	Phe Vol
401.3045	0.9622	0.851	14.395	14.578	14.736	Phe Vol
401.3177	0.9699	0.851	14.472	14.619	14.663	Phe Vol
401.3292	0.9767	0.852	14.480	14.635	14.837	Phe Vol
401.3413	0.9838	0.852	14.358	14.687	14.760	Phe Vol
401.3528	0.9906	0.852	14.385	14.618	14.657	Phe Vol
401.3635	0.9969	0.853	14.457	14.603	14.920	Phe Vol
401.3760	1.0042	0.853	14.582	14.645	14.777	Phe Vol
401.3899	1.0124	0.853	14.375	14.613	14.818	Phe Vol
401.4014	1.0192	0.854	14.433	14.590	14.754	Phe Vol
401.4153	1.0273	0.854	14.414	14.641	14.870	Phe Vol
401.4299	1.0359	0.855	14.485	14.615	14.724	Phe Vol
401.4490	1.0472	0.855	14.315	14.575	14.621	Phe Vol
401.4663	1.0573	0.856	14.213	14.511	14.381	Phe Vol
406.3215	0.9130	0.995	14.249	14.422	14.427	Phe Vol
406.3358	0.9215	0.995	14.272	14.454	14.449	Phe Vol
406.3472	0.9282	0.996	14.325	14.459	14.426	Phe Vol
406.3569	0.9339	0.996	14.287	14.477	14.587	Phe Vol
406.3653	0.9388	0.996	14.330	14.479	14.463	Phe Vol
406.3771	0.9457	0.996	14.387	14.509	14.760	Phe Vol
406.3861	0.9510	0.997	14.361	14.544	14.813	Phe Vol
406.3965	0.9572	0.997	14.399	14.581	14.928	Phe Vol
406.4104	0.9653	0.997	14.394	14.574	14.749	Phe Vol
406.4233	0.9729	0.998	14.355	14.593	14.511	Phe Vol
406.4344	0.9795	0.998	14.404	14.637	14.633	Phe Vol
406.4472	0.9870	0.998	14.372	14.603	14.536	Phe Vol
406.4597	0.9943	0.999	14.391	14.478	14.589	Phe Vol

Table 2. *UBV* observations of HZ Her after 1988

JD 2400000+	*V*	*B*	*U*	Observer	JD 2400000+	*V*	*B*	*U*	Observer
47386.281	13.09	13.02	12.21	Lyu	48100.310	13.06	13.01	12.36	Vol
47386.292	13.08	12.99	12.11	Lyu	48100.316	13.11	13.03	12.25	Vol
47387.292	14.42	14.54	14.53	Lyu	48105.331	13.11	12.93	12.25	Vol
47389.282	13.81	13.90	13.67	Vol	48117.300	13.01	12.85	12.21	Vol
47391.284	13.09	13.02	12.17	Vol	48118.266	14.18	14.33	14.29	Lyu
47394.278	13.85	14.08	13.94	Vol	48118.277	14.26	14.58	14.50	Lyu
47395.280	13.39	13.28	12.65	Vol	48119.265	13.03	12.95	12.10	Lyu
47397.328	14.10	14.23	13.84	Vol	48119.275	13.05	12.98	12.12	Lyu
47397.345	14.03	14.12	13.86	Vol	48119.284	13.00	12.94	12.14	Lyu
47397.363	14.04	14.21	14.10	Vol	48119.292	13.03	12.95	12.17	Lyu
47397.382	14.24	14.28	14.16	Vol	48119.301	13.05	13.04	12.26	Lyu
47397.398	14.13	14.34	14.10	Vol	48119.310	13.01	12.96	12.14	Lyu
47397.416	14.31	14.65	14.62	Vol	48119.320	13.02	12.94	12.15	Lyu
47421.338	14.41	14.51	14.44	Lyu	48119.328	13.06	12.98	12.20	Lyu
47645.429	13.65	13.87	13.39	Vol	48119.336	13.06	12.98	12.25	Lyu
47645.442	13.53	13.62	12.99	Vol	48119.344	13.04	13.02	12.19	Lyu
47645.454	13.58	13.55	13.04	Vol	48119.354	13.04	13.04	12.23	Lyu
47647.443	14.49	14.73	14.70	Lyu	48119.362	13.11	13.06	12.21	Lyu
47647.463	14.43	14.62	14.65	Lyu	48119.370	13.07	13.08	12.36	Lyu
47736.457	12.94	12.89	11.96	Vol	48120.336	13.63	13.81	13.44	Vol
48092.408	13.50	13.59	13.06	Vol	48120.347	13.68	13.74	13.43	Vol
48092.419	13.44	13.50	13.06	Vol	48122.280	13.09	13.02	12.33	Vol
48093.313	13.18	13.14	12.46	Vol	48122.289	13.11	12.96	12.25	Vol
48093.321	13.14	13.09	12.45	Vol	48125.349	14.00	14.24	14.06	Vol
48093.328	13.14	13.09	12.43	Vol	48127.324	13.41	13.32	12.53	Vol
48093.337	13.11	13.07	12.44	Vol	48129.403	13.20	13.18	12.45	Lyu
48093.352	13.07	13.03	12.41	Vol	48129.410	13.23	13.18	12.42	Lyu
48093.434	13.05	13.00	12.24	Vol	48130.272	14.42	14.56	14.88	Lyu
48095.310	13.30	13.23	12.59	Lyu	48130.283	14.44	14.58	14.66	Lyu
48095.334	13.32	13.25	12.63	Lyu	48131.265	13.07	12.98	12.31	Lyu
48096.291	14.26	14.44	14.49	Lyu	48131.273	13.09	13.00	12.34	Lyu
48096.303	14.34	14.50	14.54	Lyu	48132.271	13.37	13.34	12.73	Vol
48099.294	13.36	13.54	13.01	Vol	48133.275	13.56	13.63	13.14	Vol
48099.305	13.53	13.49	13.03	Vol	48133.282	13.59	13.60	13.13	Vol
48099.315	13.51	13.56	13.05	Vol	48412.342	14.50	14.65	14.86	Lyu
48099.327	13.49	13.59	13.14	Vol	48424.379	14.44	14.58	14.81	Lyu
48099.340	13.47	13.51	13.01	Vol	48511.337	13.90	14.01	13.78	Vol
48099.351	13.47	13.55	13.00	Vol	48511.350	13.84	13.98	13.72	Vol
48099.362	13.72	13.75	13.06	Vol	48514.265	13.99	14.13	13.54	Vol
48100.305	13.07	13.01	12.31	Vol	48515.303	13.49	13.44	12.75	Vol

Table 2. (Contd.)

JD 2400000+	V	B	U	Observer	JD 2400000+	V	B	U	Observer
48515.312	13.43	13.42	12.69	Vol	49217.398	13.27	13.32	12.54	Lyu
48799.355	13.30	13.27	12.56	Vol	49221.306	13.61	13.63	13.18	Lyu
48810.359	14.42	14.63	14.85	Vol	49224.289	13.18	13.26	12.44	Lyu
48829.483	13.46	13.51	12.99	Vol	49511.335	13.15	13.20	12.42	Lyu
48830.326	13.36	13.50	13.26	Vol	49516.331	13.29	13.38	12.74	Lyu
48831.289	13.30	13.32	12.64	Vol	49519.344	14.37	14.55	14.72	Lyu
48833.374	13.22	13.16	12.45	Vol	49534.338	14.08	14.22	14.14	Lyu
48834.319	14.13	14.24	14.08	Vol	49536.365	14.43	14.54	14.63	Lyu
48835.389	13.54	13.57	13.13	Vol	49537.370	13.21	13.28	12.50	Lyu
48835.403	13.59	13.62	13.16	Vol	49559.322	13.27	13.26	12.51	Vol
48836.367	13.44	13.40	12.88	Vol	49559.333	13.24	13.25	12.52	Vol
48836.378	13.44	13.41	12.76	Vol	49560.325	13.77	13.83	13.39	Vol
48836.403	13.39	13.37	12.75	Vol	49560.335	13.76	13.82	13.38	Vol
48837.335	14.28	14.50	14.49	Vol	49565.423	14.07	14.20	14.00	Vol
48838.454	13.12	13.15	12.37	Vol	49569.289	13.37	13.49	12.69	Vol
48840.364	13.35	13.38	12.72	Vol	49571.288	13.05	12.99	12.19	Vol
48840.374	13.37	13.40	12.80	Vol	49571.295	13.05	12.94	12.12	Vol
48840.393	13.47	13.45	12.80	Vol	49572.276	13.64	13.81	13.21	Vol
48840.417	13.42	13.52	12.94	Vol	49572.285	13.61	13.68	13.22	Vol
48856.372	14.17	14.16	13.88	Vol	49573.281	13.59	13.63	13.22	Vol
48858.315	13.31	13.22	12.76	Vol	49573.291	13.59	13.62	13.22	Vol
48866.281	14.00	14.10	13.85	Vol	49594.312	13.76	13.78	13.31	Lyu
48866.381	14.38	14.59	14.73	Vol	49598.342	13.28	13.31	12.54	Lyu
48867.294	13.22	13.18	12.41	Vol	49619.277	13.97	14.07	13.93	Lyu
48869.264	13.27	13.22	12.52	Vol	49840.388	13.76	13.84	13.39	Lyu
48869.297	13.27	13.21	12.57	Vol	49917.341	14.02	14.17	13.97	Lyu
48869.356	13.32	13.38	12.68	Vol	49918.331	13.38	13.41	12.85	Lyu
49133.344	14.46	14.65	14.87	Vol	49925.382	13.92	13.95	13.53	Lyu
49133.380	14.43	14.63	14.84	Vol	49926.319	12.89	12.97	12.42	Lyu
49133.411	14.44	14.60	14.83	Vol	49949.265	14.33	14.61	14.56	Vol
49133.444	14.34	14.55	14.72	Vol	49951.345	14.33	14.47	14.41	Vol
49133.460	14.18	14.24	14.49	Vol	49951.365	14.09	14.24	13.72	Vol
49138.397	14.61	14.60	14.74	Vol	49953.266	13.39	13.39	12.77	Vol
49138.413	14.43	14.59	14.93	Vol	49953.278	13.36	13.36	12.77	Vol
49138.430	14.43	14.67	14.79	Vol	49953.294	13.36	13.36	12.76	Vol
49151.373	13.15	13.18	12.39	Lyu	49955.291	13.13	13.11	12.29	Vol
49152.357	13.83	13.91	13.60	Lyu	49956.360	14.01	14.15	13.65	Vol
49159.397	13.49	13.51	12.86	Lyu	49961.295	14.51	14.67	14.84	Vol
49181.328	13.68	13.77	13.45	Lyu	49961.323	14.61	14.65	14.85	Vol
49191.327	14.08	14.13	13.96	Lyu	49961.355	14.39	14.60	14.87	Vol

Table 2. (Contd.)

JD 2400000+	V	B	U	Observer	JD 2400000+	V	B	U	Observer
49961.389	14.43	14.57	14.96	Vol	51306.389	14.05	14.21	14.02	Lyu
49961.427	14.27	14.42	14.65	Vol	51308.320	13.54	13.61	13.21	Lyu
49963.260	13.80	14.02	13.79	Vol	51313.394	13.61	13.67	13.28	Lyu
50210.298	13.00	13.04	12.12	Lyu	51319.406	13.86	13.94	13.63	Lyu
50249.318	13.14	13.11	12.37	Vol	51345.319	14.45	14.62	14.82	Lyu
50249.327	13.19	13.13	12.36	Vol	51346.313	13.36	13.30	12.61	Lyu
50250.350	14.43	14.68	14.67	Vol	51349.352	13.32	13.30	12.58	Lyu
50250.374	14.47	14.62	14.85	Vol	51368.358	13.34	13.28	12.54	Lyu
50250.396	14.44	14.63	14.74	Vol	51370.337	13.65	13.72	13.37	Lyu
50261.383	13.37	13.27	12.56	Vol	51375.340	13.51	13.51	13.06	Lyu
50308.409	13.75	13.82	13.43	Vol	51396.296	14.55	14.70	15.05	Vol
50308.420	13.71	13.81	13.29	Vol	51396.322	14.44	14.63	14.91	Vol
50311.367	13.96	14.05	13.77	Vol	51396.346	14.31	14.55	14.74	Vol
50311.378	13.98	14.12	13.81	Vol	51396.371	14.38	14.53	14.47	Vol
50315.371	13.31	13.36	12.91	Vol	51396.396	14.32	14.51	14.45	Vol
50603.333	13.10	13.16	12.38	Lyu	51396.428	14.33	14.43	14.30	Vol
50604.403	13.34	13.34	12.68	Lyu	51398.312	13.92	14.05	13.83	Vol
50606.348	13.13	13.12	12.29	Lyu	51398.343	13.80	13.91	13.74	Vol
50628.370	13.15	13.08	12.29	Lyu	51398.387	13.74	13.83	13.59	Vol
50631.351	14.22	14.36	14.50	Lyu	51398.462	13.65	13.65	13.14	Vol
50635.388	13.23	13.25	12.49	Lyu	51400.311	13.42	13.37	12.82	Lyu
50663.317	14.12	14.31	14.15	Lyu	51401.305	14.40	14.58	14.74	Vol
50687.330	14.34	14.70	14.74	Vol	51401.341	14.36	14.69	14.76	Vol
50687.350	14.43	14.68	14.67	Vol	51401.376	14.58	14.65	14.78	Vol
50704.275	14.43	14.64	14.92	Lyu	51401.415	14.41	14.64	14.87	Vol
50729.229	13.36	13.39	12.77	Vol	51401.466	14.21	14.51	14.38	Vol
51021.315	13.31	13.31	12.69	Vol	51402.366	13.32	13.28	12.61	Lyu
51021.356	13.47	13.45	12.67	Vol	51404.315	13.67	13.75	13.49	Lyu
51021.366	13.45	13.45	12.67	Vol	51406.322	14.25	14.42	14.43	Vol
51026.380	13.23	13.24	12.45	Vol	51406.357	14.29	14.48	14.59	Vol
51039.402	13.97	14.17	14.51	Vol	51406.397	14.40	14.58	14.93	Vol
51040.303	13.33	13.33	12.66	Vol	51406.434	14.40	14.64	14.63	Vol
51042.369	13.88	14.09	13.86	Vol	51406.460	14.39	14.48	14.59	Vol
51043.374	13.13	12.98	12.11	Vol	51407.365	13.42	13.34	12.63	Lyu
51045.326	13.20	13.21	12.46	Vol	51408.302	14.32	14.41	14.49	Lyu
51046.275	14.05	14.18	14.06	Vol	51410.304	13.77	13.88	13.62	Vol
51277.445	13.95	14.08	13.79	Lyu	51410.313	13.77	13.83	13.55	Vol
51285.460	13.99	14.07	14.05	Lyu	51440.231	14.30	14.48	14.51	Lyu
51294.447	14.03	14.00	13.61	Lyu	51488.175	14.40	14.63	14.78	Lyu
51305.493	13.30	13.29	12.547	Lyu					

light curve. The mean fluxes from the undisturbed atmosphere of the star are:

$$\nu \bar{F}_\nu^V = (3.39 \pm 0.17) \times 10^{-11} \text{ erg cm}^{-2}\text{s}^{-1},$$
$$\nu \bar{F}_\nu^B = (3.91 \pm 0.16) \times 10^{-11} \text{ erg cm}^{-2}\text{s}^{-1},$$
$$\nu \bar{F}_\nu^U = (1.79 \pm 0.19) \times 10^{-11} \text{ erg cm}^{-2}\text{s}^{-1}.$$

Subtracting the computed flux from the undisturbed stellar surface from the values computed using the polynomial approximation of the curve at orbital phases 0.93−0.98 and 0.02−0.07, we derived the apparent variations of the integrated flux of the accretion disk with orbital phase when entering and emerging from the eclipse. Recall that the beginning of the neutron star's eclipse corresponds to orbital phase 0.93, and the end of the eclipse to phase 0.07 [25]. Further, for selected orbital phases, we transformed the accretion-disk fluxes in each of the three bands into magnitudes and computed the color indices of the disk's integrated light seen by an observer. To obtain real color indices, we must take into account interstellar extinction, which is not large for HZ Her. In [26], a color excess of $E_{(B-V)} = 0.10^m$ was adopted. However, it has been possible to improve this value in recent years thanks to studies with the Hubble Space Telescope. The absence of absorption in the spectrum of HZ Her at $\lambda = 2200$ Å [27] gives $E_{B-V} < 0.05^m$ for an upper limit to the interstellar reddening. Studies of the interstellar extinction based on soft X-ray observations give a scatter of a factor of two in the density of interstellar hydrogen along the line of sight, though Boroson *et al.* [28] present a specific value for the color excess, $E_{B-V} = 0.018^m \pm 0.002^m$. Since such a color excess does not significantly influence the values of the computed color indices for the accretion disk, we adopted the values $E_{B-V} = 0.05^m$, $E_{U-B} = 0.035^m$.

3. RESULTS

3.1. (a) The Orbital Light Curves

We first plotted the mean U, B, and V light curves of the HZ Her/Her X-1 system applying the technique used in [20] but with the addition of new data ([13, 21, 22] and Table 2). Since we used more than twice as much data as the analysis of [20], we chose the interval for averaging over phase to be 1/15 rather than 1/20. Figure 1 compares the mean light curves for the data of 1972−1998 with the light curves of 1983 and 1999, when the system was in its ALS in the X-ray.

We can clearly see that the light curves of 1983 and 1999 differ appreciably, and that the U light curves differ significantly from the mean curves in the ordinary state. First, they show no secondary minimum

(phase 0.5); second, the primary minimum (phases from 0.8 to 0.2) is broader than for the mean curve. In addition, a deficiency of light is observed at phases 0.1−0.4 and 0.6−0.9. This could be due to a decrease in the size of the hot spot on the stellar surface formed due to heating by X-rays from the pulsar. In general, the light curves of 1983 and 1999 resemble those for the low state, when the pulsar's X-rays are blocked from the observer by the accretion disk.

3.2. (b) The Accretion Disk

Figure 2 presents our UBV data for HZ Her/Her X-1 near the primary minimum during the period of the ALS in 1999 (Table 1). It also shows data obtained near the primary minimum in August 1983 [21]. The dashed curves are the mean light curves, and the vertical dashed lines indicate the limits of the X-ray eclipse, when the hot spot on the stellar surface becomes invisible. In this phase interval, we observe the flux from rhe accretion disk and the undisturbed side of the star. In our subsequent analysis, we use only observations obtained simultaneously in the U, B, and V bands.

The observational data reduced as described above are presented in Fig. 3. Different symbols are used for observations obtained using different methods on different Julian dates. Approximations of the observing data using fourth-power polynomials are shown by the solid curves. The vertical dashed lines indicate the limits of the phase intervals of the neutron star's eclipse by the optical star. In the top of the figure, we give the linear size of the part of the accretion disk covered by the stellar limb when entering or emerging from the eclipse. In the computations of the disk radius, we used the parameters of the binary system from [25].

Figure 3 clearly shows the low flux level from the accretion disk, compared to the disk flux when the X-ray flux is in its high (main-on) state [29]. In the high state, the U flux from the half of the accretion disk entering the eclipse (the flux at phase 0.93) is almost a factor of ten higher [18] than during the prolonged low state. The B and V fluxes differ by approximately a factor of six.

The second feature of the disk's optical characteristics during the prolonged low state is the different behavior of the color indices in the $(B - V) - (U - B)$ diagram. The color indices for the part of the disk covered by the stellar limb at phase 0.93 are $U - B = -0.5^m2 \pm 0.20^m$ and $B - V = -0.08^m \pm 0.15^m$, whereas, at phase 0.95, when the radius of the eclipsed part of the disk is $R_d = 0.8 \times 10^{11}$ cm, these values are $U - B = -0.30^m \pm 0.41^m$ and $B - V = 0.01^m \pm 0.27^m$. Taking into account their large uncertainties, these color indices are situated along the
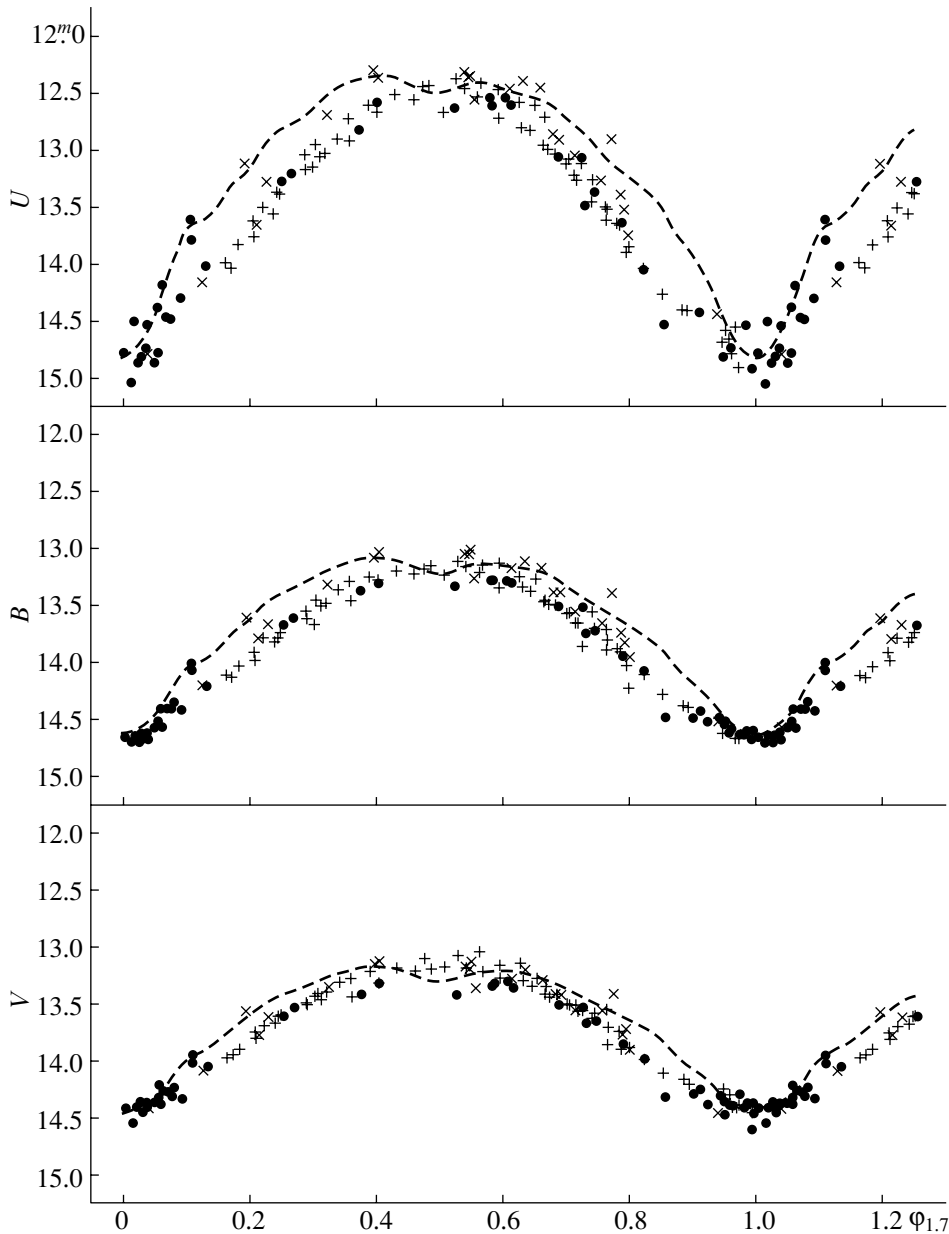
Fig. 1. The mean orbital light curves of HZ Her from observations of 1972−1998 (dashed curves) and in the anomalous low state of the X-ray flux in 1983 and 1999. Shown are the 1983 data of [21] (×), the data of [14] (+), and the 1999 data presented here (●).

curve for late-B main-sequence stars in the two-color diagram. This behavior differs appreciably from the changes in the color indices of the accretion disk's integrated light when entering eclipse during the main-on X-ray state [18]. In that state, the color indices of the inner parts of the disk lie near the curves for black bodies with $T = 20\,000$ K and early-B main-sequence stars. The color indices of the outer parts of the disk are located to the right of the black-body curve, in the area occupied by emission from hot gas

with $T > 10^4$ K and densities 10^{14}–10^{16} cm^{-3} that is optically thick in the Balmer continuum [30].

The color indices for the part of the accretion disk emerging from eclipse behave differently. At phase 0.055, when the radius of the disk that has emerged from the eclipse is $R_d = 0.6 \times 10^{11}$ cm, the color indices have the values $U - B = -1.39^m \pm 0.35^m$ and $B - V = 0.81^m \pm 0.30^m$. At phase 0.07, when we record light from the half of the accretion disk that has emerged from the disk, the color indices are $U - B = -1.17^m \pm 0.21^m$ and $B - V = 0.46^m \pm 0.19^m$. Thus, all parts of the accretion disk emerging from eclipse,
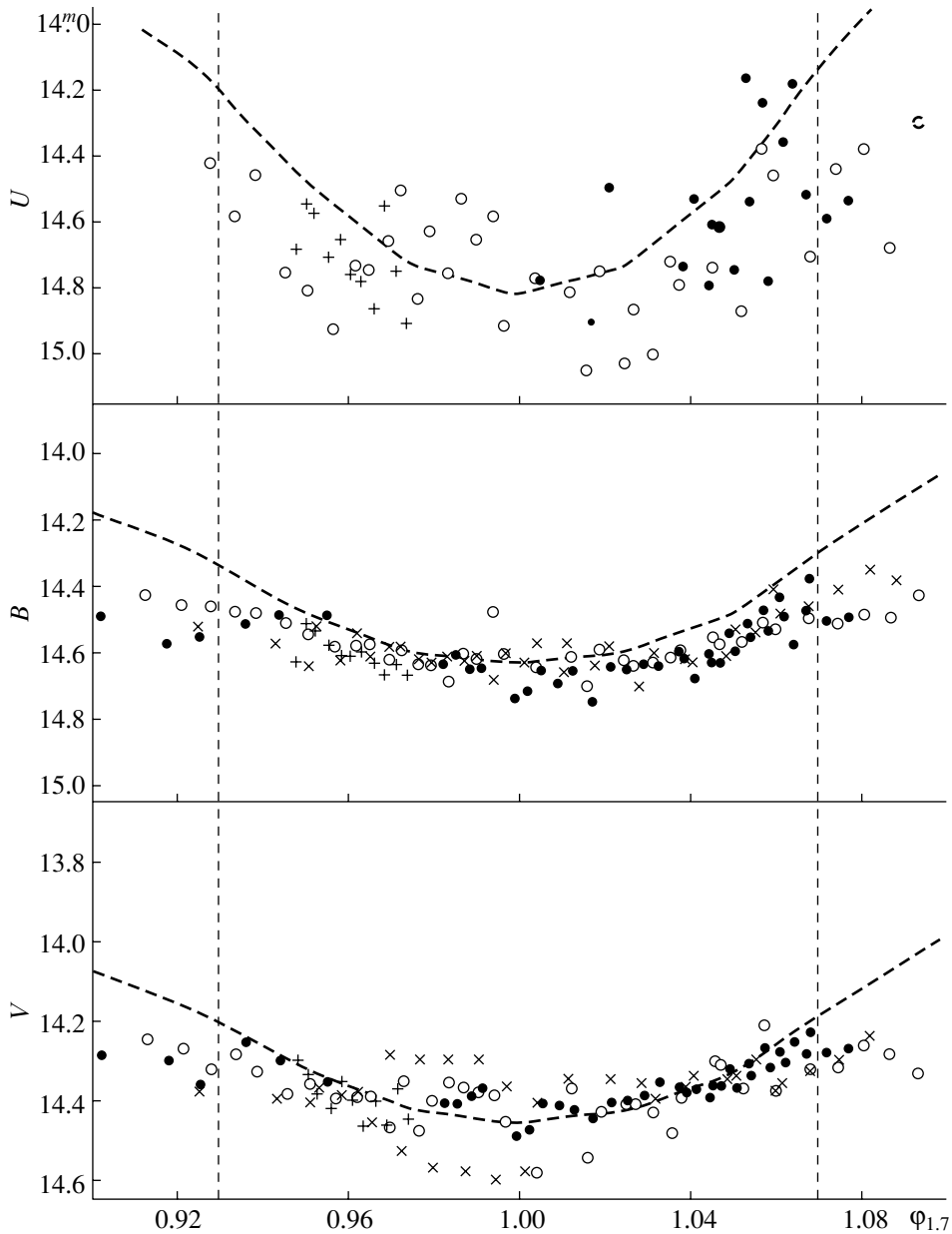
Fig. 2. Data obtained in 1999 near the primary minimum. The vertical dashed lines show the limits of the X-ray eclipse. Shown are CCD data obtained in April 1999 on the 125 cm telescope (•), photoelectric data obtained in August on the 60 cm telescope (○), CCD data obtained in July on the 60 cm telescope (×), and the 1983 observations of [21] (+). The dashed curves are the mean light curves.

including its visible part, occupy a position in the two-color diagram corresponding to emission from hot gas that is optically thick in the Balmer continuum. This situation differs from that for the main-on state, when emission from the outer parts of the disk that are emerging from behind the optical star's limb appears to the left of the black-body curve [18], corresponding to radiation from a hydrogen plasma that is optically thin in the continuum and Balmer lines with an electron temperature not exceeding 10^4 K and a density of the order of 10^6 cm^{-3} [31]. Consequently, we con-

clude that the optical features of the disk emerging from eclipse have changed dramatically. In the prolonged low state, a dense, hot hydrogen plasma is now responsible for the optical radiation from the disk as it emerges from eclipse. Sheffer and Lyutiĭ [18] concluded that the position of the outer parts of the disk to the right of the black-body curve in the two-color diagram was probably determined by the strong corona of the accretion disk formed due to the illumination of the disk by X rays.

Our analysis of observations of the Her X-1/HZ
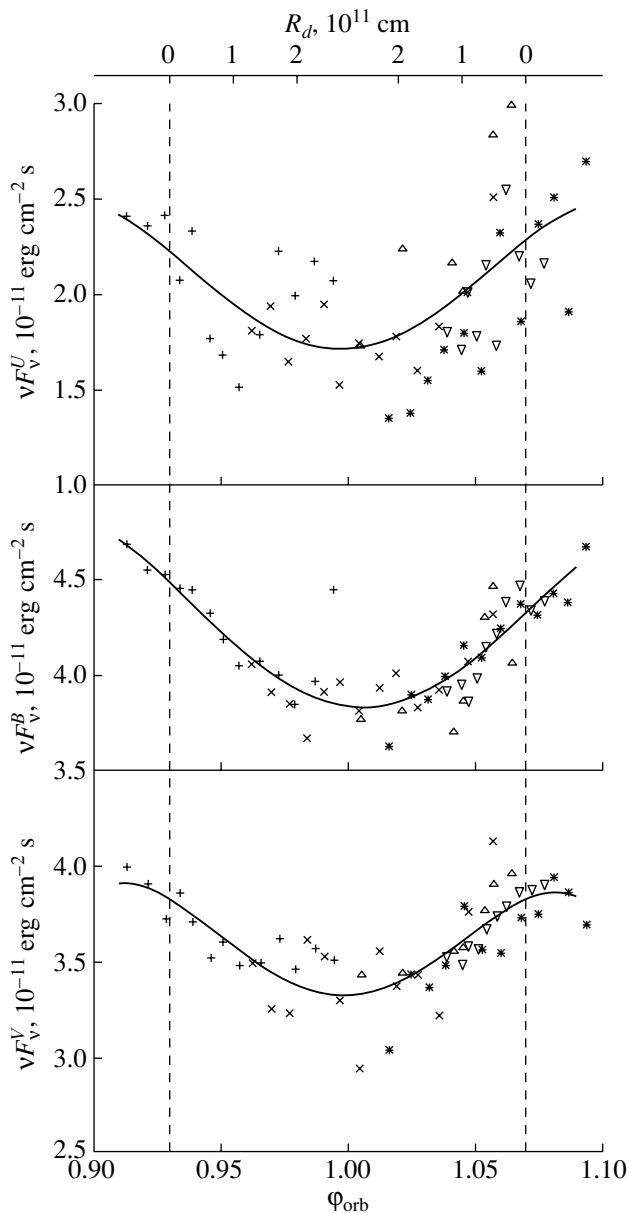
Fig. 3. The radiation flux from the accretion disk and the unheated side of HZ Her based on observations obtained in 1999. The different symbols correspond to observations obtained on different dates: JD 2451282 ($\bigtriangledown$), JD 2451287 ($\triangle$), JD 2451396 ($\ast$), JD 2451401 ($\times$), and JD 2451406 ($+$). The solid curves are approximations using fourth-power polynomials (see text).

Her system during a prolonged low X-ray state enables us to draw several conclusions based on the changes in the optical characteristics of the flux from the accretion disk.

First, the low level of emission from the accretion disk is probably due to a decrease in the disk's visible surface area. Such a change could result from a change in the disk's inclination to the orbital plane, and hence to the line of sight. As a result, the X-ray pulsar was screened from the observer by the inner edge and plane of the accretion disk, so that the X-ray flux from the pulsar switched to the low state.

Possible theoretical origins for variations in the inclination of the accretion disk and for twisting of its plane that are dependent on the strength of the disk's illumination by the X-ray flux from the pulsar were first suggested in [32]. Other reasons for the transition of the X-ray flux of Her X-1 to the prolonged low state, such as expansion of the accretion disk [33] or a strong twist of its plane [34], seem rather improbable: such variations of the disk structure do not lead to a decrease in the observed flux from the disk and, on the contrary, could possibly lead to an increase in this flux. Parmer *et al.* [35] also concluded based

on the collected X-ray data that the origin of the significant decline of the observed X-ray flux was a decrease in the accretion disk's inclination and, as a result, the screening of the pulsar's X rays from the observer. Judging from the observed reflection effect from HZ Her [33], the efficiency of X-ray generation by the pulsar itself remained virtually unchanged, though the rate of accretion onto the neutron star apparently decreased, since its rotation slowed [35].

Second, the inclination of the accretion disk to the orbital plane apparently did not decrease to zero. In that case, only the outer edge of the disk would be observed both when entering and emerging from the eclipse. However, analysis of the data shows that, when entering the eclipse, the visible part of the disk radiates like a main-sequence star, whereas, when emerging from the eclipse, the visible disk radiation is formed by hot, dense gas. This difference in the optical features of different parts of the disk shows that the disk presumably continues to be twisted, so that one of its visible halves is illuminated by the X-ray flux somewhat stronger than the other, though there is no appreciable difference in the fluxes from the two halves of the accretion disk. It is difficult to draw conclusions about the shape of the twisted plane of the disk from the data under consideration. However, a comparison of our results with those based on earlier optical observations [18], and especially on ultraviolet observations obtained with the Hubble Space telescope [28] in a period of high activity of the pulsar, clearly indicate that the half of the accretion disk covered by the disk of the optical star is usually appreciably brighter than the half of the disk emerging from the limb. This is possible only if the accretion disk is twisted such that the outer edge of the part entering eclipse is concave, while the outer edge of the other half, emerging from eclipse, is convex. Because of the large solid angle subtended by the pulsar, the first half of the disk is subject to stronger X-ray illumination than the second half. This kind of deformation of the disk is possible only if the accretion disk is precessing in the direction of the orbital motion, as was claimed earlier in [18].
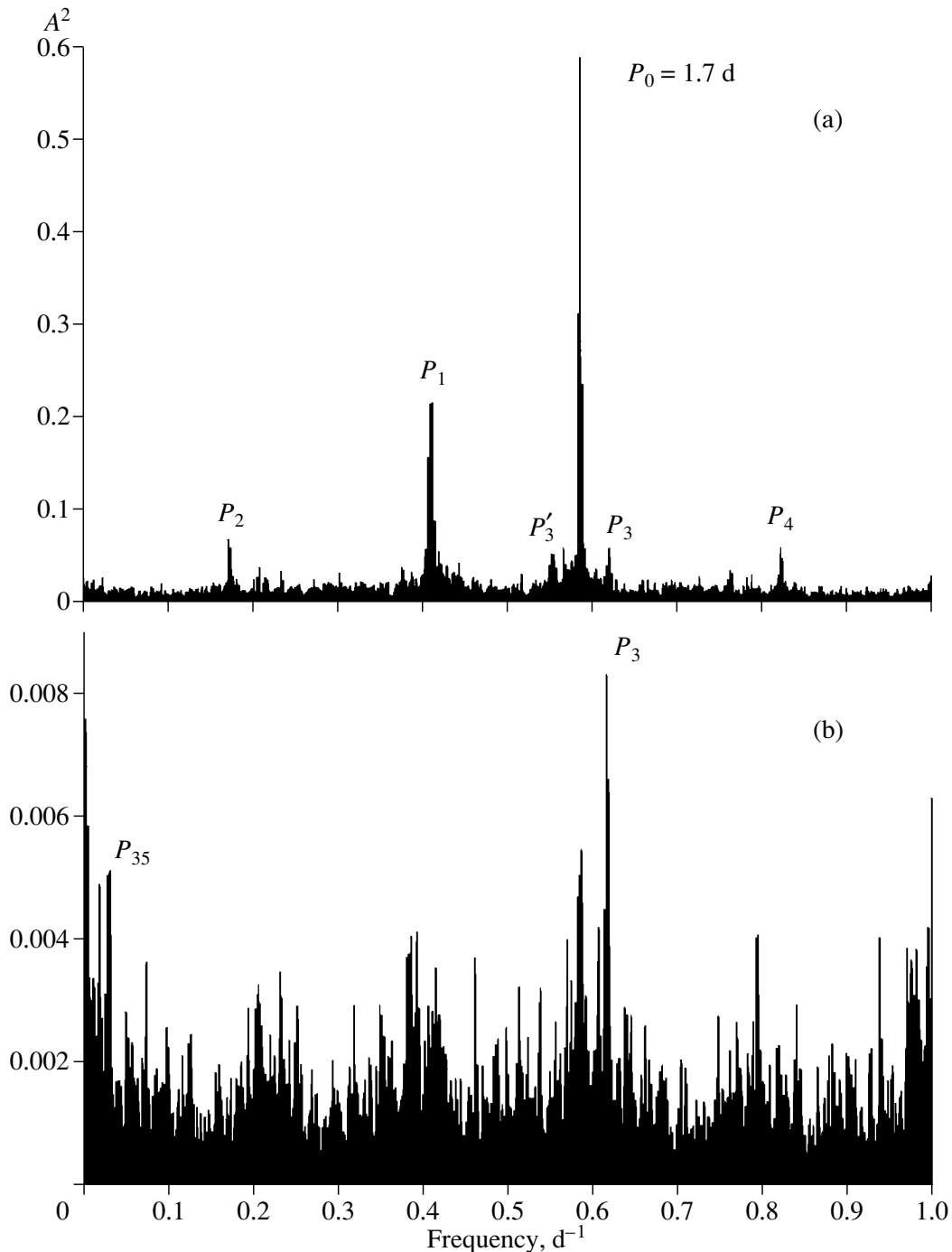
4. THE POWER SPECTRUM

The most detailed study of the power spectrum of HZ Her based on optical observations [8, 36] revealed a beat period (1.621^d) corresponding to the interaction between the orbital and 35-day periods. This led Deeter *et al.* [8] to conclude that the precession of the accretion disk in the HZ Her/Her X-1 system was retrograde. The volume of available observing material has by now increased by a factor of three to four, making it worthwhile to repeat this analysis. Despite difficulties inherent in analyses of power spectra for very non-uniform time series, as is almost always the case for astronomical photometric datasets, the analysis provides some new information.

The power spectrum in Fig. 4a was computed for data of the same series used for the mean light curve (see above), but using only the B observations, since, first, we wish to compare our results with those of [8, 36] and, second, the scatter in the data due to irregular brightness variability in the HZ Her/Her X-1 system is lowest in the B band [37] (Fig. 1). The peak corresponding to the orbital period dominates the power spectrum, and its amplitude is so high that its significance is beyond doubt. The orbital period indicated by the power spectrum is $P_o = 1.700165 \pm 0.000031^d$, very close to the most accurate period derived from the arrival times of pulses from the X-ray pulsar, $P_o = 1.70016773^d$ [25]. Peaks corresponding to the one-year aliasing of the orbital period are seen to both sides of and very close to the P_o peak. All remaining more or less significant peaks, P_1-P_4, are not independent. For example, $P_1 = 2.42836^d$ is an alias of the orbital period relative to the Nyquist frequency. Generally speaking, the Nyquist frequency, $F_{Ny} = 1/2\Delta t$, is defined for a uniform time series. However, it is often manifest in power spectra of non-uniform series of astronomical data since the observations are usually made either once per day or within intervals that are fairly short compared to a day. In Fig. 4, $F_{Ny} = 0.5$ d^{-1}. The period $P_2 = 5.67079^d$ is the beat period between P_1 and the orbital period, $1/P_2 = 1/P_o - 1/P_1$, and $P_4 = 1.21412^d$ is an alias of P_2 relative to the Nyquist frequency ($1/P_2 + 1/P_4 = 1$).

There is no obvious peak corresponding to the 35-day period (P_{35}) in the power spectrum, and the only evidence for the presence of this period is the periods P_3 ($1/P_3 = 1/P_o + 1/P_{35}$) and P_3' ($1/P_3' = 1/P_o - 1/P_{35}$). However, if we try to exclude the orbital variability by selecting data only at orbital phases from 0.3 to 0.7, a peak corresponding to the 35-day period appears in the power spectrum, $P_{35} = 34.869 \pm 0.007^d$ (Fig. 4b). It is striking that, within the errors, this period coincides with the periods determined from the shape of the X-ray pulses (34.875 ± 0.003^d) [37] and from timing of the "switching on" (34.875 ± 0.030^d) [38]. Note also that the significances of P_3, P_3', and P_{35} are low (as already noted in [8]), and these peaks do not exceed 3σ of the normal distribution.

Thus, the original power spectrum has only one significant peak, corresponding to the orbital period, $P_o = 1.7^d$ (Fig. 4a). Any data filtering to exclude the orbital period can lead to the appearance of numerous other peaks, which are statistically insignificant artifacts (Fig. 4b).

Fig. 4. Power spectra of HZ Her from optical (B) observations obtained in 1972−1998. (a) Power spectrum of the initial series of observations. The dominant peak corresponds to the orbital period, and other significant peaks are not independent; there is no pronounced peak corresponding to the 35-day period. (b) Power spectrum for the same series, but with the orbital variability (the 1.7-day period) pre-whitened. A low-significance peak corresponding to the 35-day period has appeared. The dominant peak is $P_3 = 1.62^d$, corresponding to beating between the orbital and 35-day periods.

5. CONCLUSIONS

Our analysis of UBV observations of the binary system HZ Her/Her X-1 acquired during both states of normal X-ray activity and the anomalous low state demonstrates that the system's orbital light curves are appreciably different in these two states. During anomalous low states observed in 1983−1984 and in 1999−2000, the orbital light curve has a narrower profile than during the high level of the system's X-ray activity. It is claimed in [39] that the contin-

uum emission in the ultraviolet nearly halves during such periods, but a stronger decrease of the radiation intensity is observed when entering or emerging from eclipse. The changes in the shape of the light curve can probably be explained as the effect of different conditions for the illumination of the optical star by the X-ray flux from the pulsar Her X-1. Early studies [40, 41] proposed that the variations in the shape of the optical light curve with the 35-day cycle could be due to variations in the beam width of the X-ray flux from the pulsar.

During anomalous low states, the size of the hot spot on the stellar surface probably decreases. This decrease could be due to changes in the geometric characteristics of the accretion disk in the binary system, namely, with a decreasing inclination of the disk to the orbital plane. When the accretion disk is situated nearly in the orbital plane, it will considerably screen the optical star from the pulsar's X rays. In addition, the visible surface area of the disk decreases significantly during the ALS, greatly reducing the optical flux from the disk, which decreases severalfold compared to the flux in periods of high X-ray activity. During the ALS, the observer sees the accretion disk nearly edge-on, as suggested by the nearly equal color indices of the disk when it is eclipsed by the optical star and when it emerges from eclipse. This behavior of the disk's optical characteristics differs from the variations of the color indices of the same parts of the disk during the high X-ray state.

Comparing the apparent brightnesses of different parts of the accretion disk in the optical and ultraviolet for different states of the system's X-ray activity and at different phases of the 35-day cycle, we conclude that the system's accretion disk precesses in the direction of the orbital motion. This contradicts earlier conclusions that the precession of the disk in the HZ Her/Her X-1 system is retrograde, based on analysis of power spectra computed from optical data obtained during the first years of extensive *UBV* observations of the system. However, our new analysis of power spectra based on a larger volume of statistical material (optical photometry of HZ Her acquired over 27 years) shows that it is not possible to reliably determine the direction of the accretion-disk precession solely on the basis of a power-spectrum analysis.

ACKNOWLEDGMENTS

REFERENCES

1. R. Giacconi, H. Gursky, E. Kellogg, *et al.*, Astrophys. J. **184**, 227 (1973).
2. H. Tananbaum, H. Gursky, E. M. Kellogg, *et al.*, Astrophys. J. Lett. **174**, L143 (1972).
3. W. Liller, IAU Circ., No. 2415 (1972).
4. A. M. Cherepashchuk, Yu. N. Efremov, N. E. Kurochkin, *et al.*, Inf. Bull. Var. Stars, No. 720 (1972).
5. V. M. Lyuty, R. A. Syunyaev, and A. M. Cherepashchuk, Astron. Zh. **50**, 3 (1973) [Sov. Astron. **17**, 1 (1973)].
6. J. I. Katz, Nature, Phys. Sci. **246**, 87 (1973).
7. J. A. Petterson, Astrophys. J. Lett. **201**, L61 (1975).
8. J. Deeter, L. Crosa, D. Gerend, and P. E. Boynton, Astrophys. J. **206**, 861 (1976).
9. A. N. Parmar, W. Pietsch, S. McKechnie, *et al.*, Nature **313**, 119 (1985).
10. S. Vrtilek, T. Mihara, F. A. Primini, *et al.*, Astrophys. J. Lett. **436**, L9 (1994).
11. R. Hudec and W. Wenzel, Bull. Astron. Inst. Czech. **27**, 325 (1976).
12. R. Hudec and W. Wenzel, Astron. Astrophys. **158**, 396 (1986).
13. A. J. Delgado, H. U. Schmidt, and H.-C. Thomas, Astron. Astrophys. **127**, L15 (1983).
14. A. V. Mironov, V. G. Moshkalev, E. M. Trunkovskiĭ, and A. M. Cherepashchuk, Astron. Zh. **63**, 113 (1986) [Sov. Astron. **30**, 68 (1986)].
15. A. N. Parmar, T. Oosterbroek, S. Del Sordo, *et al.*, Astron. Astrophys. **353**, 575 (1999).
16. N. E. Kurochkin, Peremen. Zvezdy **18**, 425 (1972).
17. V. M. Lyuty and I. B. Voloshina, Pis'ma Astron. Zh. **15**, 806 (1989) [Sov. Astron. Lett. **15**, 347 (1989)].
18. E. K. Sheffer and V. M. Lyuty, Astron. Zh. **74**, 209 (1997) [Astron. Rep. **41**, 181 (1997)].
19. V. M. Lyuty, Peremen. Zvezdy **18**, 417 (1972).
20. I. B. Voloshina, V. M. Lyuty, and E. K. Sheffer, Pis'ma Astron. Zh. **16**, 625 (1990) [Sov. Astron. Lett. **16**, 267 (1990)].
21. H.-C. Thomas, J. Africano, A. J. Delgado, and H. U. Schmidt, Astron. Astrophys. **126**, 45 (1983).
22. N. N. Kilyachkov, V. S. Shevchenko, S. D. Yakubov, *et al.*, Pis'ma Astron. Zh. **20**, 664 (1994) [Astron. Lett. **20**, 569 (1994)].
23. J. J. O'Dell, W. A. Stein, and J. W. Warner, Astrophys. J., Suppl. Ser. **38**, 267 (1978).
24. S. J. Boyle, I. D. Howard, R. Wilson, and J. C. Raymond, Adv. Space Res. **8**, 509 (1989).
25. J. E. Deeter, P. E. Boynton, and S. H. Pravdo, Astrophys. J. **247**, 1003 (1981).
26. J. B. Oke, Astrophys. J. **209**, 547 (1976).
27. F. H. Chang, S. D. Vrtilek, and J. C. Raymond, Astrophys. J. **452**, 825 (1995).
28. B. Boroson, T. Kallman, S. D. Vrtilek, *et al.*, Astrophys. J. **529**, 414 (2000).
29. R. Kippenhahn, H. U. Schmidt, and H. C. Thomas, Astron. Astrophys. **90**, 54 (1980).
30. R. E. Gershberg, V. P. Grinin, I. V. Il'in, *et al.*, Astron. Zh. **68**, 548 (1991) [Sov. Astron. **35**, 269 (1991)].

31. T. S. Belyakina and N. Kh. Minikulov, Izv. Krym. Astrofiz. Obs. **76**, 51 (1987).
32. J. E. Pringle, Mon. Not. R. Astron. Soc. **281**, 357 (1996).
33. A. M. Levine, IAU Circ., No. 7139 (1999).
34. W. Coburn, W. A. Heindl, J. Wilms, *et al.*, Astrophys. J. **543**, 351 (2000).
35. A. N. Parmar, T. Oosterbroek, D. Dal Fiume, *et al.*, Astron. Astrophys. **350**, L5 (1999).
36. L. Crosa and P. E. Boynton, Astrophys. J. **235**, 999 (1980).
37. N. G. Bochkarev, V. M. Lyuty, E. K. Sheffer, and I. B. Voloshina, Pis'ma Astron. Zh. **14**, 992 (1988) [Sov. Astron. Lett. **14**, 421 (1988)].
38. S. S. Holt, I. J. Kaluzienski, E. A. Boldt, and P. J. Serlemitsos, Astrophys. J. **227**, 563 (1979).
39. S. D. Vrtilek, H. Quaintrell, B. Boroson, *et al.*, Astrophys. J. **549**, 522 (2001).
40. G. S. Bisnovatyĭ-Kogan and B. V. Komberg, Astron. Zh. **52**, 457 (1975) [Sov. Astron. **19**, 279 (1975)].
41. G. S. Bisnovatyĭ-Kogan, A. V. Goncharsky, B. V. Komberg, *et al.*, Astron. Zh. **54**, 241 (1977) [Sov. Astron. **21**, 133 (1977)].

Translated by N. Samus'

The Brightness Distribution over a Stellar Disk Derived from Observations of Microlensing by a Binary System

M. B. Bogdanov[1] and A. M. Cherepashchuk[2]

[1]*Chernyshevsky University, Saratov, Russia*
[2]*Sternberg Astronomical Institute, Universitetskiĭ pr. 13, Moscow, 119899 Russia*
Received March 13, 2002; in final form, May 23, 2002

Abstract—Using a model-independent technique, we have reconstructed a one-dimensional strip distribution of the brightness over a stellar disk from observations of microlensing of a Galactic bulge star by a caustic of the binary gravitational lens OGLE-1999-BUL-23, obtained by the international PLANET group. The ill-posed inverse problem was solved using a regularization method taking into account the non-negativity of the brightness distribution. The radial brightness distribution was searched for on a compact set of convex-upward, monotonically non-increasing, non-negative functions, assuming that the source is circularly symmetrical. The reconstructed brightness distribution is compared with the results of model fitting and limb-darkening calculations based on models of stellar atmospheres. © 2002 MAIK "Nauka/Interperiodica".

1. INTRODUCTION

Gravitational microlensing of stars by massive compact objects is of considerable interest in connection with many problems in astronomy and astrophysics [1]. One important application of this effect is its use to obtain high angular resolution in studies of stars. The cosmic lenses can provide the extremely high resolution of several microarcseconds. Unfortunately, in the most common case of a point-like gravitational lens, the lensing curve is relatively insensitive to the brightness distribution of the lensed object [2−4]. An exception is the rare situation when a gravitational lens is projected onto the disk of a star [5, 6]. The characteristic potential of the binary gravitational lens results in the formation of caustics in the source plane, whose intersection can give rise to the appearance or disappearance of additional images of the star, accompanied by dramatic variations of the flux amplification factor [7, 8]. On the caustic itself, the flux amplification factor for a lensed point source formally tends to infinity, sharply increasing the sensitivity of the lensing curve to the brightness distribution [4, 9]. Currently, about twenty passages of stars across gravitational-lens caustics have been observed [10−13].

Another important manifestation of caustics are so-called high-amplitude events in the fluxes of multiple images of a quasar formed by a gravitational lens. These originate due to microlensing of stars belonging to the lensing galaxy. The brightness distribution in the accretion disk of the quasar can be derived from the corresponding light curves [14−16].

Observations of microlensing by stars are usually analyzed by selecting a model based on the mass ratio of the lens components, the geometrical parameters of the relative motion of the lens and star, and the brightness distribution over the disk of the star. The central problem here is that such models have a large number of free parameters. Even in the simple case of a static, two-particle binary lens and a source with a uniform disk brightness, the number of the parameters is nine [10]. If a non-linear law for the limb darkening is used and the reduction factors for three independent sets of two-filter observations are taken into account, the number of parameters increases to 19 [11]. Along with computational problems, this sharply aggravates interdependences between the model parameters. In addition, the fact that, like most inverse problems in astrophysics, this problem is ill-posed becomes significant [17]. Noise in the original data can result in instability and ambiguity in the parameter estimates. For example, two appreciably different sets of model parameters obtained in [10] described the observed lensing curve essentially equally well.

For most stars, model atmospheres calculated in a plane-parallel geometrical approximation are available and describe the expected limb-darkening law reasonably reliably. However, late-type giants should possess extended atmospheres, which are substantially more difficult to calculate, and the derived disk brightness distributions cannot be easily parametrized. When the image of a quasar core is microlensed by stars of a lensing galaxy, a random

field of caustics originates, which is virtually impossible to model. In addition, no reliable models for the brightness distribution in the accretion disk of a quasar are currently available. It is therefore of considerable interest to analyze such observational data using a model-independent technique that either totally excludes free parameters or decreases their number substantially. We applied one such technique to the MACHO 98-SMC-1 microlensing event [9] to reconstruct the brightness distribution over the stellar disk from observations of the star's crossing of a gravitational-lens caustic. In [16], we solved a similar problem, reconstructing a one-dimensional strip brightness distribution for the accretion disk of a quasar from observations of microlensing of component C of the gravitational lens QSO 2237+0305.

Here, we analyze the microlensing of a Galactic-bulge star by a caustic of the binary gravitational lens OGLE-1999-BUL-23, observed by the international PLANET group.

2. DATA ANALYSIS

Our technique for analyzing observations of microlensing of a star by a gravitational-lens caustic is described in detail in [9], and we will only briefly summarize its central tenets here. Given the small angular sizes of Galactic bulge stars, the curvature of the caustic can generally be neglected, so that it can be considered a straight line. Then, the characteristic observed lensing curve will depend only on the one-dimensional projection $B(x)$ of the two-dimensional brightness distribution over the source $b(x, y)$ onto the x axis, perpendicular to the caustic. The projection $B(x)$ is commonly called a strip distribution, and is related to the two-dimensional brightness distribution $b(x, y)$ by the equation

$$B(x) = \int_{-\infty}^{\infty} \int_{-\infty}^{\infty} b(\xi, y)\delta(\xi - x)d\xi dy, \qquad (1)$$

where $\delta(x)$ is the Dirac delta function. The integral equation (1) describes the scanning of the two-dimensional brightness distribution over the source by an infinitely narrow knife-edge beam perpendicular to the x axis. Thus, only a strip distribution of the brightness can be derived from observations of crossing of a gravitational-lens caustic.

In general, a set of strip distributions with different scanning directions is needed to derive the two-dimensional brightness distribution. The problem of reconstructing the object image from a set of one-dimensional projections is called computer tomography, and its methods are well developed [18]. However, in the case of circular symmetry, which

is relevant for the vast majority of stars, the radial brightness distribution $b(r)$ is unambiguously related to $B(x)$ via the Abell integral equation

$$B(x) = \int_{x}^{\infty} 2b(r)rdr/\sqrt{r^2 - x^2}. \qquad (2)$$

For definiteness, let us consider the second caustic crossing, which is accompanied by a sharp decrease of the flux and is generally recorded in more detail than the first crossing. Let us denote ξ to be the angular distance of the current point of the strip distribution $B(\xi)$ from its center, and x to be the angular distance of the source center from the caustic. Then, the flux amplification factor for a source with infinitely small extent in the x direction near the time of the caustic crossing can be expressed [7, 8] as

$$A(x, \xi) = A_0 + kH(\xi - x)/\sqrt{\xi - x}, \qquad (3)$$

where A_0 is the flux amplification factor for source images formed by the lens that do not disappear in the course of the crossing, k is a factor that depends on the parameters of the gravitational lens, and $H(\xi - x)$ is the step-like Heavyside function, which is equal to zero and unity for negative and non-negative arguments, respectively. Near the time of the caustic crossing, A_0 and k can be considered constant. The observed light curve $I(x)$, usually called the lensing curve, is

$$I(x) = \int_{-\infty}^{\infty} A(x, \xi)B(\xi)d\xi. \qquad (4)$$

Expression (4) is a Fredholm integral equation of the first kind, and it is known that the inverse problem of deriving the strip brightness distribution $B(x)$ along the observed lensing curve $I(x)$ is ill-posed [17]. This was first recognized for gravitational microlensing in [14], where the problem was solved using a Tikhonov regularization technique. However, this regularization method uses minimum *a priori* information about the function $B(x)$, which makes the solution less stable to random noise. When the lensed sources are stars, we can take into account a substantially larger volume of *a priori* information and introduce a number of qualitative restrictions for the solution in accordance with the physical nature of the phenomenon (the non-negativity of $B(x)$, the presence of circular symmetry of the stellar disk, the absence of increases in $b(r)$ with distance from the center, etc).

The second important fact related to (4) is that its kernel $A(x, \xi)$ possesses a singularity at the point $\xi = x$. This results in certain difficulties in reducing the observational data. General questions concerning
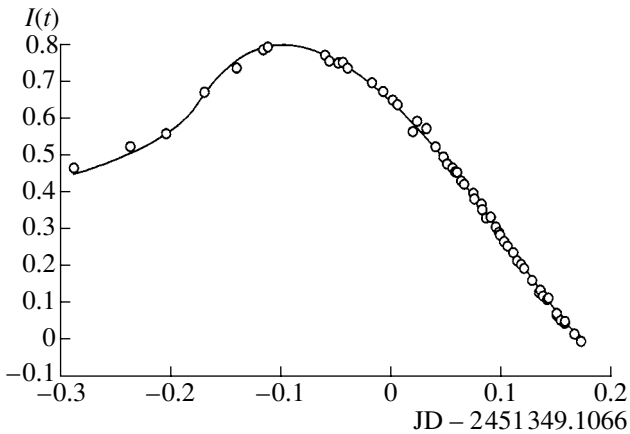
Fig. 1. Counts of the lensing curve of OGLE-1999-BUL-23, observed in the I band near the second caustic crossing (circles). The solid curve indicates the lensing curve corresponding to the reconstructed radial brightness distribution over the stellar disk.

the solution of such singular integral equations are considered in [19]. It was shown in [20] that, as applied to equation (4) with the kernel (3) in the case of the strip brightness distributions that are inherent to real astronomical objects, the corresponding integral sum converges when the sequences of counts x_i and ξ_i form a so-called canonical partitioning of the integration interval (uniform grids with the condition $\xi_i = (x_i + x_{i+1})/2$). Other ways of partitioning are also possible, when an integer number of counts ξ_i lie within the limits of the interval of counts of the sequence x_i [20]. In any case, a search for $B(\xi)$ on a uniform grid ξ_i requires specifying $I(x)$ on a uniform grid as well. Therefore, the observational data must be interpolated to grid points, since the observed lensing-curve counts usually display a fairly random distribution in time.

When the lensed source displays circular symmetry, we can derive an integral equation relating the observed lensing curve $I(x)$ to the radial brightness distribution over the source $b(r)$ by combining (2) and (4):

$$I(x) = \int_0^\infty S(x, r) b(r) dr. \tag{5}$$

The calculation of the kernel of this equation $S(x, r)$ is considered in detail in [9]. The reduction of the problem to (5) makes it possible to use additional *a priori* information about the brightness distribution. For stars with extended atmospheres, the solution can be determined on the compact set of monotonically non-increasing, non-negative functions. For normal stars, it is convenient to search for the solution of (5) on the compact set of monotonically non-increasing,

convex-upward, non-negative functions [17]. These restrictions on the possible form of $b(r)$ are imposed by the physical nature of the problem and, in addition, make it stable to the influence of random noise.

Since (4) and (5) are linear, the lensing curve can be modified by subtracting the flux level to which it decreases immediately after the caustic crossing in the region where the second term of (3) is equal to zero. After subtracting this flux level, specified by the value A_0, the problem becomes degenerate in the sense that, since the lens parameters are unknown, the brightness distributions can be derived from (4) or (5) only to within an arbitrary constant.

The angular distance $x = V(t - t_0)$, where V is the angular velocity of the source's motion towards the caustic and t_0 is the time when the caustic crosses its center. The value V depends on the relative spatial velocity and the distance to the source, as well as the angle at which it crosses the caustic, and is generally unknown. This means that the angular size of the brightness distributions is determined from (4) and (5) also to within an arbitrary factor. Below, we will assume that the zero level has been estimated and subtracted; accordingly, we will adopt $A_0 = 0$ and will assume $k = 1$ and $V = 1$.

Thus, in the absence of a model for the gravitational lens, observations of the passage of a source across a caustic can yield only the shape of the brightness distribution. However, for many purposes, this is sufficient. In particular, a comparison between these data and theoretical calculations can be used to test models of stellar atmospheres in a way that is independent of spectral data.

3. OBSERVATIONS OF THE STELLAR MICROLENSING EVENT OGLE-1999-BUL-23

The microlensing of a Galactic bulge star OGLE-1999-BUL-23 was observed in the V and I filters by the international PLANET group in June–August 1999 [12]. Four observatories were involved: Sutherland (South Africa), Bickley (Australia), Hobart (Tasmania), and Cerro Tololo (Chile). Therefore, the first task was to reduce the individual sets of observations to a single photometric system. This is by no means easy, given the difficulty of performing photometry in crowded stellar fields, due to the seeing-dependent nature of blending. In [12], the reduction was carried out in two stages. The data sets in each filter were first reduced to a single flux level for the star away from the caustic. In the second stage, the data sets were fitted to the lensing curve corresponding to the best-fit model of the event, taking into account the seeing. At the same time, we determined multiplicative factors needed to increase the standard deviations of the individual counts found
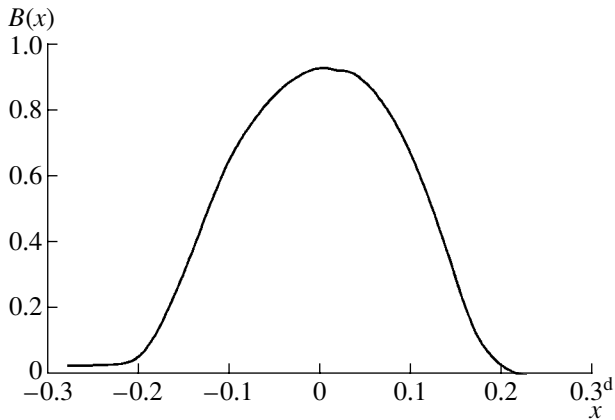
Fig. 2. The one-dimensional strip brightness distribution over the disk of the lensed star, reconstructed by the regularization method taking into account the non-negativity of the distribution.

Fig. 3. Radial brightness distribution over the stellar disk, derived for the set of convex-upward, monotonically non-increasing, non-negative functions (solid curve). The dashed curve indicates the distribution for the linear limb-darkening law of the star from model-atmosphere calculations.

by the DoPHOT code for the reduction of CCD photometry data. This is important for the subsequent analysis, since such codes usually underestimate the errors.

To reconstruct the brightness distributions, we used the densest set of I fluxes, obtained near the time of the second caustic crossing, after they had undergone the first stage of the reduction. Despite the fact that the scatter of the flux counts is somewhat smaller after the second stage of the reduction, they can no longer be considered model independent. On the other hand, since the total flux level is fairly high, the effect of blending should be small. Dr J. An, one of the participants of the PLANET group, kindly sent us data files containing the Julian dates of the observation times, the stellar-magnitude counts, and their rms errors. We increased the errors using the factors derived in [12]. The lensing-curve counts were transformed into a flux scale with the maximum value set equal to unity. The flux zero level, specified as the weighted average of the 16 counts immediately following the brightness decrease, was equal to 0.2043 ± 0.0010. The circles in Figure 1 indicate the 55 flux counts used with the zero level subtracted. Adopting the angular velocity $V = 1$, we will measure $x_i = t_i - t_0$ in fractions of days. We initially adopted the epoch JD_{hel} 2451349.1066 obtained in [12] for the time t_0. Further, the lensing curve and errors were linearly interpolated onto a uniform 100 point grid.

In the first stage of the analysis, we reconstructed the strip brightness distribution by solving (4) using the regularization method, taking into account the non-negativity of $B(x)$ [21]. In this case, we seek the smoothest solution for which the residual corresponding to the difference between the lensing-curve counts $I_c(x_i)$ and the observed curve $I_o(x_i)$ is consistent with the value expected for the errors in the data.
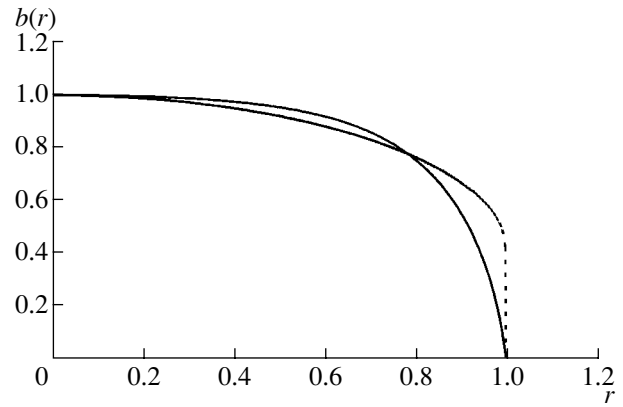
It is convenient to use the residual

$$\chi_N^2 = \sum_{i=1}^{N} [(I_0(x_i) - I_c(x_i))/\sigma_i]^2, \qquad (6)$$

where N is the number of lensing-curve counts and σ_i are the estimated errors for these counts. The expected χ_N^2 should be equal to the number of the degrees of freedom N.

Figure 2 presents the reconstructed strip brightness distribution. Unlike the previous reconstruction for the MACHO 98-SMC-1 event [9], $B(x)$ displays a smooth, essentially symmetrical outline. This indicates that we did not underestimate the count errors. The size of the profile coincides with the model-fitting data, according to which the radius of the star corresponds to the time interval $0\overset{d}{.}1707 \pm 0\overset{d}{.}0009$ [12]. The angular radius of the star estimated in [12] is $0\overset{''}{.}00000186 \pm 0\overset{''}{.}00000013$. The fact that the left wing of the profile $B(x)$ tends to a value slightly different from zero is probably due to the observational errors and the small density of counts of the curve $I(x)$ in its initial interval.

The resulting strip brightness distribution enables us to correct the x-axis origin. As follows from (4), the time shift $t_0 - \Delta t$ will be equal to the shift of the center of gravity of the reconstructed profile $B(x)$. In our case, $\Delta t = -0\overset{d}{.}0027$. This is likewise consistent with the model fitting ($\Delta t = 0\overset{d}{.}0000 \pm 0\overset{d}{.}0006$), given the large number of parameters and the fact that their formal errors are usually underestimated [22]. The error of the derived Δt depends on the accuracy of the reconstruction $B(x)$, which is impossible to estimate using the regularization method [17]. The non-zero value and sign of Δt are probably due to the slight

asymmetry of $B(x)$. On the whole, the reconstruction of the strip brightness distribution is consistent with the assumed circular symmetry of the lensed source. This leads to the next stage of the reduction using supplementary *a priori* information.

We can conclude from the estimates of parameters of the lensed star obtained in [12] that the star cannot possess an extended atmosphere. Therefore, we searched for the solution for (5) on a compact class of monotonically non-increasing, convex-upward, non-negative functions [17] by minimizing the residual (6) for various radii of the star R. To ensure complete independence from the model fitting and the result of the $B(x)$ reconstruction, we used the correction for the Δt origin as the second parameter of the problem. The minimum residual (6) was achieved for $R = 0\overset{d}{.}176 \pm 0\overset{d}{.}002$ and $\Delta t = 0\overset{d}{.}000 \pm 0\overset{d}{.}002$, in agreement with the model-fitting results. The radial brightness distribution corresponding to the minimum residual is shown by the solid curve in Fig. 3. The normalization of the distribution is specified by the conditions $R = 1$, $b(0) = 1$. The corresponding lensing curve $I_c(x)$ is represented by the solid curve in Fig. 1, and is in sufficiently good agreement with the observations.

It is of interest to compare the derived brightness distribution $b(r)$ with calculations of model stellar atmospheres. The most detailed grid of models for plane-parallel atmospheres and the corresponding brightness distributions for various wavelengths were calculated by Kurucz [23]. A more compact description for limb darkening is achieved using simple laws, such as the linear law

$$b_m(\mu) = b(1)(1 - u + u\mu), \qquad (7)$$

where μ is the cosine of the angle between the line of sight and the normal to the surface of the star, and u is the limb darkening factor. Values of the parameter u for stars with various effective temperatures T_{eff} and surface gravities g were obtained in [24] for bands of IR photometric systems. If we adopt for the star $\log g\ [\text{cm s}^{-2}] = 3.5$ and $T_{\text{eff}} = 4830$ K, in accordance with [12], the factor u is 0.58 in the I band [24]. When calculating the brightness distribution using (7), we took into account the fact that the μ_i values corresponding to the uniform grid of counts r_i are related to them by the expression $\mu_i = \sqrt{R^2 - r_i^2}/r_i$. Figure 3 presents the derived model brightness distribution $b_m(r)$ (dashed curve).

We can see from Fig. 3 that the limb darkening for the reconstructed brightness distribution is substantially higher than for $b_m(r)$. It is possible that this was affected by the uncertainties in the stellar parameters; however, the most likely reason for this deviation is errors in the reconstruction $b(r)$. Note that the

value $u = 0.63$ [12] obtained by the model fitting also exceeds the theoretical value. Earlier, we estimated the expected error in the limb-darkening factor for the currently achievable observational accuracy [9]. Later, similar results were obtained by Rhie and Bennett [25], who estimate that, in order to estimate the caustic microlensing u with an accuracy of ± 0.10, the observational errors should not exceed $0.3-0.8\%$. Thus, if we wish to obtain more reliable information about brightness distributions over stellar disks, the accuracy of observations must be increased.

Nevertheless, our lensing-curve analyses carried out using various methods and *a priori* information lead to good mutual consistency between the results, and the reconstructed radial brightness distribution is also qualitatively consistent with model-atmosphere calculations. This indicates that our technique is able to produce stable estimates of the brightness distributions, even in the presence of comparatively high noise levels.

4. CONCLUSION

Our model-independent technique for the analysis of lensing curves observed during the passage of a star across a gravitational-lens caustic can be used to reconstruct the shape of the brightness distribution over the disk of a lensed star without knowing the parameters of the lens. When the flux errors are known exactly, it is not necessary to introduce any free parameters in the reconstruction of the strip brightness distribution. Even when no information about the measurement errors is available, the single parameter Δt is sufficient for the reconstruction of the radial brightness distribution on a compact set of monotonic and limited functions, since the size of the search area for $b(r)$ can be taken to clearly exceed the expected size of the star. When $b(r)$ is searched for on a set of convex-upwards, monotonically non-increasing, non-negative functions, two free parameters are sufficient: R and Δt.

The results of our reconstruction of the strip and radial brightness distributions over the stellar disk from observations of the OGLE-1999-BUL-23 microlensing event are consistent both with each other and with the results of model fitting. Therefore, the application of this technique to the analysis of other events involving microlensing by gravitational-lens caustics, including the reconstruction of the brightness distributions of the accretion disks of quasars, is very promising.

The origin of the term "microlensing" is associated with the fact that the multiple images of a source formed by the gravitational lens are not resolved, and only variations of the flux from the lensed source are detected. However, the appearance or disappearance

of additional images of the source in the course of the caustic crossing can lead to a shift in the center of gravity of the images, which can be detected by currently designed space interferometers. This opens up fresh opportunities for studies of gravitational microlensing. The behavior of the stellar images in the course of the caustic crossing associated with the event OGLE-1999-BUL-23 was analyzed in [26].

5. ACKNOWLEDGMENTS

REFERENCES

1. A. F. Zakharov and M. V. Sazhin, Usp. Fiz. Nauk **168**, 1041 (1998) [Phys. Usp. **41**, 945 (1998)].
2. M. B. Bogdanov and A. M. Cherepashchuk, Astron. Zh. **73**, 783 (1996) [Astron. Rep. **40**, 713 (1996)].
3. M. A. Hendry, I. J. Coleman, N. Gray, *et al.*, New Astron. Rev. **42**, 125 (1998).
4. S. B. Gaudi and A. Gould, Astrophys. J. **513**, 619 (1999).
5. C. Alcock, W. H. Allen, R. A. Allsman, *et al.*, Astrophys. J. **491**, 436 (1997).
6. M. B. Bogdanov and A. M. Cherepashchuk, Astron. Zh. **76**, 688 (1999) [Astron. Rep. **43**, 601 (1999)].
7. P. Schneider, J. Ehlers, and E. E. Falco, *Gravitational Lenses* (Springer-Verlag, Berlin, 1992).
8. A. F. Zakharov, *Gravitational Lenses and Microlenses* [in Russian] (Yanus-K, Moscow, 1997).
9. M. B. Bogdanov and A. M. Cherepashchuk, Astron. Zh. **77**, 842 (2000) [Astron. Rep. **44**, 745 (2000)].
10. M. D. Albrow, J.-P. Beaulieu, J. A. R. Caldwell, *et al.*, Astrophys. J. **512**, 672 (1999).
11. M. D. Albrow, J.-P. Beaulieu, J. A. R. Caldwell, *et al.*, Astrophys. J. **522**, 1011 (1999).
12. M. D. Albrow, J. An, J.-P. Beaulieu, *et al.*, Astrophys. J. **549**, 759 (2001).
13. C. Alcock, R. A. Allsman, D. Alves, *et al.*, Astrophys. J. **541**, 270 (2000).
14. B. Grieger, R. Kayser, and T. Schramm, Astron. Astrophys. **252**, 508 (1991).
15. E. Agol and J. Krolik, Astrophys. J. **524**, 49 (1999).
16. M. B. Bogdanov and A. M. Cherepashchuk, Astron. Zh. **79** (2002) (in press) [Astron. Rep. **46** (2002) (in press)].
17. A. V. Goncharskiĭ, A. M. Cherepashchuk, and A. G. Yagola, *Ill-posed Problems of Astrophysics* [in Russian] (Nauka, Moscow, 1985).
18. F. Natterer, *The Mathematics of Computerised Tomography* (Wiley, Chichester, 1986; Mir, Moscow, 1990).
19. S. M. Belotserkovskiĭ and I. K. Lifanov, *Numerical Methods in Singular Integral Equations and Their Application to Aerodynamics, the Theory of Elasticity, and Electrodynamics* [in Russian] (Nauka, Moscow, 1985).
20. M. B. Bogdanov, astro-ph/0102031 (2001).
21. A. N. Tikhonov, A. V. Goncharskiĭ, V. V. Stepanov, and A. G. Yagola, *Regularizing Algorithms and a Priori Information* [in Russian] (Nauka, Moscow, 1983).
22. A. V. Goncharskiĭ, S. Yu. Romanov, and A. M. Cherepashchuk, *Finite-Parametric Inverse Problems of Astrophysics* [in Russian] (Mosk. Univ., Moscow, 1991).
23. R. L. Kurucz, Harvard Preprint No. 3348 (1991).
24. A. Claret, J. Diaz-Cordoves, and A. Gimenez, Astron. Astrophys., Suppl. Ser. **114**, 247 (1995).
25. S. H. Rhie and D. P. Bennett, astro-ph/9912050 (1999).
26. B. S. Gaudi and A. O. Petters, astro-ph/0112531 (2001).

Translated by K. Maslennikov